University of Vermont

ScholarWorks @ UVM

6-1-2014

Understanding and Managing the Impacts of Electric Vehicles on Electric Power Distribution Systems

Paul Hines
University of Vermont, paul.hines@uvm.edu

Jeff Frolik
University of Vermont

Jeffrey Marshall
University of Vermont

Jonathan Dowds
University of Vermont

Pooya Rezaei
University of Vermont

See next page for additional authors

Follow this and additional works at: https://scholarworks.uvm.edu/trc

Authors

Paul Hines, Jeff Frolik, Jeffrey Marshall, Jonathan Dowds, Pooya Rezaei, Andrew Seier, Andrew Fuhrmann, and Alexander Hilshey

Understanding and Managing the Impacts of Electric Vehicles on Electric Power Distribution Systems

DISCLAIMER

The contents of this report reflect the views of the authors, who are responsible for the facts and the accuracy of the information presented herein. This document is disseminated under the sponsorship of the Department of Transportation University Transportation Centers Program, in the interest of information exchange. The U.S. Government assumes no liability for the contents or use thereof.

Understanding and Managing the Impacts of Electric Vehicles on Electric Power Distribution Systems

A University of Vermont Transportation Research Center research report.

UVM TRC Report #14-010

Authors

Principal Investigator:	Paul Hines, Ph.D.
Co-Principal Investigators:	Jeff Frolik, Ph.D., and Jeffrey Marshall, Ph.D.
Research contributors:	Pooya Rezaei, Andrew Seier, Andrew Fuhrmann, Jonathan Dowds, Alexander Hilshey

Acknowledgement

Table of Contents

Chapter 1

Introduction

In the United States, transportation accounts for 31% of all U.S. greenhouse gas emissions and 180% of all domestic crude oil production[1]. Electrification of the transportation sector is one potential path to simultaneously reduce greenhouse gas emissions and dependence on foreign oil. However, transportation electrification is not without challenges. In order for electrified transportation to result in substantial greenhouse gas emissions reductions, the fuel sources for electricity need to come from low-carbon resources, such as wind and solar power plants. And, the aging U.S. electricity infrastructure will need to be modernized in order to incorporate large amounts of electrified transportation without substantially degrading electricity reliability. While there are a number of useful studies on the greenhouse gas impacts of transportation electrification, only recently have researchers begun to understand the impacts of electricity on electric power infrastructure. Thus, the primary goals of this research project were to understand these impacts in detail and to develop new methods for reducing the impact of transportation electrification on the electricity transmission and distribution infrastructure.

In particular, this report focuses on understanding and mitigating the impact of transportation electrification on the medium and low voltage distribution infrastructure, through which electricity is transported from the bulk power grid, through neighborhoods, to individual homes and businesses. Distribution systems in residential neighborhoods with particularly high plug-in electric vehicle adoption rates may see substantial load increases in the relatively near future, making this problem particularly timely. In prior work[2], researchers identified these distribution system impacts to be notably ill understood. This project focused specifically on the impacts of electric vehicles on two key components of power distribution systems: residential service transformers, and underground cables.

Service transformers are one of the most important components of the power grid. Every home and business connects to the power grid through these relatively small transformers. Because of cost considerations they do not include any telemetry systems that can inform utilities of their health, making it difficult for utilities to know when these components are overloaded. Most residential service transformers are rated to serve between 10 and 50 kVA of load, and typically serve 5-15 homes or small businesses. Yet a single plug-in electric vehicle (PEV) with a fast charging system (240 V Level 2 charging) will consume about 7 kVA. Three electric vehicles will nearly use the entire capacity of a 25-kVA transformer. Because of this potential for overloads, this project studied the impact of PEVs on service transformers in detail. Chapter 2 describes results from a detailed study of the impact of PEVs on service transformers, for two climatically distinct locations (Vermont and Arizona) and for several different types of PEV charge management systems designed to mitigate these impacts. The results clearly show that the

---

[1] Annual Energy Outlook, U.S. Department of Energy, Energy Information Agency, 2014.

[2] Jonathan Dowds, Paul Hines, Chris Farmer, Richard Watts, Steve Letendre, Plug‐in Hybrid Electric Vehicle Research Project: Phase II Report. UVM Transportation Research Center. March 25, 2010.

lower temperatures in Northern climates (such as Vermont) provide a substantial margin for additional PEV adoption, relative to hot climates where even low levels of PEV adoption can cause significant damage. In addition, the research team, in partnership with Green Mountain Power, installed two new "Smart" transformers, which included detailed thermal monitoring software. Chapter 3 describes results from this data collection and modeling work.

Secondly, this project studied the impact of PEV adoption on underground cables. Underground cables, as with service transformers, are critical to many medium voltage power distribution systems. Since they are expensive and time-consuming to replace, understanding the impact of new loads on these components is an important part of understanding the overall impact of electric vehicles on the grid. As with transformer impacts, we found that the impact of PEVs on underground cables was particularly ill understood in the research literature. Based on a review of this literature, the research team found that the impact of rainfall on underground cables was a particularly notable gap. To address this gap, the team developed a new method to model the impact of rainfall on water and heat transport in the soil surrounding a cable. This new method makes it possible to accurately predict soil moisture and heat transfer variation based on recorded weather conditions. This should make it possible to adjust the load limits of underground cables, based on actual conditions, which will allow for more efficient use of these important distribution system components. Chapter 4 of this report describes the results of this new modeling method.

Finally, this project studied new methods to dynamically adjust the number of electric vehicles that are charging simultaneously, in order to mitigate the risk of electricity infrastructure damage from electric vehicle charging. While other researchers have also developed methods to dynamically manage electric vehicle charging, most have suggested centralized optimization-based methods, which tend to raise concerns about Smart Grid privacy and security. Instead, this project studied an alternative approach that harnesses algorithms used in communications systems (such as the Internet, home Wi-Fi networks or wireless sensor networks) in order to ensure that vehicles do not overload the grid, while preserving privacy and vehicle autonomy. This new "Packetized" approach to PEV charge management is described in detail in Chapter 5, which also presents results from extensive tests of this approach.

Together these results suggest that PEV adoption can have impacts on the electric power distribution infrastructure, but that these impacts can be managed. Locations with very high levels of PEV adoption may need to upgrade aging infrastructure, however, areas with cooler, high-moisture climates (such as Vermont) may be able to leverage existing infrastructure for some time before extensive upgrades are needed to support large-scale transportation electrification. If large-scale adoption of PEVs does occur in some areas, methods such as the packetized approach may substantially reduce the need for large-scale increases in transmission and distribution infrastructure.

Chapter 2

Estimating the Impact of Electric Vehicle Smart Charging on Distribution Transformer Aging*

Alexander D. Hilshey, Paul D. H. Hines, Pooya Rezaei, Jonathan R. Dowds

Abstract

This paper describes a method for estimating the impact of plug-in electric vehicle (PEV) charging on overhead distribution transformers, based on detailed travel demand data and under several different schemes for mitigating overloads by shifting PEV charging times (smart charging). The paper also presents a new smart charging algorithm that manages PEV charging based on estimated transformer temperatures. We simulated the varied behavior of drivers from the 2009 National Household Transportation Survey, and transformer temperatures based an IEEE standard dynamic thermal model. Results are shown for Monte Carlo simulation of a 25kVA overhead distribution transformer, with ambient temperature data from hot and cold climate locations, for uncontrolled and several smart-charging scenarios. These results illustrate the substantial impact of ambient temperatures on distribution transformer aging, and indicate that temperature-based smart charging can dramatically reduce both the mean and variance in transformer aging without substantially reducing the frequency with which PEVs obtain a full charge. Finally, the results indicate that simple smart charging schemes, such as delaying charging until after midnight can actually increase, rather than decrease, transformer aging.

1 Introduction

With a growing number of mass-market plug-in hybrid and battery electric vehicles (collectively plug-in electric vehicles, PEVs) currently for sale or scheduled to go on sale, there is a growing need to understand the impact that PEV charging loads will have on the electricity distribution infrastructure. Substantial research exists regarding the impacts of PEVs on gasoline consumption [1, 2], power-plant emissions [3, 4], electricity costs [5, 6, 7], transmission adequacy [8], and generating supply adequacy [7, 9, 10]. However, the literature on medium and low voltage distribution system impacts (see Sec. 1.2) is more limited and offers less guidance to utilities looking to incorporate PEV impacts into their maintenance and investment plans.

Several factors combine to make quantifying the impact of PEVs on the medium and low voltage distribution infrastructure a particularly pressing issue. First, the social benefits offered by PEV deployment in terms of reduced oil consumption and life-cycle greenhouse gas emissions

---

have prompted policies at the state and federal levels geared toward increasing the rate of PEV adoption [11, 12, 13]. Second, because early PEV adopters are likely motivated, at least in part, by environmental concerns, and because there is evidence from past hybrid electric vehicle sales that environmentally motivated vehicle consumers tend to be geographically clustered [14, 15], it is likely that PEV sales will be concentrated in particular areas. This clustering means that PEV charging loads will impact local distribution infrastructure well before the impacts on transmission or generation infrastructure is significant. If, as is suggested in [16], these impacts are severe distribution utilities may need to make significant infrastructure investments in high-adoption locations to facilitate this new load. Accurate information on PEV impacts is essential to ensure that these investments are made in an efficient manner. Thus the objective of this paper is to present, and illustrate the utility of, a computational method for estimating the additional transformer aging resulting from PEV charging load and to evaluate different approaches to manage the additional transformer load from PEV charging.

1.1 Background on modeling PEV power demand

Accurately estimating the impact of PEV charging on electric power system components requires both component models and good estimates of the magnitude and timing of demand increases due to PEV charging. Early PEV research assumed very simple charging profiles, such as assuming that vehicles will charge daily starting at 17:00, 18:00 or 19:00 hours, with batteries fully depleted at the start of each charge cycle [17, 2, 7, 18]. However actual PEV charging loads will depend highly on travel patterns, which vary tremendously from driver to driver and day to day. To better capture this variability in driving behavior, researchers have used either detailed GPS data for small groups of drivers, or survey data from larger populations. Ref. [19] used data from 9 drivers to estimate variability in daily miles driven, but with fixed evening arrival times. Another study [20] used GPS data from 76 vehicles to derive a stochastic model of miles driven and arrival/departure times. Reference [21] uses a larger set of GPS data to develop a Monte Carlo model that is similar to the one presented here, but the data are not used to model the miles driven, which is necessary to estimate the battery state-of-charge on arrival. Other researchers have also use Monte Carlo methods to study PEV charging impacts [22, 23, 24] but do not specifically consider distribution transformer aging. The authors in [22] study harmonics due to PEV fast charging; Ref. [23] investigates system level PEV charging impacts including bus voltages, branch currents, and energy losses; and [24] uses a Monte Carlo model to predict reliability, efficiency and profitability of Vehicle-to-Grid (V2G) technology.

While GPS data can allow one to estimate day-to-day variability in driver behavior, the small sample sizes, typical of GPS studies, may result in biased outcomes. An alternative (or perhaps supplement) is to use large-scale driver survey data, such as the US National Household Travel Survey (NHTS) [25] to estimate driver behavior. Ref. [26] used NHTS data to develop a probabilistic model for PEV loads, but focused on modeling large numbers of vehicles, such that the patterns for individual PEVs are averaged. This paper also employs the NHTS data, but with a pure sampling strategy that allows for precise tracking of vehicle departure and arrival times, and the battery state of charge.

1.2 Background on transformer aging models

There is conflicting evidence regarding the impact of PEVs on the residential distribution infrastructure. Ref. [16] uses a time-series model of transformer aging and argues that PEV charging could decrease transformer life by 93%. The study results, however, are based on a transformer model [27] that does not consider the impact of transient ambient temperatures. Another study [28] suggests that a PEV penetration level as small as 10% could induce additional distribution transformer overloading beyond planned overloading. Ref. [29] discusses two residential distribution circuits and estimates that distribution infrastructure costs could increase by 19% and energy losses could increase by 40% with substantial (60%) PEV deployment.

Transformers are among the most costly components in the medium and low voltage distribution infrastructure, and therefore, transformer aging is a key consideration when evaluating the impacts of PEV charging and deciding whether or not to employ smart charging. Transformer aging depends highly on the state of internal insulation material, which is impacted by internal transformer temperatures, specifically the hottest spot temperature. Accurately modeling hottest spot temperature is crucial to accurately predicting transformer aging. Pierce [30] provides a detailed thermodynamic model of transformer temperatures and fluid flow during transient temperature and loading conditions. This method became the industry standard when it was published in the 1995 revision of IEEE C57.91 [31] as Annex G. The Annex G method is not, to our knowledge, contested in the existing literature, and was thus chosen for the transformer model used in this paper.

1.3 Background on Smart Charging

The extent to which PEV charging will impact the distribution infrastructure will depend highly on the charging method used. For instance, the results of [8] and [32] suggest that impacts of PEV charging on components of residential feeders could be minimal given the presence of smart charging, and Ref. [33] argues that PEV deployment with smart charging could yield net benefits for the distribution system by leveling power demand and thus reducing distribution losses per unit energy. Ref. [19] used GPS travel data to obtain expected transformer insulation life in different charging scenarios, and proposed a smart-charging algorithm to reduce the loss of life in transformers. The authors in [34] used time-of-use price to find optimal charging loads, which minimize the charging cost in a regulated market. They argue that using their method reduces cost and flattens the load curve. Ref. [35] used the same GPS data as [20] to predict realistic driving habits and proposes a decision-making process for charging based on a fuzzy-logic system. The authors in [36] proposed an optimal charge management algorithm for a large number of PEVs in a parking lot and compare their optimization algorithm with more traditional methods. Ref. [37] investigated unidirectional V2G to maximize aggregator profit while satisfying system load and price constraints; different smart charging algorithms for a hypothetical group of commuter cars are simulated to obtain a continuous variable charge rate. They showed the benefits of combining regulation and reserves bids [38] and concluded that that price constrained optimal bidding outperforms other methods. Centralized charging of PEVs is studied in [39] to minimize distribution network losses using three different objective functions and using simplified travel behavior. In addition, there is substantial international research into electric vehicle smart charging (e.g., [40, 41, 42]), as well as international efforts to develop standards for PEV communications (e.g., ISO 15118 [43]).

This paper extends previous work [44] to describe both a method for estimating the impact

of PEV charging on overhead distribution transformers (given a time-series transformer insulation material thermal model and PEV charging demand derived from observed light-duty vehicle travel patterns) and a method for mitigating this impact through a transformer temperature-based smart charging algorithm designed to reduce damaging transformer overloading. Furthermore, temperature-based control is compared to several other approaches to smart charging. Sec. II describes a method for modeling residential load with PEV charging. Sec. III describes the transformer thermal model, summarizing and providing a supplemental guide to the Annex G transformer thermal model. Sec. IV describes the various smart charging algorithms employed, which is followed by results (Sec. V). Finally we summarize our conclusions in Sec. VI.

2 Modeling PEV charging loads

In this paper, residential load profiles are comprised of two components: residential baseline load (L_h) and load from PEV charging (L_v). As we are primarily focused on the effect of PEV loads, we assumed that each home connected to a distribution transformer has identical, deterministic baseline load. However, in order to study travel pattern variation, we sampled from empirical travel data to develop a Monte-Carlo model of the PEV portion of the residential load profile.

2.1 Residential baseline load without PEV charging

The National Energy Modeling System (NEMS) reported itemized residential load profiles in [45], which are interpreted in [28] to produce a single home daily load profile. We fed these data into a cubic spline to produce a one home, 24-hour load profile, $L_h(t)$, with one minute time steps. Our model multiplied this daily pattern by the quantity of homes (n_h) serviced by an overhead distribution transformer to obtain the total transformer load, before adding vehicles. The power factor for the residential loads was assumed to be 0.9 lagging. The result is a baseline demand profile, which we assume to be constant from day to day over a one-year period. Fig. 1 displays the daily baseline demand profile for a 25kVA transformer servicing 12 homes and 6 PEVs, along with the travel patterns for the 6 PEVs. Baseline load values in Fig. 1 that are in excess of the 25kVA transformer rating represent periods of planned overloading, which are acceptable according to [31].

2.2 Additional load from PEV charging

This section describes the method used to develop a Monte Carlo model of PEV load (L_v), based on National Household Transportation Survey data [25]. The NHTS is a comprehensive survey of U.S. travel patterns conducted by the Federal Highway Administration. The survey data aim to include all trips taken by all members of the household within a 24 hour period including the length, timing, duration and mode of transportation for each trip. As the NHTS travel data do not reflect behavior of PEV-specific drivers, we assume that travel behavior of PEV and non-PEV drivers is indistinguishable.

The goal of the PEV charging model was to estimate the additional time-varying load that would result from n_v vehicles charging at a certain point in a power grid. For each one-year run of our model we randomly selected n_v vehicles from among the vehicles in the New England subset of the NHTS data that both start and end the day at home. In our model half of the vehicles were assumed to have the charging and efficiency characteristics of the Chevrolet Volt (10.4 kWh
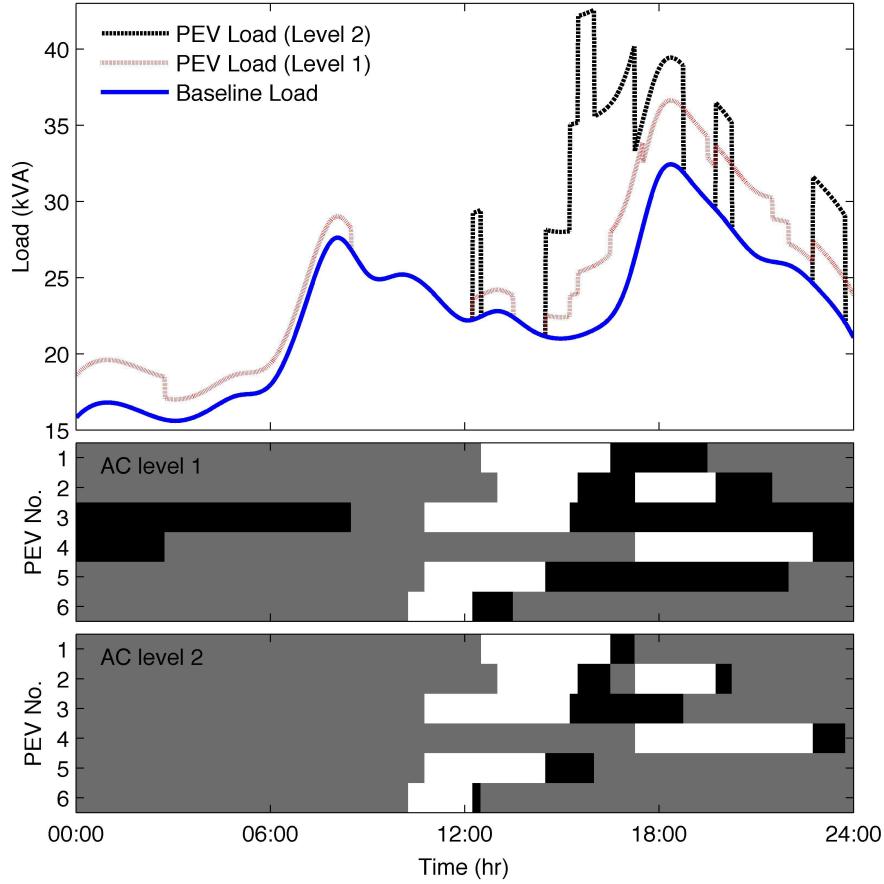
Figure 1: The top panel shows the daily baseline load profile with and without PEVs for a 25kVA overhead distribution transformer servicing 12 homes and 6 randomly selected PEVs charging at AC Level 1 and AC Level 2. Both charging levels correspond to the same sample set of PEV charging behavior. The middle and lower panels show the state of each vehicle throughout the day, which is one of: away (white), parked but not charging (gray), or charging (black).

battery and 0.26 kWh/mile), and the other half had the characteristics of the Nissan Leaf (24 kWh and 0.24 kWh/mi)[1]. Additionally, we assumed that all PEVs charge exclusively from a home charging station. Without smart charging in place, we assumed charging begins immediately upon the vehicle's arrival at home and continues until either the battery reaches full capacity or the vehicle begins a new trip. We assumed either AC Level 1 (1.4 kW) or AC Level 2 (7 kW) charging as established in [46] and 85% charge efficiency as reported in [47]. Based on data obtained from a GM Volt (Fig. 2), we assumed that the power draw was constant until the battery fully charged and that the power factor was 1.0.

The sampling method used in this paper represents the state of each vehicle v using two variables: the state-of-charge for each battery (represented by D_v, the amount of energy needed to fill the battery) and a binary variable, A_v, indicating whether the vehicle is parked at home and connected to a wall socket. Thus, the time required to fully charge the battery of vehicle v at charge rate P_v is $T_v = D_v/P_v$. If the step size for vehicle modeling is Δt (in units of hours), the load (in

---

[1]Battery size and efficiency calculated from data provided in the vehicle owner's manuals from GM and Nissan.
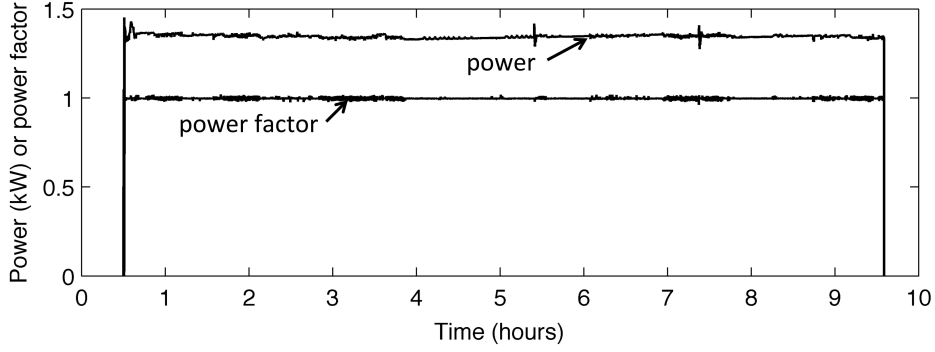
Figure 2: AC power consumption and power factor for a full (AC Level 1) charge of a GM Volt. Data courtesy of Green Mountain Power.

kW) due to vehicle v during time interval $[t, t + \Delta t)$ is:

$$L_v(t, \Delta t) = \begin{cases} A_v(t)P_v, & \text{if } T_v(t) \geq \Delta t \\ A_v(t)\frac{D_v(t)}{\Delta t} & \text{if } 0 < T_v(t) < \Delta t \\ 0, & \text{if } T_v(t) \leq 0 \end{cases} \tag{1}$$

For the purposes of this model, we randomly select a weekday and a weekend driving profile from the New England subset of the NHTS data for each v. These are reproduced to give a one-year charging pattern for each vehicle. We chose a vehicle model step size (Δt) of 0.25 hours.

The total load (in kVA) on the transformer is the combination of the n_h (complex) residential loads and loading from n_v randomly selected PEVs:

$$L(t) = \left| n_h L_h(t) + \sum_{v=1}^{n_v} L_v(t) \right| \tag{2}$$

Fig. 1 illustrates the results from the model by showing the additional load due to 6 PEVs added to the load for 12 homes, at Level 1 and Level 2 charging rates.

It is important to note that the baseload data $L_h(t)$ (as well as the temperature data for the thermal model below), were initially available at hourly intervals. These were translated into one-minute data (the step size for the thermal model) using a cubic spline. The PEV load is also translated into one-minute data, from the 15 minute step size in the model, assuming that the PEV load does not change within each 15 minute interval.

3 Modeling Distribution Transformer Aging

Our model for estimating distribution transformer aging simulates the thermal performance of an overhead distribution transformer, installed in a location with a known trajectory of ambient temperatures $T_A(t)$ and load $L(t)$, based on IEEE C57.91-1995. One-minute ambient temperature data, $T_A(t)$, were obtained by feeding hourly temperature data from the National Climatic Data Center[2] into a cubic spline to produce one-minute data. The combined PEV/baseline data came from (2). We obtained transformer specifications from data provided by a local distribution utility.

The output of the model is an estimate of the total one-year accelerated aging of the transformer

---

[2]http://www.ncdc.noaa.gov

insulation material, in years. When this "Factor of Equivalent Aging" (F_{EQA}) is greater than 1.0, the transformer is aging at a rate that is greater than its designed level of 1 year per year.

3.1 Transformer thermal model

The transformer thermal model estimates internal transformer temperatures using the Annex G method of IEEE C57.91-1995 [31]. Annex G describes the heat transfer and fluid flow dynamics of the transformer while accounting for transient loading and ambient temperature conditions, changes in oil viscosity and winding resistance, and cooling mode. While the reader should refer to Annex G for precise details, the core of the method consists of three differential equations for internal transformer temperatures, which have the general form:

$$\frac{dT_W}{dt} = f_1\left(L^2(t), T_W(t) - T_{DAO}(t)\right) \tag{3}$$

$$\frac{dT_O}{dt} = f_2\left(L^2(t), T_A(t) - T_O(t), ...\right.$$
$$\left. T_W(t) - T_{DAO}(t)\right) \tag{4}$$

$$\frac{dT_{HS}}{dt} = f_3\left(L^2(t), T_W(t) - T_{HS}(t)\right) \tag{5}$$

The first equation (3) describes the average transformer winding temperature, $T_W(t)$, as a function of the square of load, $L^2(t)$, and the average temperature of fluid in the winding cooling ducts, $T_{DAO}(t)$. The second (4) models the average cooling oil temperature, $T_O(t)$, based on the difference between $T_W(t)$ and $T_{DAO}(t)$, and between $T_A(t)$ and $T_O(t)$. Equation (5) describes the transformer hottest spot temperature based on the difference of $T_W(t)$ and $T_{HS}(t)$. Calculated values for (5) are used in the transformer damage function, as described in Sec. 3.3. Following the procedure in Annex G, we solved (3)-(5) using first order Euler's method, with a 1-minute time step.

3.2 Transformer insulation loss-of-life equations

Transformer insulation typically fails prior to other components within a transformer. For this reason, the estimated life of a transformer is primarily a function of aging within the transformer insulation. Accelerated aging is a measure of how quickly the transformer insulation degrades under actual conditions, relative to degradation at rated loading and rated ambient temperature conditions. Clause 5 of IEEE Std. C57.91-1995 [31] provides a method for estimating distribution transformer aging, which we summarize here.

Excessively high hottest spot temperatures damage a transformer's insulation through the destructive process of pyrolysis [48]. To model this, the calculated $T_{HS}(t)$ are fed into a damage function [31] that estimates the instantaneous accelerated aging of the transformer ($F_{AA}(t)$), which can be integrated to compute the total transformer thermal aging over a time horizon (T) to yield the average Factor of Equivalent Aging (F_{EQA}):

$$F_{EQA}(t) = \frac{1}{T}\int_{t-T}^{t} e^{\left(\frac{15,000}{T_{HS,R}+273} - \frac{15,000}{T_{HS}(t)+273}\right)} dt, \tag{6}$$

Equation (6) was used to estimate the total distribution transformer aging over a $T = 1$ year period.
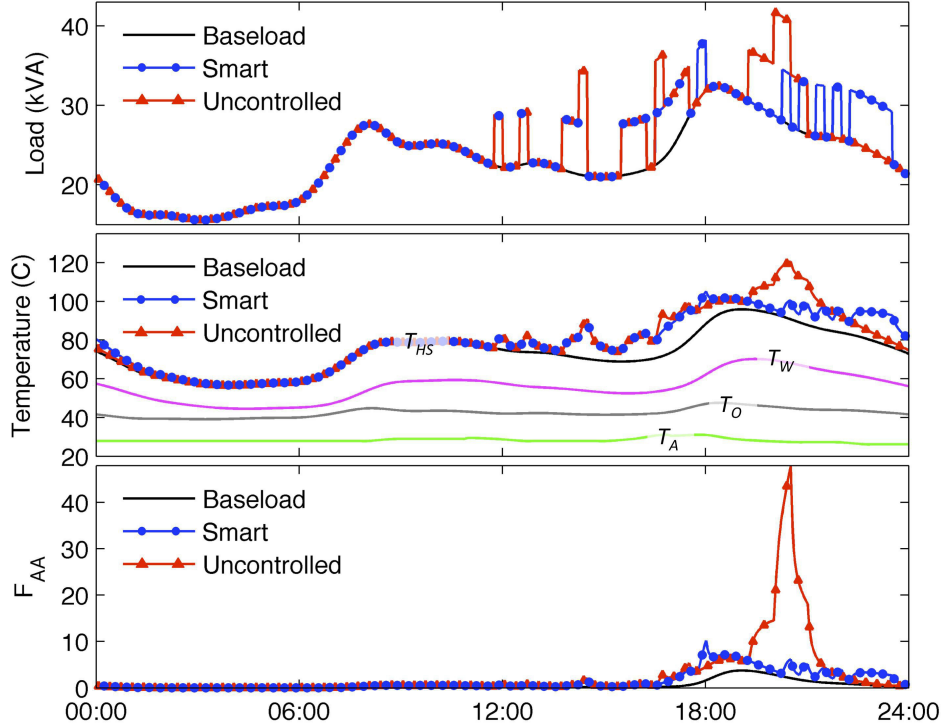
9

Figure 3: Illustration of model estimating distribution transformer aging over the course of one day. The transformer modeled is a 25kVA overhead distribution transformer servicing 12 homes. The temperature data come from Phoenix, Arizona, 2010. The transformer is modeled under zero PEVs, 6 PEVs with uncoordinated AC Level 2 charging and 6 PEVs with temperature-based AC Level 2 smart charging ("Smart" in the graph above). The top panel shows load as seen by the transformer. The middle panel shows ambient temperature and internal transformer temperatures; T_O and T_W are only shown for the base load case. The bottom panel shows the instantaneous factor of accelerated aging, $F_{AA}(t)$.

3.3 Distribution transformer aging model sample result

Fig. 3 illustrates the combined effect of the transformer thermal model and transformer insulation aging equations, with and without PEV-charging load ($n_v = 6$) and under smart and uncontrolled charging. For this sample result, the transformer thermal model produced transformer internal temperatures and F_{AA} values for a 25kVA distribution transformer serving 12 homes. Table 1 describes the transformer parameters used in this study. The ambient temperature in Fig. 3 represents a 2010 "hot" day in Phoenix, AZ. As shown in the lower panel of Fig. 3, the uncontrolled PEV charging case exhibits a brief period of extreme aging, approaching 50 years per year.

4 Smart Charging Methods

If a distribution transformer is overloaded due to PEV charging, it can either be replaced with a larger unit, or the PEV load can be managed with financial incentives and smart charging technology. This section describes several different approaches to smart charging, which might be employed to to extend the life of a transformer serving several electric vehicles.

A successful smart charging algorithm should ensure that all PEVs receive as close to a full charge as possible, thus minimally inconveniencing the PEV owner, while mitigating the negative

Table 1: Transformer Parameters Used*

Parameter	Symbol	25kVA
Rated httest spot temp.	$T_{HS,R}$	84.4 °C
Rated winding temp.	$T_{W,R}$	77.0 °C
Rated ambient temp.	$T_{A,R}$	30 °C
Volume of oil	-	41.6 L
Mass of core	M_C	79.9 kg

*Parameter values were obtained from transformer manufacturer specification sheet provided by a local utility. Parameter values not provided by the manufacturer (not shown) were chosen in accordance with Annex G recommendations.

impacts of high loads on the electricity infrastructure. The smart charging algorithm proposed in Sec. 4.1 seeks to do this directly by determining how many PEVs may charge at a given time without pushing the distribution transformer into sustained, rapid accelerated aging. Other approaches are discussed in Sec. 4.2. In all cases, we assume that smart meters (Advanced Metering Infrastructure) are installed at each home, which allow a charge management device at the transformer to monitor instantaneous loads and send signals to vehicles connected to the transformer to forgo charging for a specified time period. Finally, we also assume that sufficient financial incentives and technology are in place to ensure participation. While this last assumption is unrealistic (some vehicle owners are unlikely to participate in smart charging programs), doing so allows us to understand the impact of different approaches.

4.1 Smart charging based on transformer temperature

Our smart charging algorithm requires two inputs: the transformer aging status, comprised of $F_{AA}(t)$ and $F_{EQA}(t)$, which are derived from the aging calculations in Sec. III, and the quantity of PEVs requesting charge, $q_r(t)$. The algorithm yields one output: the quantity of PEVs that may charge at time t: $q(t) \leq q_r(t)$. When implemented in a charge management device associated with a transformer, the algorithm operates in two steps. Step one determines $q(t)$. The second step dispatches a signal to smart meters, which subsequently signal each vehicle to either continue or discontinue charging. Step two is performed by random allocation, which has the advantages of 1.) not requiring the exchange of information pertaining to battery level and 2.) avoiding the need to decide which PEV "deserves" charging precedence.

To determine the modeled transformer aging status, we assume that smart meters report instantaneous household load to the transformer, as well as the number of vehicles available for charge management, $q_r(t)$. The aggregated $L(t)$ and a measured value for $T_A(t)$ are fed into the transformer thermal model (Sec. 3), which yields $F_{AA}(t)$ and $F_{EQA}(t)$ averaged over a period of time. An F_{EQA} averaging period of 12 hours was chosen to ensure that brief periods of high-temperature operation did not extend to produce high average aging over longer periods. Numerical tests of the algorithm with averaging periods of 6, 12, 18, and 24 hours did not show that the averaging period had a statistically significant effect on annual transformer aging.[3]

After calculating $F_{AA}(t)$ and $F_{EQA}(t)$, the algorithm compares the modeled transformer aging status against four aging thresholds ($H_{EQA}, H_{\min}, H_{\text{med}}$, and $H_{\max}$) to determine whether $q(t)$ should be increased, decreased, or held constant in the next time period. Equation (8) is used to

---

[3]In our test, mean aging ranged from 1.572 to 1.588, with a standard deviation of 0.2. The differences were not significant.

choose the change in $q(t)$ from the previous time period:

$$q(t) \;=\; q(t - \Delta t) + \Delta q(t) \tag{7}$$

$$\Delta q(t) \;=\; \begin{cases} +1, & \text{if } (F_{AA} < H_{\min}) \text{ or} \\ & (F_{AA} < H_{\text{med}} \,\&\, F_{EQA} < H_{EQA}) \\ -1, & \text{if } F_{AA} > H_{\text{med}} \\ -2, & \text{if } F_{AA} > H_{\max} \\ 0 & \text{otherwise.} \end{cases} \tag{8}$$

Table 2 provides suggested aging threshold values, as determined from numerical experimentation.

Table 2: Aging Thresholds used for Temperature-based Smart Charging Algorithm

H_{EQA}	$H_{\min}$	H_{med}	$H_{\max}$
2.5	3.5	4	4.75

Unless $q(t)$ is greater than $q_r(t)$, in which case all requesting PEVs may charge, the smart charging algorithm randomly chooses $q(t)$ vehicles from the set of vehicles that are currently requesting charge, $q_r(t)$, and signals the smart meters to allow or forgo charging to their respective PEVs.

Fig. 3 highlights the differences between uncontrolled and smart charging using a transformer operating during a high-temperature, 24 hour period for Phoenix, Arizona and serving six PEVs. The smart charging algorithm delayed charging for several vehicles, away from the hottest hours or heaviest load periods of the day.

Note that the communication costs for this control algorithm are minimal. The only data exchange that is needed is for the vehicle to query a "transformer control agent" once every 15 minutes to request permission to charge. The transformer would need to assemble the requests and randomly grant a subset of these requests, according to (8). The transformer control agent does not need to gather information about the battery state of charge, the departure time of the vehicle, or whether the PEVs will charge at other locations, which is advantageous in terms of customer privacy and simplicity. The algorithm, as implemented, is fully capable of handling the adding and removing of vehicles, assuming that the vehicles can communicate with the control agent. We assume that this communication would be encouraged through a preferential smart charging rate structure.

The algorithm could also be applied without major changes to mitigate overloads on a distribution feeder transformer, so long as there was sufficient communication bandwidth to facilitate requests between the vehicles and the transformer. Also, the algorithm assumes that PEVs can only be controlled in a binary manner, making it feasible to implement within bandwidth-limited, high latency first generation Advanced Metering Infrastructure (AMI). As AMI improves, real-time communications between grid infrastructure and smart meters will be increasingly feasible, making it feasible to adapt the temperature-based control algorithm for bi- or unidirectional and continuous charging control (V2G).

4.2 Other smart charging methods

To compare temperature-based smart charging to other approaches, we measured transformer aging and the frequency of charge mitigation for three existing smart charging methods:

1. *After Midnight* (AM): all charging is postponed until after 12:00 am, and before 6:00 am to avoid the peak load period;

2. *Load Cutting* (LC): charging starts immediately upon the arrival of the PEV at the home charging station but is limited based on the aggregate transformer load such that PEV charging (w/ 15 minute intervals) is randomly allocated every 15 minutes, to ensure that the transformer load remains below its load limit; in a variant of this method, the load limit is increased to 30kVA during nighttime hours (10:00 pm - 8:00 am);

3. *"Randomized Charging Strategy"*: following the method proposed in [19], a random array of charging time slots, with 15 minute intervals, is allocated between 7:00 pm or the vehicle arrival time (whichever is later), to ensure that the vehicle is charged by 6:00 am.

5   Results

As concluded in previous work [44], ambient temperatures can dramatically affect the impact of PEV charging on transformers. Therefore, we examined PEV charging impacts with one year of ambient temperature data from two climatically distinct U.S. cities: Burlington, Vermont (VT) and Phoenix, Arizona (AZ), which have average July temperatures of 21.4°C and 34.8°C respectively. The main goal was to compute the annual factor of equivalent aging (F_{EQA}), which we also refer to as the transformer's aging rate. To compensate for variability in PEV driver travel behavior, we ran the transformer model for 10,000 sets of randomly generated travel patterns, under each of the following five test conditions, for both locations: 1) no PEV charging; 2) AC Level 1, uncoordinated PEV charging; 3) AC Level 1, temperature-based smart PEV charging; 4) AC Level 2, uncoordinated PEV charging; and 5) AC Level 2, temperature-based smart PEV charging. In addition, the three smart charging algorithms from Sec. 4.2 were compared, for both charging levels and in both locations. As in Fig. 3, the 25 kVA transformer was assumed to serve 12 homes and 6 vehicles, each with unique weekday and weekend travel patterns for each model run. The average baseline load was 22.8 kVA, which is near the rated limit.

Figure 4 shows the simulation results for no PEVs, uncontrolled, and temperature-based charging for each location. The uncontrolled charging results show a substantial difference between AC Level 1 and 2 charging. Level 2 charging increases aging rates by a factor of 5.6 and 4.2 above the uncontrolled level, in Vermont and Arizona respectively. Clearly, higher charging rates will result in increased aging rates for distribution infrastructure. Additionally, the results show that temperature-based smart charging can dramatically reduce transformer aging. The proposed smart charging algorithm reduced average transformer aging in Burlington by a factor of 1.4 for AC Level 1 and a factor of 4.8 for AC Level 2, relative to uncontrolled charging. In Phoenix, the differences are greater, with average F_{EQA} falling by factors of 1.8 and 6.3 for Levels 1 and 2, respectively. For all cases, a two-sample Kolmogorov-Smirnov test shows statistical significance of the reduction in aging from temperature-based smart charging ($p < 10^{-3}$ for all cases).

The results also indicate that temperature-based smart charging can dramatically reduce the uncertainty in transformer aging that results from differing travel patterns among vehicles. The 90th percentile aging rates for the Level 2 cases (from Fig. 4) decrease by an order of magnitude under temperature-based smart charging in both Arizona and Vermont. This indicates that temperature-based smart charging can reduce both the average, and the variance in transformer life expectancy under high levels of PEV adoption.
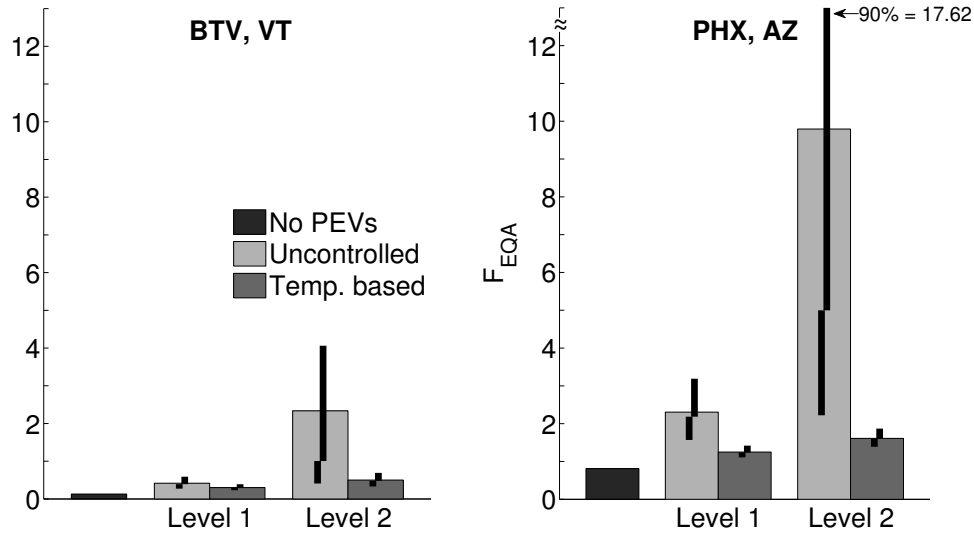
13

Figure 4: The annual factor of equivalent aging (F_{EQA}) for Burlington, VT & Phoenix, AZ for no PEVs, uncontrolled PEV charging, and temperature-based smart charging. The graph displays average (bars) and $10^{th} - 50^{th}$ & $50^{th} - 90^{th}$ percentile (black lines) F_{EQA} values for each location and charging rate.

It is important to emphasize that an algorithm that reduces aging but does not allow adequate charging to the PEV batteries is not desirable. To ensure that the proposed smart charging method resulted in adequate PEV charging, we measured the number of cases in which vehicles fully charged before beginning their next trip, after having been parked at home for an extended period of time. Specifically, we define a "successful charge" to be a period in which the battery was charged to at least 95% of its capacity after being at home long enough to have received a full charge at the unmitigated Level 1 or 2 charging rate. We found that for both charging rates and both locations, vehicles received successful charges in greater than 98% of extended home stays. The only exception to this was AC Level 2 in Arizona which showed an average of 97% successful charge rate. Given that the algorithm achieves a very high rate of charging success for the case of a very heavily loaded transformer, we conclude that the proposed scheme would have almost no noticeable effect on most PEV owners.

For comparison purposes, the three smart charging methods described in Sec. 4.2 were evaluated under the same model parameters as those for the temperature-based smart charging method (both locations and both charging rates). As before, we compared the average annual aging rate (F_{EQA}) for 10,000 iterations and the average percent of successful charges. The results of these simulations are found in Figs. 5 and 6.

All simulated cases showed that load cutting method substantially reduced distribution transformer aging. For AC Level 1, the aging rate decreased from 0.42 (for uncontrolled charging) to 0.18 in VT, and from 2.30 to 1.07 in AZ. For AC Level 2, the average aging rate decreased from 2.34 (for uncontrolled charging) to 0.15 in VT and from 9.79 to 0.90 in AZ. However, the successful charge rate for load cutting was only 66.6% for AC Level 2 and 95.2% for Level 1, which is notably lower that what was obtained from the temperature-based algorithm. This indicates that controlling transformer load based on temperature or aging, rather than merely based on load, will
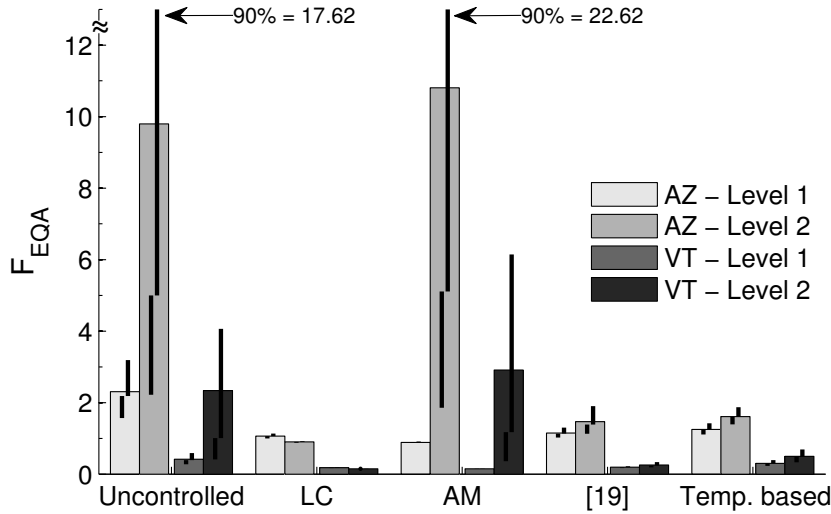
Figure 5: Transformer aging (F_{EQA}) results for uncontrolled charging, and four smart-charging methods: load cutting (LC), after midnight (AM), randomized charging [19], and our temperature-based method. The graph displays average (bars) and $10^{th} - 50^{th}$ & $50^{th} - 90^{th}$ percentile (black lines) F_{EQA} values for each location and charging rate.

reduce the need to curtail PEV charging loads, likely leading to less customer aggravation. In order to further explore the load-cutting method, we attempted to improve the results by increasing the load limit by 20% (to 30 kVA) during night-time hours (10:00 pm to 8:00 am). This modification caused the percent of successful charges to increase by as much as 10% in Level 2 charging (from 67% to 77%), but did not have a significant impact on successful charges in Level 1 charging, or on the average aging rate. The reason is that in the simple load cutting method many Level 2 charging instances are cut when the transformer reaches its full load, but in Level 1 charging the lower charging power allows more PEVs to obtain nearly a full charge before departing. However, in the modified load-cutting method a greater quantity of Level 2 charging occurs during the night, without substantially increasing the aging rate. The results make the modified version more desirable than the simple load cutting method, but still less attractive than the temperature-based method.

At AC Level 1, the after-midnight method resulted in a decrease in aging from 0.42 to 0.15 (compared to uncontrolled charging) for Vermont, and from 2.30 to 0.90 Arizona. At AC Level 2, however, the after-midnight method resulted in an increase in average aging rate from 2.34 to 2.91 and from 9.79 to 10.81 for VT and AZ, respectively. Additionally, the percent of successful charges were quite low: 62.5% for Level 1 and 76.5% for Level 2. These results show that time-delayed charging may only be helpful in reducing distribution transformer aging when AC Level 1 is used, and can have a substantial negative impact on transformer life with higher charging rates. In both cases, the after-midnight method results in a low rate of successful charges, because charging is delayed until after 12:00 am.

The randomized charging strategy from [19] also produced good results in terms of mitigating distribution transformer aging. For AC Level 1, the aging rate decreased from 0.42 to 0.19 in VT and from 2.30 to 1.15 in AZ. For AC Level 2, the average aging rate decreased from 2.34 to 0.26 in VT and from 9.79 to 1.47 in AZ. However, the percent of successful charges was found to be
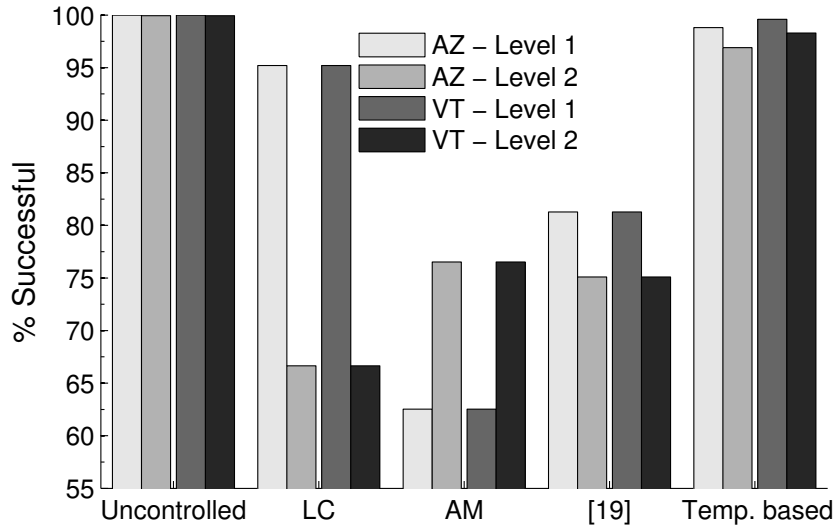
Figure 6: Average percent successful charging for uncontrolled charging and each of the smart charging methods in Fig. 5.

81.3% and 75.1% for AC Levels 1 and 2 respectively. Therefore, the randomized charging strategy, which clearly is effective in reducing distribution transformer aging, may be less desirable given the need to maintain a favorable battery state of charge.

6 Conclusions

This paper describes a method for estimating and mitigating the impact of electric vehicle charging on overhead distribution transformers by combining a transformer thermal aging model with empirical travel behavior and a temperature-based smart charging algorithm. We use Monte Carlo simulation to estimate thermal aging in a fully loaded 25 kVA overhead distribution transformer serving 12 homes and 6 PEVs, with ambient temperature data from Phoenix, Arizona and Burlington, Vermont. We compared the thermal aging in the transformer, as well as the likelihood that vehicles would be able to successfully charge their batteries, for several smart charging algorithms, including a new temperature based control algorithm proposed in this paper.

The results suggest a number of interesting conclusions. First, we found that in all cases the warmer climate of Phoenix, AZ resulted in notably more transformer aging, relative to the cooler climate of Burlington, VT. This indicates that, in cooler climates, a moderate amount of overloading from PEV charging may not substantially decrease transformer life. The results also highlight the need to use location-specific ambient temperature data when evaluating the impact of PEV charging on thermally sensitive infrastructure. Additionally, because of the variability in driver behavior and the exponential aging function, PEV charging is likely to introduce enormous uncertainty in transformer aging, particularly for hot climates. Second, the results show that smart charging in general, and the proposed temperature-based algorithm in particular, can substantially reduce transformer aging. These reductions were substantially greater in the hot climate location, relative to the cool climate one. In addition to this average effect, we found that smart charging can also reduce uncertainty in transformer life, in the face of highly uncertain vehicle travel behavior.

These benefits came with very little cost in terms of inconvenience to PEV drivers. In the proposed temperature-based method, vehicles were able to charge their batteries to at least 95%, after having been at home for long enough to get a full charge, in more than 97% of all cases. While the model indicated that other smart charging algorithms can also reduce transformer aging, methods that were not explicitly focused on mitigating transformer damage tended to result in a greater number of unsuccessful charges. For the case of vehicles charging at AC Level 2 rates, but only being allowed to charge after midnight, smart charging actually increased, rather than decreased transformer aging over the uncontrolled case. Time-of-use pricing schemes, in which vehicles could charge at a reduced cost after a certain hour, could have a similar negative impact on the distribution infrastructure. This emphasizes the need to exercise caution when designing new incentives and technology for time-delayed charging. Unintended consequences, such as creating a sudden spike in load when lower-priced electricity becomes available, could have costly impacts on power delivery infrastructure.

While the focus of this paper is on mitigating transformer damage due to electric vehicle charging, similar methods can be used (and similar results are likely to be obtained), if the proposed temperature-based smart charging algorithm were applied to other large loads that can be time-shifted, such as air-conditioners and water heaters. Also, the relatively smart-charging algorithm proposed in this paper considers only one constraint: the thermal limit of a transformer. Future work will focus on integrated control methods that can manage smart charging to satisfy the many limits in a power system, such as bulk generation availability (and bulk prices) as well the thermal limits of power transformers and underground cables. In addition, as the communications capabilities of AMI systems improve, it will become increasingly feasible to deploy more sophisticated load management algorithms. In future work, we will also investigate the potential benefits and costs of continuous, rather than binary electric vehicle charge management methods.

Acknowledgment

References

[1] J. Gonder, T. Markel, M. Thornton, and A. Simpson, "Using global positioning system travel data to assess real-world energy use of plug-in hybrid electric vehicles," *Transportation Research Record*, 2007.

[2] K. Parks, P. Denholm, and T. Markel, "Costs and emissions associated with plug-in hybrid electric vehicle charging in the Xcel Energy Colorado service territory," National Renewable Energy Laboratory, Golden, CO, Tech. Rep., 2007.

[3] C. Samaras and K. Meisterling, "Life cycle assessment of greenhouse gas emissions from plug-in hybrid vehicles: Implications for policy," *Environmental Science and Technology*, vol. 42, no. 9, pp. 3170–3176, 2008.

[4] R. Sioshansi and P. Denholm, "Emissions impacts and benefits of plug-in hybrid electric vehicles and vehicle-to-grid services," *Environmental Science & Technology*, vol. 43, no. 4, pp. 1199–1204, 2009.

[5] W. Kempton and J. Tomic, "Vehicle-to-grid power fundamentals: Calculating capacity and net revenue," *Journal of Power Sources*, vol. 144, no. 1, pp. 268–279, 2005.

[6] M. J. Scott and M. Kintner-Meyer, "Impact assessments of plug-in hybrid vehicles on electric utilities and regional U.S. power grids part II: Economic assessment," Pacific Northwest National Laboratory, Tech. Rep., 2007.

[7] S. Hadley and A. Tsvetkova, "Potential impacts of plug-in hybrid electric vehicles on regional power generation," Oak Ridge National Laboratory, Tech. Rep., 2008.

[8] C. Gerkensmeyer, M. Kintner-Meyer, and J. DeSteese, "Technical challenges of plug-in hybrid electric vehicles and impacts to the US power system: Distribution system analysis," Prepared for U.S. Dept. of Energy, Pacific Northwest National Laboratory, Tech. Rep., 2010.

[9] P. Denholm and W. Short, "An evaluation of utility system impacts and benefits of optimally dispatched plug-in hybrid electric vehicles," National Renewable Energy Laboratory, Tech. Rep. NREL/TP-620-40293, 2006.

[10] M. Kintner-Meyer, K. Schneider, and R. Pratt, "Impact assessments of plug-in hybrid vehicles on electric utilities and regional U.S. power grids part I: Technical analysis," Pacific Northwest National Laboratory, Tech. Rep., 2007.

[11] D. Crane and B. Prusnek, "The role of a low carbon fuel standard in reducing greenhouse gas emission and protecting our economy, state of California." State of California, Tech. Rep., 2007.

[12] A. E. Farrell and D. Sperling, "A low-carbon fuel standard for California part 2: Policy analysis, institute of transportation studies," University of California, Davis., Tech. Rep., 2007.

[13] EIA, "International energy outlook," US DOE Energy Information Agency, Tech. Rep., 2008.

[14] M. E. Kahn and R. K. Vaughn, "Green market geography: The spatial clustering of hybrid vehicles and LEED registered buildings," *The B. E. Journal of Economic Analysis & Policy*, vol. 9, no. 2, 2009.

[15] J. Sears, J. Dowds, L. Aultman-Hall, and P. Hines, "Travel demand and charging capacity for electric vehicles in rural states: A Vermont case study," *Transportation Research Record*, 2012.

[16] C. Roe, F. Evangelos, J. Meisel, A. Meliopoulos, and T. Overbye, "Power system level impacts of PHEVs," in *Proceedings of the 42nd Hawaii International Conference on System Sciences*, Waikoloa, HI, 2009.

[17] EPRI, "Environmental assessment of plug-in hybrid electric vehicles: Volume 1: Nationwide greenhouse gas emissions," Electric Power Research Institute, Tech. Rep., 2007.

[18] D. Lemoine and D. Kammen, "Effects of plug-in hybrids electric vehicles in California energy markets," in *Proceedings of the TRB 86th Annual Meeting*, 2007.

[19] Q. Gong, S. Midlam-Mohler, V. Marano, and G. Rizzoni, "Study of pev charging on residential distribution transformer life," *IEEE Trans. Smart Grid*, vol. 3, no. 1, pp. 404 –412, March 2012.

[20] A. Ashtari, E. Bibeau, S. Shahidinejad, and T. Molinski, "Pev charging profile prediction and analysis based on vehicle usage data," *IEEE Trans. Smart Grid*, vol. 3, no. 1, pp. 341 –350, March 2012.

[21] M. Kuss, T. Markel, and W. Kramer, "Application of distribution transformer thermal life models to electrified vehicle charging loads using monte-carlo method," *25th World Battery, Hybrid and Fuel Cell Electric Vehicle Symposium and Exhibitionl*, 2010.

[22] F. Koyanagi, T. Inuzuka, Y. Uriu, and R. Yokoyama, "Monte carlo simulation on the demand impact by quick chargers for electric vehicles," in *Power Engineering Society Summer Meeting, 1999. IEEE*, vol. 2, 1999, pp. 1031 –1036 vol.2.

[23] F. Soares, J. Lopes, and P. Almeida, "A monte carlo method to evaluate electric vehicles impacts in distribution networks," in *Innovative Technologies for an Efficient and Reliable Electricity Supply (CITRES), 2010 IEEE Conference on*, Sept. 2010, pp. 365 –372.

[24] C. Sandels, U. Franke, N. Ingvar, L. Nordströ andm, and R. Hamren, "Vehicle to grid: Monte carlo simulations for optimal aggregator strategies," in *Power System Technology (POWER-CON), 2010 International Conference on*, Oct. 2010, pp. 1 –8.

[25] Oak Ridge National Laboratories. (2009) 2009 NHTS user notes. [Online]. Available: http://nhts.ornl.gov/2009/pub/usernotes.pdf

[26] D. Wu, D. Aliprantis, and K. Gkritza, "Electric energy and power consumption by light-duty plug-in electric vehicles," *IEEE Trans. Power Systems*, vol. 26, no. 2, pp. 738 –746, May 2011.

[27] J. F. Lindsay, "Temperature rise of an oil-filed transformer with varying load," *IEEE Trans. Power Apparatus and Systems*, vol. PAS-109, no. 9, pp. 2530–2536, 1984.

[28] S. Shao, M. Pipattanasomporn, and S. Rahman, "Challenges of PHEV penetration to the residential distribution network," in *Proceedings of the IEEE Power & Energy Society General Meeting*, Minneapolis, July 2009.

[29] L. P. Fernández, T. G. S. Román, R. Cossent, C. M. Domingo, and P. Frías, "Assessment of the impact of plug-in electric vehicles on distribution networks," *IEEE Trans. Power Systems*, vol. 26, no. 1, pp. 206 –213, Feb. 2011.

[30] L. Pierce, "Predicting liquid filled transformer loading capability," *IEEE Trans. on Industry Applications*, vol. 30, Jan/Feb 1994.

[31] Transformers Committee of the IEEE Power Engineering Society, *IEEE Std C57.91-1995: IEEE Guide for Loading Mineral-Oil-Immersed Transformers*. IEEE, 1995.

[32] M. Rutherford and V. Yousefzadeh, "The impact of electric vehicle battery charging on distribution transformers," in *Applied Power Electronics Conference and Exposition (APEC), 2011 Twenty-Sixth Annual IEEE*, March 2011, pp. 396 –400.

[33] K. Clement-Nyns, E. Haesen, and J. Driesen, "The impact of charging plug-in hybrid electric vehicles on a residential distribution grid," *IEEE Trans. Power Systems*, vol. 25, no. 1, pp. 371–380, Feb. 2010.

[34] Y. Cao, S. Tang, C. Li, P. Zhang, Y. Tan, Z. Zhang, and J. Li, "An optimized EV charging model considering TOU price and SOC curve," *IEEE Trans. Smart Grid*, vol. 3, no. 1, pp. 388 –393, March 2012.

[35] S. Shahidinejad, S. Filizadeh, and E. Bibeau, "Profile of charging load on the grid due to plug-in vehicles," *IEEE Trans. Smart Grid*, vol. 3, no. 1, pp. 135 –141, March 2012.

[36] W. Su and M.-Y. Chow, "Performance evaluation of an EDA-based large-scale plug-in hybrid electric vehicle charging algorithm," *IEEE Trans. Smart Grid*, vol. 3, no. 1, pp. 308 –315, March 2012.

[37] E. Sortomme and M. El-Sharkawi, "Optimal charging strategies for unidirectional vehicle-to-grid," *IEEE Trans. Smart Grid*, vol. 2, no. 1, pp. 131 –138, March 2011.

[38] E. Sortomme and M. El-Sharkawi, "Optimal combined bidding of vehicle-to-grid ancillary services," *IEEE Trans. Smart Grid*, vol. 3, no. 1, pp. 70 –79, March 2012.

[39] E. Sortomme, M. Hindi, S. MacPherson, and S. Venkata, "Coordinated charging of plug-in hybrid electric vehicles to minimize distribution system losses," *IEEE Trans. Smart Grid*, vol. 2, no. 1, pp. 198 –205, March 2011.

[40] M. Agsten, S. Schlegel, and D. Westermann, "On the optimization of the load of electric vehicles," *Proceedings of the 18th IFAC World Congress*, vol. 18, 2011.

[41] R. Schwerdfeger, M. Agsten, M. Ifland, S. Schlegel, A.-K. Marten, and D. Westermann, "PHEV and BEV charge management strategies in microgrids," *CIGRE - The Electric Power System of the Future - Integrating super grids and microgrids*, 2011.

[42] A. De Almeida and E. Vine, "Advanced monitoring technologies for the evaluation of demand-side management programs," *IEEE Trans. Power Systems*, vol. 9, no. 3, pp. 1691 – 1697, August 1994.

[43] "Road vehicles – vehicle to grid communication interface," International Organization for Standardization, Standard ISO/IEC CD 15118-3, 2012 (in development).

[44] A. Hilshey, P. Hines, and J. Dowds, "Estimating the acceleration of transformer aging due to electric vehicle charging," *Summer 2011 IEEE PES General Meeting*, 2011.

[45] NEMS. (2001) Reload database documentation and evaluation and use in NEMS. [Online]. Available: http://www.onlocationinc.com/LoadShapesReload2001.pdf

[46] Society of Automotive Engineers, "SAE charging configurations and ratings terminology," *SAEJ1772*, 2011.

[47] K. Morrow and D. Karner, "Plug-in hybrid electric vehicle charging infrastructure review," U. S. Dept. of Energy, Idaho National Laboratory., Tech. Rep., 2008.

[48] G. Swift, T. Molinski, and W. Lehn., "A fundamental approach to transformer thermal modeling–part 1: Theory and equivalent circuit." *IEEE Trans. Power Delivery*, vol. 16, no. 2, pp. 171–175, Apr 2001.

Chapter 3

Data-Driven Thermal Modeling of Residential Service Transformers*

Andrew Seier, Paul Hines, and Jeff Frolik

Abstract

Sales of privately-owned, plug-in electric vehicles (PEVs) are projected to increase dramatically in the coming years; their charging will impact residential service transformer loads. Transformer life expectancy is related to the cumulative effects of internal winding temperatures, which are a function of such loading. Thermal models exist (for example, IEEE C57.91) for predicting these internal temperatures, the most sophisticated being the Annex G model. While this model has been validated with measurements from large power transformers, small residential service transformers have been given less attention. Given increasing PEV loads, a better understanding of service transformer aging could be useful in replacement planning processes. Empirical data from this paper indicate that the Annex G model over-estimates internal temperatures in small, $25\,\text{kVA}$, $65\,^\circ\text{C}$ rise, mineral oil immersed transformers. In order to create a model that is both simpler, and more accurately tracks empirical transformer data, this paper presents a method for modeling service transformers via genetic programming. These results suggest that one can use a fairly simple thermal model in combination with data from advanced metering infrastructure (AMI) to more accurately estimate service transformer lifetimes, and thus more accurately plan for transformer replacement.

1   Introduction

This paper focuses on methods used to estimate the lifetime of service transformers in residential areas. The term *service transformer* is used here to define the pole- or pad-mounted transformers that directly serve residential loads. The service transformers considered in this paper are $25\,\text{kVA}$, $65\,^\circ\text{C}$ rise mineral-oil immersed devices. Though these particular assets are fairly inexpensive–around \$700 for pole-mounted and \$1,500 for pad-mounted plus installation costs–the entirety of the fleet will typically constitute a significant fraction of a distribution utility's physical assets.

Sales of plug-in electric vehicles (PEVs) are expected to greatly increase. Inflating adoption rates are predicted to stress the grid and require distribution transformer replacement [1], [2], [3]. For instance, Level 2 charging of PEVs draws $7.2\,\text{kVA}$ of power from the grid. For a $25\,\text{kVA}$ service transformer, this amounts to 29% of the rated load. The average American household has two

---

vehicles [4]. Given that a single service transformer may serve ten houses, PEV penetration rates of 25% could load a $25\,\mathrm{kVA}$ device to 144% of rated load, if the vehicles charge simultaneously. Because charge times for PEVs are expected to overlap, even low penetrations of PEVs can create harmful overloading for service transformers [5].

Individual power transformers are typically monitored closely as their failure in the grid can be extremely costly to utilities and can cause prolonged outages [6]. The cost of monitoring each service transformer on the network is generally too expensive, computationally or monetarily, and approximations are used to determine device lifetimes. However, a utility that has advanced metering infrastructure (AMI) has access to accurate loading history for its service transformers and can estimate wear based upon these data. The expense of tracking these assets are then mostly computational.

Where loading is known for a transformer, artificial neural networks (ANN) have been proposed to match the loading profile of a new transformer to the loading profiles of transformers in a recorded database to yield an estimate of remaining lifetime of the new device [7]. Because this paper looks at the damage caused by new PEV charging loads, representative databases are likely not available. Also, ANNs do not give the utility an intuitive understanding of how they predict their outcomes. Another approach is to probabilistically estimate the number of transformers that will require replacement as a function of predicted PEV adoption rates as discussed in [2]. While this analysis is helpful to utilities, it only helps for budgeting, leaving the real-time health of specific transformers in question. Finally, since the loading is known on these service transformers, a thermal model can be used which can yield the desired estimates on transformer life while preserving the connection between how the model works and our intuition about how aging occurs in transformers. This approach is usually based on the aging of the insulation paper as a function of loading and ambient temperature.

In general, loading transformers causes heating in the internal windings and degrades the insulating material. The effect of overloading is to cause accelerated aging compared to a unit that is loaded to its rating. If enough overloading accumulates in a single transformer, its lifetime can be significantly curtailed. Transformer aging theory and modeling methods are discussed in the IEEE Guide to Loading Mineral-Oil Immersed Transformers [8]. Due to the internal heating's exponential dependence on transformer loading, energy-equivalent load profiles without peaks are more economic than those with peaks as seen in (3).

This equation set says that if internal heating is an exponential function of load, $L(t)^x$ with $x > 1$, then the least heat would be created by a *flat* loading profile, K. This is important because simultaneously charging PEVs from one service transformer will cause large loading peaks. This means that an accurate estimation of transformer aging starts with some detailed history of transformer loading. If the loading history is known, two models are given by the IEEE loading guide, Clause 7 and Annex G, for calculating transformer aging [8]. The latter model is more complicated, but it is more accurate. Other methods exist which use a circuit model to depict device heating [9], or attempt a complete 3-D dynamic model [10].

$$\text{Let: } \int_0^T L(t)dt = TK \ , \ L(t) > 0 \tag{1}$$

$$\text{Assume: } L(t_1) > K \ , \ t_1 \in [0, T] \tag{2}$$

$$\therefore \int_0^T L(t)^x dt > TK^x \ , \ x > 1 \tag{3}$$

In summary, the use of a thermal model would allow utilities to more closely track their service transformer fleets. Ideally, the model would be concise, intuitive, and accurate so that utilities could track many service transformers with minimal effort. To this end, we propose that there exists a simple thermal model that would track the existing data at least as well as the more complicated Annex G and will better represent heating in service transformers. This model will allow for a computationally inexpensive and accurate description of aging in the service transformer fleet.

This paper is organized as follows, Section 2 describes the data collection process and devices used. Section 3 explains present drawbacks to using the IEEE Annex G model and discusses some motivation for using a genetic program (GP) to find a thermal model for service transformers. Section 4 details the modeling process via an example with data created with the Annex G model. Section 5 explains why this modeling process would be of use to utilities. Finally, Section 6 summarizes the findings of this paper.

2   Data Collection

This paper uses experimental data to validate thermal models for service transformer heating. The following section presents information on how these data were acquired.

Howard Industries smart transformers were used to gather thermal and loading data. When powered, the smart transformers output information about the state of operation of the machine each minute. The key output parameters from the instrumented transformer and accompanying sensors are ambient temperature, internal temperatures, and load. Transformers were installed in two locations in South Burlington, Vermont. The locations of these transformers were chosen to be in areas where loading was expected to peak above the transformer's load rating. Each transformer serves a minimum of eleven homes.

Internal temperature data include the outer low voltage winding (OLVW) temperature which is used in this paper. This reading can be compared with the TW or TO values from the Annex G model, the winding or top oil temperature, respectively. The locations of the temperature probes are shown pictorially in Figure 1.

The data loggers used in this research were Campbell Scientific CR800's which recorded serial output from the smart transformers as well as output from an ambient temperature sensor. The loggers were fitted into voltage regulator boxes that were installed on the utility poles underneath the pole-mount transformers. All measurements are real time values which are collected every minute.

Data collected has shown that during periods of high ambient temperature, loading on the instrumented transformers peaked above the rated loading limit. However, the average loading on the transformers was $9.4 \, \text{kVA}$ over the course of three months of logging.

3   Motivation for a New Model

As mentioned in Section 1, the IEEE has published models to predict the internal temperature of a transformer. The following Section discusses whether the Annex G model may be overly complicated for the purpose of modeling $25 \, \text{kVA}$ service transformers. It also presents evidence that the predictions of the model may be overly conservative, and thus not an accurate representation
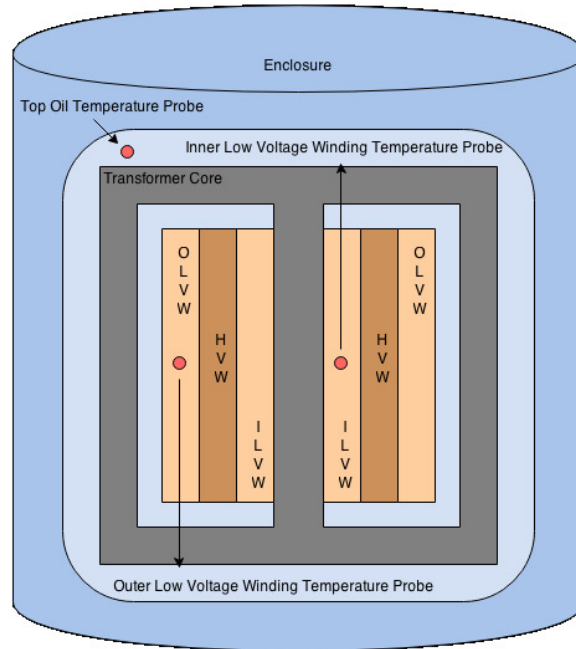
Figure 1: Transformer winding cross-section. The transformers in this work are 1ϕ. Red circles represent where temperature sensors are located in the Howard Industries devices. Windings show are inner low voltage winding (ILVW), high voltage winding (HVW), and outer low voltage winding (OLVW). The upper-left dot represents the Top Oil (TO) temperature.

of the actual internal heating of these units.

3.1 The Annex G Model

For this work, we used the IEEE Annex G model to aid in comparison with previous work [5]. Experimental comparisons for the Annex G model can be found for larger transformers [11]. To our knowledge, there is no existing literature that thoroughly validates the Annex G model for smaller (e.g., $25\,\mathrm{kVA}$) service transformers.

Using data from a representative day, Figure 2 shows a comparison of top oil temperature data which was output from the Annex G model alongside an actual measurement of the top oil temperature data from a smart transformer (refer to Figure 1). Figure 2 also shows a comparison of the Annex G model's prediction for the internal hottest spot temperature and the thermal limit for the hottest spot temperature ($110\,^{\circ}\mathrm{C}$), which when loaded to produces aging at $1\,\mathrm{pu}$ [8]. These data show that during peak loading, the Annex G top oil temperature is overestimating the actual top oil temperature by over $20\,^{\circ}\mathrm{C}$. Also, even if the Annex G hottest spot estimates are correct in Figure 2, this transformer can be loaded much more before accelerated aging will occur. This is because per unit aging is defined as aging in a transformer with a hottest spot temperature of $110\,^{\circ}\mathrm{C}$, the dashed line at the top of Figure 2. Therefore, this transformer could be loaded much more heavily according to the Annex G model predictions, and it shows that these transformers are actually heating less than the model predicts.
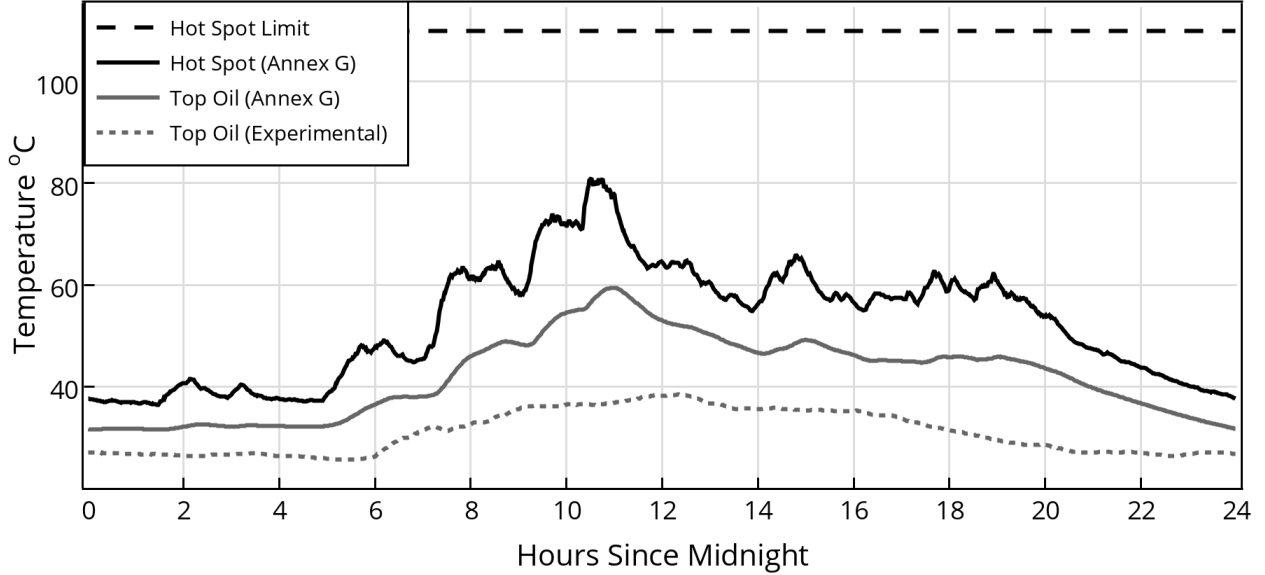
Figure 2: Comparison of Annex G calculated top oil temperature and measured top oil temperature. From top to bottom, the plot shows the thermal hottest spot temperature limit for normal aging of a transformer ($110\,^{\circ}$C), the Annex G prediction for hottest spot temperature, the Annex G prediction for top oil temperature, and the measured top oil temperature. All measurements and predictions depend data collected as described in Section 2.

3.2   Introduction to Using a Genetic Program

A GP will be used in this work to create a list of mathematical structures that attempt to explain the dynamics of a distribution transformer's hottest spot temperature. The merits of genetic programming are well documented [12], [13], [14]. A note is in order of preferring an approach that allows for highly complex and disorderly solution structures. A succinct, physically-appropriate solution is ultimately selected by human intervention. The GP will work to continuously output better solutions and it is the job of the user to pick a reasonably intuitive and concise solution. In this work, a GP called Eureqa Formulize, developed by Nutonian, is used to find underlying structures in the data. The program is based on the work done in [14].

   The solution we will search for in this paper is a single differential equation that reliably yields changes in the internal temperature of a service transformer. To see the utility in this, the reader can refer to the Annex G model which is made up of over 30 equations, many of which are differential equations. In contrast, the solution we seek in this paper is of the form shown in (4).

$$\dot{T_{HS}}(s) = f(T_{HS}(s), L(s), T_A(s)) \tag{4}$$

   To begin the genetic program, a set of solutions of the form shown in (4) are said to make up the *population* of solutions in the first *generation* of the program. Each solution is termed an *individual*. Note that we use s in (4) to emphasize that the data are discrete.

   To assess the *fitness* of each individual in each generation of the GP, the fitness test, $\mathrm{F}(X_{g,i})$, shown in (5) will be used. The individual, $X_{g,i}$, is number i in the gth generation of the GP. The variables we will use are $L(s)$, $T_A(s)$, and $T_{HS}(s)$ for load, ambient temperature, and hottest spot temperature as a function of the discrete variable s, where S is the number of data points we are using in the GP. Every generation, the N individuals are tested and ranked in descending order of
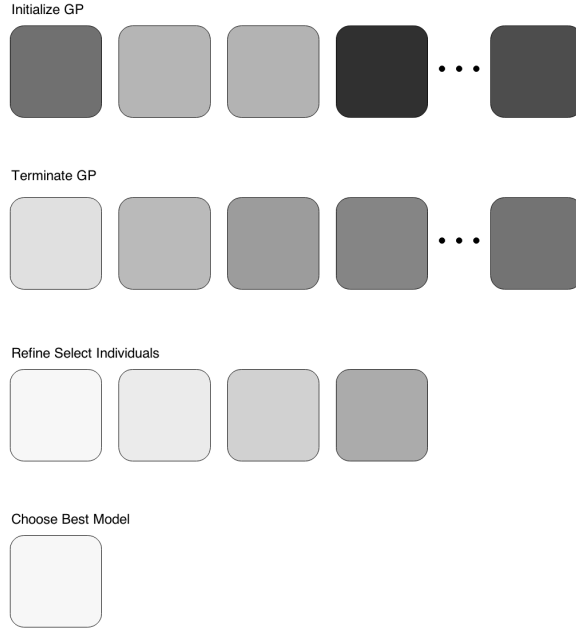
25

Figure 3: The model selection process. Each block is an individual solution with the shade representing its absolute fitness, white meaning zero error. The GP is initialized, a set of fit individuals surfaces and the process is terminated, a subset of fit individuals are further refined using a LMS approach, and a single model is ultimately chosen.

fitness.

$$l\,\mathrm{F}(X_{g,i}) =$$
$$\frac{1}{S}\sum_{s=0}^{S-1}\left(\dot{T}_{HS}(s) - X_{g,i}\left(L(s), T_A(s), T_{HS}(s)\right)\right)^2$$

Fit individuals are propagated through future generations as a function of their relative fitness and new individuals are created by combining aspects of fit individuals. In our work, a set of individual solutions are chosen from the final generation. The coefficients on these solutions are then refined via a least mean-squares (LMS) approach, and one solution is ultimately chosen as a best model for the data.

The process is shown graphically in Figure 3. Each block represents an individual in this process (i.e., a solution modeling the change in hottest spot temperature). The shade associated with each individual represents its mean squared error (MSE).

4   GP Modeling

With regard to the complexity of the Annex G model, the following Section seeks to find a simple thermal model that at least tracks internal temperatures as well as the IEEE Annex G model. The purpose of this Section is to detail a broad approach by which a thermal model can be created to accurately describe the internal heating of service transformers based on user-defined input variables.

We are attempting to model the dynamics of the Annex G model [8]. As such, we need to

start with a hottest spot temperature profile created by this model. To do this, we input ambient temperature data and actual loading data, which was increased to 150% of the measured values to bring the internal temperatures closer to the transformer's limits and expose the dynamics of the model. The Annex G hottest spot temperature (T_{HS}), the ambient temperature (T_A), and the loading (L) are used as inputs to the GP. It should be noted that variables T_O and T_W, which are other outputs from the Annex G model, could have been used as additional inputs to the GP. In this way, we would have to actually model *multiple* differential equations, one for each variable, and come up with a set of equations that would need to be integrated forward together to find the hottest spot temperature, T_{HS}. Again, it is our purpose here to simplify, so we choose to relate the input variables to *one* of the original outputs of the Annex G model, the hottest spot temperature.

Heuristically, we would expect that the change in T_{HS} will depend on the difference between the hottest spot temperature, T_{HS}, and the ambient temperature, T_A. Hence, to simplify the search space, we define T_D as shown in (5), and we seek a differential equation for the change in hottest spot temperature as shown in (6).

$$T_D = T_{HS} - T_A \tag{5}$$
$$\dot{T}_{HS} = f(L, T_D) \tag{6}$$

The allowable operations for these input variables were: addition, subtraction, multiplication, and negation. This search space has closure and it is also reasonable to assume that it is sufficient to describe the dynamics. The justification of sufficiency comes with the acceptance of a model at the end of this Section.

4.1 Running the Genetic Program and Selecting Solutions

After running the GP for over 6 hours with 16 cloud cores, the ten simplest results were identified. They are shown, ordered by complexity and labeled alphabetically (a-j) in Table 1. This table labels each solution equation structure with a letter which will be referenced throughout.

As is common with genetic programs, it is up to the user to select a reasonable solution [12], [13], [15]. Solution (a) from Table 1 is not good selection because it is constant that doesn't depend on any of the input variables. Models (b) and (c) do not depend on T_D, which is connected to T_A, a known input to the Annex G model. Therefore, we do not choose these either. Models (h)-(j) begin to create complicated polynomial fits from the variable L and are also not chosen.

We select the solutions (d), (e), (f), and (g) to move forward with. It will be shown that one of these models can be considered acceptable when compared to the Annex G model in the following subsections. If this were not the case, the next logical step would be to include more of the models from Table 1 to see if any of these yield better results. If no models can ultimately be selected by the end of this process, the assumption is that the solution space is not sufficient and more input variables, beyond our chosen L and T_D, need to be added and the GP must be rerun. For reference, the selected model structures arising from the GP are shown in **bold** in Table 1 along with their resulting models from the training discussed in the following subsection.

4.2 Fitting Selected Structures to Training Data via Least Mean Squares

The next step is to take the structures obtained from running the GP and find a best LMS fit to make the actual models. In making a model, we must train it on certain data and then check its validity

Table 1: Structures arising from GP and four selected structures trained on the data in Figure 4.

ID	Structure for $\dot{T}_{HS}$	Model for $\dot{T}_{HS}$ (Trained in Figure 5)
a	α_1	
b	$\alpha_1 L$	
c	$\alpha_1 L + \alpha_2$	
d	$\alpha_1 L + \alpha_2 T_D$	$0.0367L - 0.0188T_D$
e	$\alpha_1 L + \alpha_2 + \alpha_3 T_D$	$0.0469L - 0.262 - 0.0149T_D$
f	$\alpha_1 + \alpha_2 L^2 + \alpha_3 T_D$	$0.178 + 0.00094L^2 - 0.0149T_D$
g	$\alpha_1 L^2 + \alpha_2 + \alpha_3 T_D^2$	$0.00096L^2 - 0.040 - 0.00022T_D^2$
h	$\alpha_1 L + \alpha_2 L^3 + \alpha_3 T_D$	
i	$\alpha_1 L + \alpha_2 L^4 + \alpha_3 T_D$	

on new data. These models are trained on the inputs shown in Figure 4, where the loading profile is an hour long pulse and the temperature profile is a ramp. During research, training the models with fictitious data like the load pulse and temperature ramp was more successful in finding a best fit. The short load pulse and temperature ramp allows us to separate out dynamics due to loading and temperature differentials.

As specified in [8], emergency overloads are intentional overloads that last for only a short duration. Loading guides in this document cite a maximum emergency overload limit of $2\,\mathrm{pu}$, thus though the load pulse shown is fictitious, it is not an unreasonable estimate to a loading scenario. Loading goes from very underloaded, at $0.5\,\mathrm{pu}$ or $12.5\,\mathrm{kVA}$, to overloaded, at $1.5\,\mathrm{pu}$ or $37.5\,\mathrm{kVA}$. The temperature ramp changes from $0\,^{\circ}\mathrm{C}$ to $40\,^{\circ}\mathrm{C}$ during an interval in the middle of the day. Such low temperatures help the model train when T_D is large, and high temperatures allow the model to train when T_D is small. In Fahrenheit, the temperatures go from $32\,^{\circ}\mathrm{F}$ to $104\,^{\circ}\mathrm{F}$. This ambient temperature spectrum certainly covers the hottest days in a Vermont year, though locals can attest that it does not fully handle the lowest. Again, this training data is meant to have some practical ranges, but need not be experimental for the purposes of training the models.

The Annex G model is then used to predict the hottest spot temperatures throughout the day, shown in Figure 4 (bottom). The models (d)-(g) are then fit to the *change* in the Annex G curve and also shown in Figure 4 (bottom), where they have been integrated forward for comparison of modeled T_{HS} temperatures. Notably, model (d) is the only curve which seems to have a steady state error. Another clarifying point, the models do the *worst* at the beginning of the day when the ambient temperature is low, though all of the models begin with initial conditions from the prior night when ambient temperatures were discontinuously higher as seen in Figure 4 (middle). Abrupt changes like this are included to help train the models by emphasizing the dynamics of the Annex G model, though ambient temperatures do not have such discontinuities in practice. Loading, on the other hand, as expressed in Figure 4 (top) *can* change very rapidly. The LMS fits for the structures obtained from the training portion of this process for the models (d), (e), (f), and (g) are shown in the rightmost column of Table 1.

4.3 Selecting a Final Model Based on Validation

The four models acquired from the training process are then assessed with new a new load profile, Figure 5 (top), and a new temperature profile, Figure 5 (middle). The loading curve here is mea-
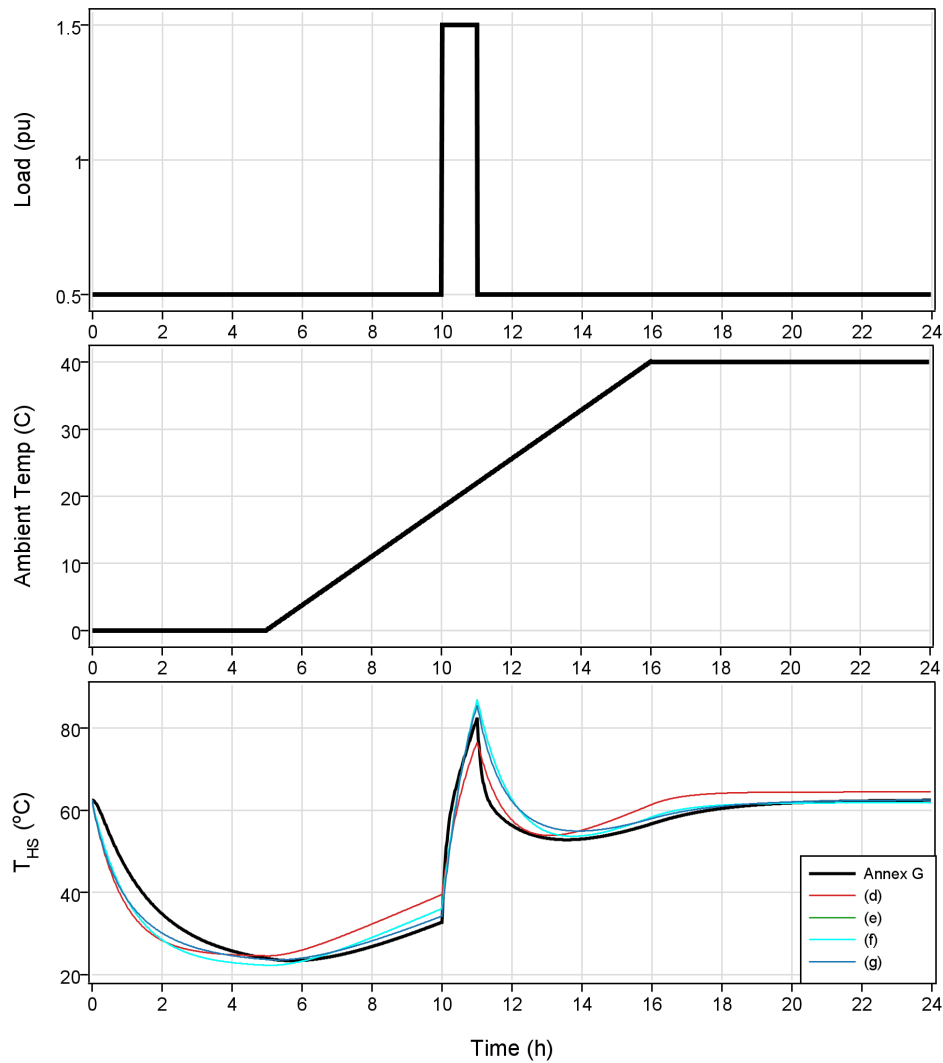
Figure 4: A T_{HS} curve is produced to train structures (d)-(g). The loading profile (top) and ambient temperature profile (middle) are used to create a the Annex G predicted T_{HS} temperature (bottom-black). Coefficients of structures (d)-(g) are set to minimize differential equation error and then integrated forward and are shown compared to the Annex G prediction (bottom-colors).

Table 2: Error table: mean squared-error (MSE) in $^\circ C/\mathrm{min}^2$ and error per point (EPP) in $^\circ C$ from the training (T), the low load (L), and the high load (H). Models refer to those in Table 1.

ID	MSE T	MSE L	MSE H	EPP T	EPP L	EPP H
d	0.0251	0.0272	0.2311	1.2805	0.4796	-6.0791
e	0.0216	0.0214	0.2011	0.0286	1.8721	3.6869
f	0.0216	0.0272	0.1692	0.0286	-1.0069	-1.0193
g	0.0203	0.0265	0.1580	0.2560	0.3465	-3.4269

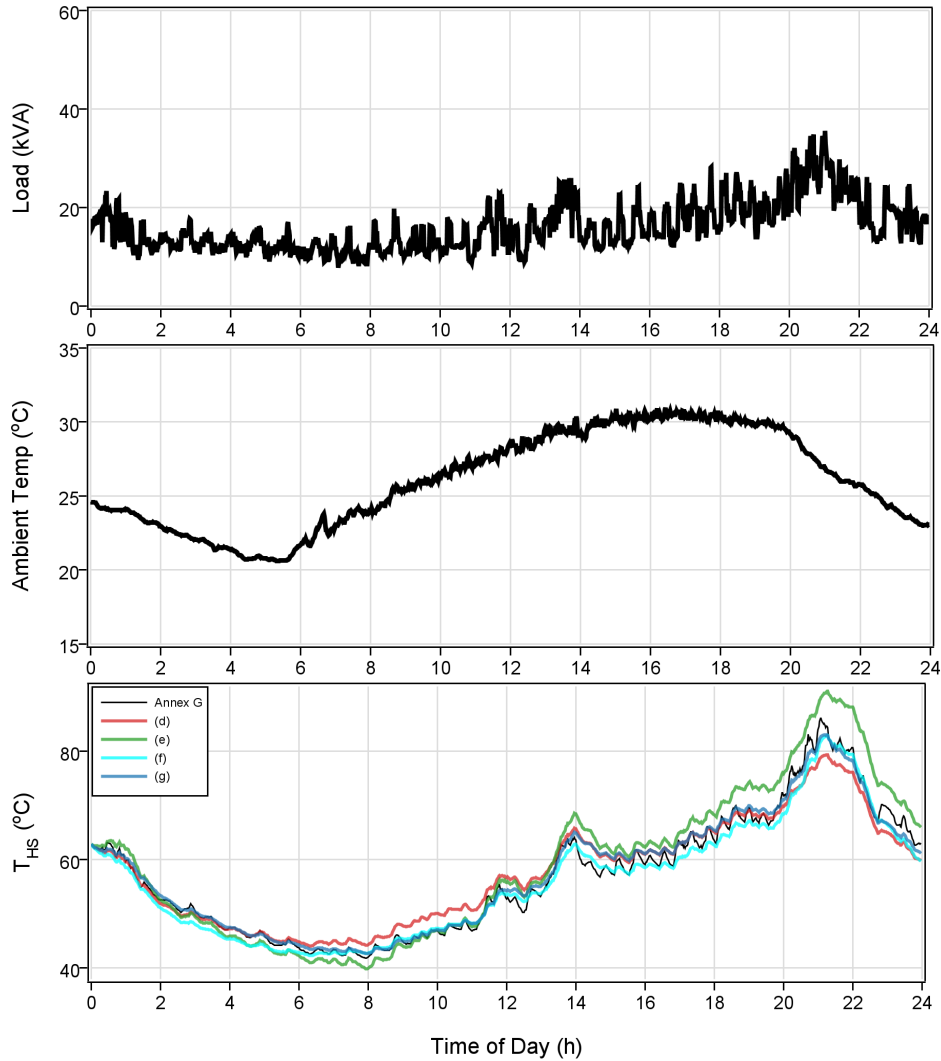Figure 5: Model validation via a comparison with independent T_{HS} predictions for low loading. The loading profile (top) and ambient temperature profile (middle) are used to create Annex G and model (d)-(f) T_{HS} predictions (bottom) to validate the models for low loading scenarios.

sured loading data from one of the smart transformers. This loading is typical of that seen in the experimental neighborhoods where the load breaches the transformer's rated limit only between the hours of $8\,\mathrm{PM}$ and $10\,\mathrm{PM}$. The ambient temperature curve shows that this data was collected on a hot day, at least for Vermont.

Figure 5 (bottom) shows the comparison of the resulting forward integrations of models (d), (e), (f), (g). To create these curves, the Annex G method was used to find an estimate for the transformer's hottest spot to which the models are compared. Model (d) is seen to overestimate the Annex G hottest spot temperature between $8\,\mathrm{AM}$ and $10\,\mathrm{AM}$ and underestimate between the hours of $8\,\mathrm{PM}$ and $10\,\mathrm{PM}$. Model (e) is seen to overestimate the Annex G hottest spot temperature between $2\,\mathrm{PM}$ and $12\,\mathrm{AM}$ the next day and the model does not seem to converge at the end of the day. Model (f) is arguably the best fit, though model (g) is also very good. Though beyond the scope of this paper, validation runs for these models with different loading levels show that model (f) outperforms all of the other models and thus it was selected from the original structures

30

shown in Table 1. A summary of the different model fits is shown in Table 2. This table shows the mean squared error (MSE) for each of the models in training (T), low-load validation (L) which is shown in Figure 5, and high-load validation (H) which is not shown. The MSE has units of $^{\circ}\mathrm{C}/\mathrm{min}^2$ because it is relating to the *change* in the hottest spot temperature. Also tabulated are the error per point (EPP) which is a measure of how symmetric the error is. This number is found by summing the errors and dividing by the number of data points and has units of $^{\circ}\mathrm{C}$. Together the MSE and EPP yield a more complete description of the model's ability to track the Annex G predictions. From Table 2, model (f) has the most consistently low EPP and has low MSE.

4.4   Results from Modeling Approach

This process has shown that many models came organically out of a GP. From these models, four were selected for further study that seemed to be both well related to the physics of the actual problem and reasonably simple. The actual coefficients for these models were thrown away so that the structures were kept. They were then re-fitted with with new coefficients using fictional training data and the least mean squares method. To understand whether these fits worked for the specific data or generally for other data sets, the models were validated by integrating them forward with new data. These results show that, qualitatively, all of the models tracked both the changes in temperature of the hottest spot, as predicted by the Annex G method, as well as the overall accumulated hottest spot temperature. We showed that the best model for the Annex G method was (f) as re-stated in (7). The achievement here is finding a differential equation that use only two measurable inputs, three terms, and still tracks the Annex G output reasonably well for very different loading data sets.

$$\dot{T_{HS}} \approx f(L, T_D) = 0.178 + 0.000939L^2 - 0.0149T_D$$

Recall that the Annex G model is made up of a large set of differential equations. Thus, the model presented in (7) manages to follow the dynamics of the Annex G model's predictions of the hottest spot temperature, Figure 5 (bottom), while being much simpler. Model (f) is not meant to be a replacement for the Annex G model for *all* transformers. However, we have conjectured that a $25\,\mathrm{kVA}$ service transformer may not require the full complexity of the Annex G model and have shown that the structure of model (f), using only *one* differential equation, has been validated to predict hottest spot temperatures in accordance with the IEEE standard model. It should be noted that this model has been trained and validated against the Annex G model for a single set of transformer parameters. This means that the model coefficients may need to be tuned for use with slightly different transformers.

It is important to note that the model in (7) makes some physical sense, given thermodynamics and circuit theory. If we recall the equivalent circuit for a transformer, there are power losses associated with the modeled resistance of the core and the resistance of the winding. These power losses manifest themselves as heating and are proportional to the square of the current through the resistors. Because the voltage at a transformer is relatively constant, the load (L) served by a transformer is proportional to the current through the windings. The power loss in the winding resistance is then proportional to the square of this instantaneous current. Hence, the L^2 term in (7) supports this rationalization. Furthermore, Newton's Law of Cooling tells us that a body cools in proportion to the difference between its temperature and the ambient temperature, i.e., the term T_D from (7) [16]. Finally, the constant in this equation may be an adjusting factor since we are

directly relating an internal temperature to the ambient temperature.

5   Connection to Asset Management

Thus far, we have explained how the Annex G model may not be appropriate for describing the heating measured experimentally in our instrumented service transformers. We have also proposed an approach by which a simple thermal model can be found for service transformers. This Section seeks to explain how a utility would be able to leverage such a model for better asset management of its service transformer fleet.

The large fleet of service transformers owned by utilities is an important subset of assets that must be appropriately managed. Given that the utility in question has already installed AMI, access to loading data for these transformers is relatively inexpensive. This includes getting local ambient temperatures from nearby national weather stations (e.g., the KBTV station for South Burlington). Initial results show that the Annex G thermal model for loading these transformers is overly conservative in that it predicts internal temperatures to be higher than what are experimentally recorded. In addition, the cumbersome nature of the model along with the large number of device-specific constants required, presents a barrier to utilities. The approach to modeling hot-spot temperatures can be used by utilities to find a concise, intuitive model which can leverage loading data.

In this way, utilities see the effect of increased loading from PEV charging as it appears. This requires neither a history of transformer failure as a comparison nor a cumbersome model which is unintuitive and computationally intense. The method only depends on evidence that insulation pyrolysis, the destruction of the material via heating, is the determining factor in transformer aging. With up-to-date information on service transformer aging, utilities can preemptively install additional capacity before certain devices breakdown and appropriately budget for future device purchase and installation.

In addition, the approach explained in this paper is flexible to the input data used. The Annex G model uses only loading and ambient temperature as inputs, though other factors (e.g., wind speed, solar intensity, etc.) may be important in properly modeling transformer heating. By measuring this data and using it as an input to the approach shown in Section 4, such dependencies can be included. For example, work with ANNs has shown that current harmonics in devices may have an effect on heating which is not captured by the Annex G model [17]. Another factor that may be of import is hydrolysis, which has been shown to effect insulation aging for transformers loaded far below their rated limits [18].

Finally, utilities would also have the option to include load management, and control loading based on calculated internal temperatures. Monitoring their transformer fleet in this way would allow for better management because of accurate information and flexibility.

6   Conclusion

Initial data collected for this paper indicate that the Annex G model is overly conservative in that it overestimates internal temperatures for the instrumented $25\,\mathrm{kVA}$ service transformers used in this work (see Figure 2). Because a precise estimate of a transformer's hottest spot temperature is the standard indicator for insulation aging, an approach to finding a more appropriate model was detailed. The approach used a genetic program to remodel output from the Annex G model to indicate the effectiveness of the method. The result of this approach was shown in (7), which

was far simpler than the Annex G model, and tracked the model well. Our existing measurement system did not provide data for hottest spot temperature; collection and modeling of hottest spot data remains for future work.

Given that utilities have increasing access to residential load time-series data and that weather data are readily available, real-time monitoring of service transformers is a realistic goal. If these assets are monitored, utilities can gain information on how much additional loading capacity exists at the residential level to serve predicted PEV charging requirements. They can also closely monitor the aging rates of these devices and make decisions on how to schedule future replacements and upgrade these devices proactively instead of reactively.

Therefore, by leveraging data collected by AMI, utilities can more closely monitor aging in assets that were previously difficult to track.

References

[1] L. Fernández, T. Román, R. Cossent, C. Domingo, and P. Frías, "Assessment of the impact of plug-in electric vehicles on distribution networks," *Power Systems, IEEE Transactions on*, vol. 26, no. 1, pp. 206–213, 2011.

[2] J. Sexauer, K. McBee, and K. Bloch, "Applications of probability model to analyze the effects of electric vehicle chargers on distribution transformers," *Power Systems, IEEE Transactions on*, vol. 28, no. 2, pp. 847–854, May 2013.

[3] Q. Gong, S. Midlam-Mohler, V. Marano, and G. Rizzoni, "Study of PEV charging on residential distribution transformer life," *Smart Grid, IEEE Transactions on*, vol. 3, no. 1, pp. 404–412, 2012.

[4] United States Department of Transportation. Number of households by household driver count. [Online]. Available: http://nhts.ornl.gov/tables09/FatCat.aspx

[5] A. Hilshey, P. Hines, and J. Dowds, "Estimating the acceleration of transformer aging due to electric vehicle charging," in *Power and Energy Society General Meeting, 2011 IEEE*, 2011, pp. 1–9.

[6] M. Pradhan and T. S. Ramu, "On the estimation of elapsed life of oil-immersed power transformers," *Power Delivery, IEEE Transactions on*, vol. 20, no. 3, pp. 1962–1969, July 2005.

[7] J. Jardini, H. Schmidt, C. M. V. Tahan, C. C. B. De Oliveira, and S. U. Ahn, "Distribution transformer loss of life evaluation: a novel approach based on daily load profiles," *Power Delivery, IEEE Transactions on*, vol. 15, no. 1, pp. 361–366, Jan 2000.

[8] "IEEE guide for loading mineral-oil-immersed transformers," *IEEE Std C57.91-1995*, pp. 1–112, 2012.

[9] G. Swift, T. Molinski, and W. Lehn, "A fundamental approach to transformer thermal modeling. I. theory and equivalent circuit," *Power Delivery, IEEE Transactions on*, vol. 16, no. 2, pp. 171–175, 2001.

[10] M. Rosillo, C. Herrera, and G. Jaramillo, "Advanced thermal modeling and experimental performance of oil distribution transformers," *Power Delivery, IEEE Transactions on*, vol. 27, no. 4, pp. 1710–1717, 2012.

[11] D. Susa, M. Lehtonen, and H. Nordman, "Dynamic thermal modelling of power transformers," *Power Delivery, IEEE Transactions on*, vol. 20, no. 1, pp. 197–204, 2005.

[12] J. Koza, *Genetic Programming: On The Programming of Computers by Means of Natural Selection*. MIT Press, 1992.

[13] J. Bongard and H. Lipson, "Automated reverse engineering of nonlinear dynamical systems," *PNAS*, vol. 104, no. 24, pp. 9943–9948, June 2007.

[14] M. Schmidt and H. Lipson, "Distilling free-form natural laws from experimental data," *Science*, vol. 324, no. 5923, pp. 81–85, 2009. [Online]. Available: http://www.sciencemag.org/content/324/5923/81.abstract

[15] H. Kamal and M. Eassa, "Solving curve fitting problems using genetic programming," in *Electrotechnical Conference, 2002. MELECON 2002. 11th Mediterranean*, 2002, pp. 316–321.

[16] L. C. Burmeister, *Convective Heat Transfer*, 2nd ed. Wiley-Interscience, 1993.

[17] J. Pylvanainen, K. Nousiainen, and P. Verho, "Studies to utilize loading guides and ann for oil-immersed distribution transformer condition monitoring," *Power Delivery, IEEE Transactions on*, vol. 22, no. 1, pp. 201–207, Jan 2007.

[18] A. Kachler and I. Hohlein, "Aging of cellulose at transformer service temperatures. part 1: Influence of type of oil and air on the degree of polymerization of pressboard, dissolved gases, and furanic compounds in oil," *Electrical Insulation Magazine, IEEE*, vol. 21, no. 2, pp. 15–21, 2005.

Chapter 4

Effect of Rainfall Transients on Thermal and Moisture Exposure of Underground Electric Cables[1]

Jeffrey S. Marshall and Andrew P. Fuhrmann

Abstract

Cable ampacity analysis is generally performed assuming constant worst-state environmental conditions, which often correspond to a dry soil condition or to a condition with uniform ambient soil moisture content. The characteristic time scale of thermal variation in the soil is large, on the order of several weeks, and is similar to the time scale between rainfall events in many geographic locations. Intermittent rainfall events introduce significant transient fluctuations that influence the thermal conditions and moisture content around a buried cable both by increasing thermal conductivity of the soil and by increasing the moisture exposure of the cable insulation. This paper reports on a computational study of the effect of rainfall events on the thermal and moisture transients surrounding a buried cable. The computations were performed with a finite-difference method using an overset grid approach, with an inner polar grid surrounding the cable and an outer Cartesian grid. The thermal and moisture transients observed in computations with periodic rainfall events were compared to control computations with a steady uniform rainfall. Under periodic rainfall conditions, the temperature and moisture fields are observed to approach a limit-cycle condition in which the cable surface temperature and moisture content oscillate in time, but with mean values that are significantly different than the steady-state values.

Nomenclature

Roman letters

A_g = area of outer grid cell [m^2]

b = cable submergence depth [m]

c_S = specific heat of soil [J/kg $\cdot$ K]

c_w = specific heat of liquid water [J/kg $\cdot$ K]

C = effective soil heat capacity [J/m^3 $\cdot$ K]

C_w = heat capacity of water [J/m^3 $\cdot$ K]

d = cable diameter [m]

D = rainfall duration parameter ($= \tau_R / \tau_L$) [dimensionless]

D_{TL} = liquid thermal migration coefficient $\left[\text{m}^2/\text{s} \cdot \text{K} \right]$

D_{TV} = vapor thermal migration coefficient $\left[\text{m}^2/\text{s} \cdot \text{K} \right]$

D_T = total thermal migration coefficient $\left[\text{m}^2/\text{s} \cdot \text{K} \right]$

$D_{\theta L}$ = liquid isothermal diffusivity $[\text{m}^2/\text{s}]$

$D_{\theta V}$ = vapor isothermal diffusivity $[\text{m}^2/\text{s}]$

D_{θ} = total isothermal diffusivity $[\text{m}^2/\text{s}]$

F = dimensionless rainfall period $(= \tau_P / \tau_L)$ [dimensionless]

f_{out} = heat supply rate to each outer grid cell [W/m^3]

h = convective heat transfer coefficient [W/m^{2}K]

h_{lv} = specific enthalpy of vaporization [J/kg]

H_x, H_y = grid size in x and y-directions [m[

I = rainfall intensity parameter $(= \overline{Q}_{rain} / K_{\theta 0})$ [dimensionless]

K_e = Kersten number [dimensionless]

K_{θ} = hydraulic conductivity [m/s]

L = latent heat of vaporization [J/m^3]

N_c = number of outer grid cells which receive a heat supply [dimensionless]

q_{surf} = cable heat flux per unit depth [W/m^2]

$\overline{q}$ = average cable surface heat flux [W/m^2]

$\mathbf{Q}$ = net water flux [m/s]

Q_{rain} = liquid flux due to rainfall, per unit depth [m/s]

r = radial coordinate [m]

R = cable radius (= d/2) [m]

R_I = radius of inner grid [m]

S = effective saturation $(= \theta / \theta_{sat})$ [dimensionless]

t = time [s]

T = absolute temperature [K]

T_f = temperature value at fringe point [K]

T_0 = ambient temperature [K]

T_{surf} = average temperature around cable surface [K]

x = horizontal coordinate [m]

y = vertical coordinate [m]

v_{max} = maximum liquid velocity magnitude [m/s]

$\mathbf{v}$ = liquid velocity [m/s]

Greek letters

ϕ = azimuthal coordinate [dimensionless]

η = soil porosity [dimensionless]

λ = effective thermal conductivity of soil $[\text{W/m}\cdot\text{K}]$

λ_{dry} = thermal conductivity of dry soil $[\text{W/m}\cdot\text{K}]$

λ_{sat} = thermal conductivity of saturated soil $[\text{W/m}\cdot\text{K}]$

θ = moisture content [dimensionless]

θ_f = value of moisture content at fringe point [dimensionless]

θ_{sat} = moisture content of saturated soil (= η) [dimensionless]

θ_{surf} = average moisture content around cable surface [dimensionless]

ρ_s = effective density of soil [kg/m^3]

ρ_w = density of liquid water [kg/m^3]

τ = time scale [s]

τ_C = convective time scale (= $b/K_{\theta 0}$) [s]

τ_D = diffusive time scale (= $C_0 b^2/\lambda_0$) [s]

τ_L = time scale of daily load variation [s]

τ_R = rain duration time scale [s]

τ_P = time scale between rain events [s]

ξ = dimensionless depth (= $-y/b$) [dimensionless]

1. Introduction

Determination of the current-carrying capacity (or ampacity) of underground electric cables is one of the key factors limiting operation of electric distribution systems, particularly in residential areas. Cable lifespan depends in a nonlinear manner on several factors, primary among which are insulation temperature, electric stress magnitude, and exposure of insulation to moisture (Hyvönen, 2008). The effect of temperature on insulation lifespan is often approximated by an exponential (Arrhenius) expression (Montanari et al., 2002; Mazzanti, 2007, 2009), so that the peak temperature values have a disproportionately large influence on lifespan degradation compared to the average temperature value. In order to reduce peak temperatures, ampacity is usually set for cable systems based on worst-case environmental conditions, usually consisting of dry conditions or conditions with uniform background soil moisture content. Water has a duel role on the cable lifespan. On the one hand, the thermal conductivity of soil is substantially increased by the presence of water, with an increase of an order of magnitude or more between dry and saturated conditions for many soils (Hamdhan and Clarke, 2010). As a consequence, the presence of water decreases insulation temperatures, which has a favorable effect on cable lifespan. On the other hand, exposure to water can give rise to formation of water treeing degradation within the cable insulation (Hyvönen, 2008), which over time can lead to deterioration of the insulation material and shortening of the cable lifespan.

The increasing availability of plug-in electric vehicles (PEVs) is expected to substantially increase electric loads in the near future, particularly within residential communities where underground cable systems are commonly used (Fernández et al., 2011; Webster, 1999; Clement-Nyns et al., 2010). Moreover, the electric load associated with PEVs has large stochastic variation, depending on the percentage of a community that has electric vehicles. In order to accommodate residential PEVs while minimizing the cost of upgrading infrastructure, new charge-control schemes have been proposed to better manage electricity availability in distribution systems without exceeding load limits (Rezaei et al., 2014).

In the presence of large fluctuations of the electric load, it is important to have a good understanding of other transients imposed on the heat and moisture transfer around the cable, the most important of which originate from intermittent rainfall events. Rainfall is a key factor in determination of cable temperature and water exposure under actual environmental conditions. In many geographic areas around the world, between 25-40 rainy days during a year account for

two-thirds of the total annual precipitation (Sun et al., 2006). This range corresponds to a typical average interval of 9-14 days between significant rainfall events. The range of time intervals associated with rainfall events is therefore similar to the time scale associated with heat transfer in the soil surrounding an underground cable (Anders, 1997), with the consequence that the temperature field around underground cables in regions with frequent rainfall may be nearly always in a transient state, influenced on a short time scale by the daily load variation and on a longer time scale by soil moisture variation associated with rainfall.

There is a substantial literature on prediction of cable ampacity based on thermal analysis within cables and the soil surrounding the cables. A survey of steady-state analytical methods is given by Neher and McGrath (1957), which has also been extended to transient problems (Neher, 1964; Anders and El-Kady, 1992; Liang, 1999; Black and Park, 1983). These analytical models are subject to a number of simplifications, including the assumption that the ground surface is an isotherm, that cables are a line source of heat, and for transient calculations, that the heat source changes as a series of discrete step functions. Numerical solutions for cable thermal fields have been reported using the finite-element method (Flatbo, 1973; Kellow, 1981; Nahman and Tanaskovic, 2012), the finite-volume method (Freitas et al., 1996), and a boundary-element method (Gela and Dai, 1988). Application of overset grid methods to cable thermal analysis were reported by Garrido et al. (2003), Vollaro et al. (2011), and Marshall et al. (2013). Overset grid methods are well suited for cable heat transfer problems since the characteristic length scale for heat transfer varies over a large range, from the cable diameter to the submergence depth of the cable. Problems with soil heterogeneity on cable heat transfer were examined by Tarasiewicz et al. (1985) and Hanna et al. (1993), and nonlinear effects due to temperature-dependent insulation electrical resistance was examined by Kovač et al. (2006).

The effect of moisture variation on underground cable thermal fields was first examined computationally by Anders and Radhakrishna (1988) using a finite element method, and later by Freitas et al. (1996) using a finite volume method. Both of these studies neglect thermal convection caused by fluid velocity associated with moisture gradients, and they assume that the ambient moisture level is uniform. Specifically, the studies assume that no additional moisture is added to the system at the soil-air interface (i.e., no rainfall). A primary observation of these studies is the formation of a local dry region surrounding an underground cable, within which the temperature gradient associated with the cable thermal field causes moisture to migrate away from the cable. The presence of this dry region decreases the soil thermal diffusivity in the region surrounding the cable, which in turn increases the cable surface temperature. Moya et al. (1999) report an experimental study of heat and moisture transport around a heated cylinder in unsaturated soil. The experimental results are found to compare well with numerical computations using a finite-volume method. The paper concluded that the primary influence of moisture on the cable surface temperature is through the influence of moisture on the soil thermal conductivity. This observation might seem to justify the common approach of simply prescribing a conservative thermal conductivity value for the soil and determining ampacity using only solution of the thermal equation. However, one problem with that approach is that cable insulation degradation is sensitive not only to thermal conditions, but also to water exposure. Accurate calculation of cable moisture exposure in realistic weather conditions is critical in order to adequately characterize degradation associated with these two variables.

The current paper examines the effect of transients caused by rainfall events on the temperature and moisture fields surrounding an underground cable. Of particular interest is the effect of a rainfall front on the dry region surrounding the cable, and the transients caused by

passage of rain fronts at different rainfall intensities, durations, and frequencies. A two-dimensional finite-difference model is used to simulate both the temperature and moisture fields surrounding an underground cable. The top boundary condition for the moisture field at the soil-atmosphere interface is varied to represent effect of rainfall of different intensity, duration, and frequency. Unlike most studies of combined moisture/thermal cable analysis, we retain the thermal convection term in the temperature governing equation to account for the short time scales of the rain front. The significance of the thermal convection term is examined by comparing simulations both with and without this term.

A summary of the governing equations and boundary conditions, and of the computations method used to solve thee equations, is given in Section 2. This section also includes results of a grid independence study and an evaluation of the importance of thermal convection on the cable surface temperature. The results of the paper are presented in Section 3, including comparison of steady-state calculations with constant rainfall rate with periodic rainfall cases having rainfall events with different intensity, duration, and frequency. Conclusions are given in Section 4.

2. Computational Method

Governing Equations

The governing equations for heat and moisture transfer within the ground are given by the coupled system derived by Philip and de Vries (1957) as

$$C\frac{\partial T}{\partial t}+C_w\mathbf{v}\cdot\nabla T=\nabla\cdot(\lambda\nabla T)+\nabla\cdot(L\,D_{\theta V}\nabla\theta),\tag{1}$$

$$\frac{\partial\theta}{\partial t}=\nabla\cdot(D_T\nabla T)+\nabla\cdot(D_\theta\nabla\theta)+\frac{\partial K_\theta}{\partial y},\tag{2}$$

where $T(\mathbf{x},t)$ is the temperature field and $\theta(\mathbf{x},t)$ is the volumetric moisture content. The various coefficients in (1)-(2) include the volumetric heat capacity of wet soil C, the volumetric heat capacity of water C_w, the water velocity vector $\mathbf{v}$, the unsaturated hydraulic conductivity K_θ, the soil thermal conductivity λ, the latent heat of vaporization of water L, the thermal moisture diffusivity D_T, the isothermal moisture diffusivity D_θ, and the isothermal vapor diffusivity $D_{\theta V}$. Equation (1) is derived from the conservation of energy, where the second term on the left-hand side represents thermal convection by the liquid motion, and on the right-hand side, the first term represents thermal diffusion, and the second term represents energy transfer via latent heat of the vapor caused by a moisture gradient.

Equation (2) is derived from a combination of the continuity equation and an extension of Darcy's law to unsaturated media. The continuity equation gives an expression for the rate of change of the moisture content as

$$\frac{\partial\theta}{\partial t}+\nabla\cdot\mathbf{Q}=0,\tag{3}$$

where $\mathbf{Q}$ is the net water flux (defined to be positive upward), which is equal to the product of the water velocity $\mathbf{v}$ and the soil porosity η. An equation for $\mathbf{Q}$ was derived by Philip and de Vries (1957) in terms of the temperature and moisture gradients as

$$\mathbf{Q} = \mathbf{v}/\eta = -(D_T \nabla T + D_\theta \nabla \theta + K_\theta \mathbf{e}_y), \tag{4}$$

where the first and second terms on the right-hand side are associated with transport of water by capillary action and the third term is associated with gravitational transport. Substituting this expression into the continuity equation (3) gives the moisture balance equation (2). Equations (1)-(2) are the same equations used by previous investigators for cable ampacity computation (Anders and Radhakrishna, 1988; Freitas et al., 1996; Moya et al., 1999), with the difference that we have also included the thermal convection term in order to properly account for the effect of rainfall on the temperature field.

The coefficients λ, D_T, D_θ, L, C, $D_{\theta V}$, and K_θ are functions of the temperature and moisture content. Since analytical expressions for these coefficients are difficult to obtain, it is common practice to evaluate them using empirical formulas developed for specific soil types. In the current study, a representative backfill soil was selected, which is identified as Soil III by Anders and Radhakrishna (1988). This soil is described as well-graded with course to fine particles, such as is found in a silty sand or a sandy loam. The equations used for the coefficients for this soil type are given by Anders and Radhakrishna (1988) as

$$\begin{aligned} \lambda &= (\lambda_{sat} + \lambda_{dry})K_e + \lambda_{dry}, \\ D_T &= D_{TL} + D_{TV}, \qquad D_\theta = D_{\theta L} + D_{\theta V}, \\ L &= \rho_w h_{lv}, \qquad\qquad C = \rho_s c_S + \rho_w c_w \theta \end{aligned} \tag{5}$$

where $K_e = \log S + 1$, $S \equiv \theta/\theta_{sat}$, and the various coefficients in (5) are given in Table 1. The empirical equation for effective thermal conductivity in (5) is restricted to $S \geq 0.1$. When $S < 0.1$, the soil is nearly dry, so we set $\lambda = \lambda_{dry}$ in the computations.

Table 1. Expressions used for the variable coefficients that characterize heat and moisture transport in the soil as functions of temperature T (in degrees Kelvin) and relative moisture content $S \equiv \theta/\theta_{sat}$. The different coefficients are in SI units, as indicated in the nomenclature section.

Variable Parameters		Constant Parameters
$D_{TL} = \exp(8.01\,S - 26.96)$		$\theta_{sat} = 0.45$
$D_{TV} = \exp(-1.416\,S - 23.316)$		$\lambda_{dry} = 0.3$
$D_{\theta L} = \exp(8.06\,S - 18.19)$		$\lambda_{sat} = 1.6$
$D_{\theta V} = \exp(-7.483\,S - 27.792)$		$\rho_s = 1800$
$h_{lv} = 2.496\times10^{-6} - (0.00237)T$		$\rho_w = 1000$
$K_\theta = 10^{-6}\,S^6$		$c_S = 1480$
		$c_w = 4216$

Computational Approach

The numerical computations are performed on both an outer Cartesian grid and on an inner polar grid surrounding a single buried cable, as shown in Figure 1. The outer grid has boundaries at $x = \pm\frac{1}{2}H_x$ in the horizontal direction, and it extends from the ground to a depth $y = -H_y$. The four boundaries of the outer grid are identified by circled numbers [1] - [4] in Figure 1. On the bottom boundary [4], the temperature is set to a prescribed value T_0 and the moisture content is governed by a flux balance of the form

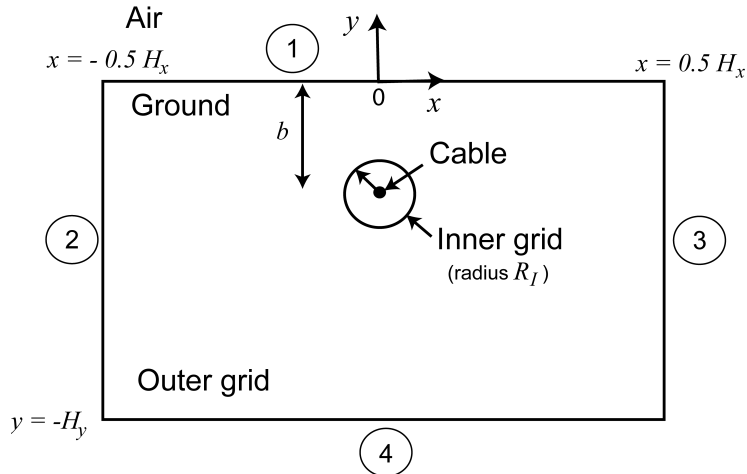$$D_T \frac{\partial T}{\partial y} + D_\theta \frac{\partial \theta}{\partial y} = -K_\theta . \tag{6}$$

Figure 1. Schematic diagram of the computational flow domain and the inner (polar) and outer (Cartesian) grids, where the cable is identified as a black circle at the center of the inner grid, which is submerged a depth b below the ground. The boundaries of the outer grid are identified by circled numbers.

Zero-flux boundary conditions are used for temperature on the side boundaries [2] and [3], so that $\partial T / \partial x = 0$. The side boundary condition for moisture is again based on the flux balance, and is given by

$$D_T \frac{\partial T}{\partial x} + D_\theta \frac{\partial \theta}{\partial x} = 0 . \tag{7}$$

A convective boundary condition for temperature is used on the top boundary [1], which has the form

$$\lambda \frac{\partial T}{\partial y} + h(T - T_{atm}) + LD_{\theta V} \frac{\partial \theta}{\partial y} = 0 , \tag{8}$$

where h is the surface heat transfer coefficient and T_{atm} is the atmospheric temperature. The third term is included along with the tradition convective boundary equation to account for the transfer of latent heat by vapor migration. The boundary condition for moisture content on the top boundary [1] is

$$D_T \frac{\partial T}{\partial y} + D_\theta \frac{\partial \theta}{\partial y} + K_\theta = Q_{rain} , \qquad (9)$$

where $Q_{rain}(t)$ denotes the prescribed time-varying flux of water supply by rain on the top boundary.

The outer Cartesian grid computations are performed by introducing a heat source for grid cells of the outer grid that overlap the cable cross-section. The heat supply rate to each outer grid cell, f_{out}, is related to the cable surface heat flux q_{in} by

$$2\pi R q_{in} = N_c A_g f_{out} , \qquad (10)$$

where R is the cable radius, N_c is the number of outer grid cells which receive a heat supply, and A_g is the area of one cell of the outer grid.

The outer grid yields an accurate solution for heat and moisture transport in the region sufficiently far away from the cable, but it does not satisfy the boundary conditions on the cable surface. In order to obtain a more accurate solution near the cable, we use an overset inner grid in an annular region spanning from the cable radius R to the outer radius R_I of the inner grid. The center of the inner grid is located a distance b below the ground level, where b is called the cable burial depth. Within this inner grid, the temperature and moisture content fields are discretized using a polar coordinate system (r, ϕ). The inner grid solution satisfies the flux boundary condition in temperature and the no-penetration condition for moisture on the cable surface, so that

$$-\lambda \frac{\partial T}{\partial r} = q_{in}, \qquad \frac{\partial \theta}{\partial r} = 0 \qquad \text{on } r = R . \qquad (11)$$

The two grids communicate on the set of grid points on the outer boundary of the inner grid ($r = R_I$), which are called *fringe points*. At each time step, we first solve for the temperature and moisture fields on the outer grid, and then use a bilinear interpolation to set the values of T and θ at the fringe points of the inner grid, denoted by T_f and θ_f. The inner solution is then solved using a Dirichlet boundary condition on its outer surface of the form

$$T = T_f, \qquad \theta = \theta_f \qquad \text{on } r = R_I . \qquad (12)$$

The governing equations (1)-(2) for temperature and moisture content were solved within both the inner and outer grids using a Crank-Nicholson method for the diffusive terms and a second-order Adams-Bashforth method for the convective term, with the velocity given by (4).

Spatial derivatives were computed using second-order centered differences in both grids. The resulting system of equations was solved using a Gauss-Seidel iteration method, which was written such that computations are performed only with non-zero matrix elements. It is noted that (1) approaches a first-order hyperbolic equation in the absence of the diffusive terms, for which the numerical method described above would not be stable. This numerical instability was not an issue in the current computations, however, since the scale of the problem is fairly small (ranging from centimeters to tens of meters) and the diffusive terms were consequently sufficiently large to suppress the instability. The CFL number $v_{max} \Delta t / \Delta x$ was monitored for all computations and did not exceed 0.002.

Dimensionless Parameters

The problem depends upon two dominant length scales - the cable diameter d and the cable submergence depth b. The cable diameter characterizes small-scale fluctuations of temperature and moisture around the cable, such as are associated with power load fluctuations during a daily cycle, but the submergence depth is more characteristic of the thermal and moisture fields as a whole.

Three characteristic time scales in the problem are referred to as the convective time scale τ_C, the diffusive time scale τ_D, and the load-variation time scale τ_L. If we select b as a characteristic length scale, the *convective time* $\tau_C = b / K_{\theta 0}$ is the typical time required for a rain front to propagate from the ground to the cable location, where $K_{\theta 0}$ is characteristic of the velocity scale caused by gravitational drainage. The *diffusive time* $\tau_D = C_0 b^2 / \lambda_0$, where λ_0 / C_0 is a characteristic thermal diffusivity, is representative of the time required for the thermal field to attain a steady state upon change of the cable heat flux or of the surrounding moisture field. The *load-variation time* τ_L represents the period of oscillation of the cable heat load, where we make the common assumption that the cable load is periodic on a daily cycle. For typical conditions, τ_C is on the order of 11 days, τ_D is on the order of 20 days, and τ_L is 1 day. The addition of rain at the top boundary introduces other time scales which can be compared to the three time scales described above. These additional scales include the rain duration time τ_R and the period between rain events τ_P, both of which are examined in the paper.

A set of dimensionless variables are defined using the cable submergence depth b as a length scale, the load-variation time τ_L as the time scale, the average cable surface heat flux $\bar{q}$, and the ambient temperature T_0. The resulting dimensionless variables (denoted with primes) are defined by

$$T' = \frac{\lambda_0}{\bar{q} b}(T - T_0), \quad \nabla' = b \nabla, \quad dt' = dt / \tau_L, \quad x' = x / b, \quad y' = y / b,$$

$$\mathbf{v}' = \mathbf{v} / K_{\theta 0}, \quad f'_{out} = \frac{b}{\bar{q}} f_{out}, \quad q'_{in} = q_{in} / \bar{q}, \quad Q'_{rain} = Q_{rain} / K_{\theta 0},$$

$$C' = C / C_0 \quad \lambda' = \lambda / \lambda_0 \quad L' = L / L_0 \quad D'_V = D_V / D_{V0},$$

$$D'_T = D_T / D_{T0}, \quad D'_\theta = D_\theta / D_{\theta 0}, \quad K'_\theta = K_\theta / K_{\theta 0}. \tag{13}$$

A subscript "0" is used to denote constant nominal values of the coefficients, where these nominal values are set equal to the coefficient values under saturated soil conditions (obtained from (5) and Table 1 with $S = 1$).

The dimensionless governing equations and boundary conditions contain a number of different dimensionless parameters. In the current paper, we hold many of these dimensionless parameters constant in order to focus on a small number of parameters that characterize the rainfall. Characteristic values of these dimensionless parameters are obtained for a typical 5kV distribution cable (e.g., a tape-shielded 5kV 4/0 AWG aluminum conductor), for which the average cable diameter is $d = 2.5$ cm, the burial depth is $b = 1$ m, and a typical cable surface heat flux is $\bar{q} = 500$ W/m^2 for an average-size residential community (Marshall et al., 2013). Using a typical value for thermal conductivity of fully saturated soil of $\lambda_0 = 1.6$ W/mK, we obtain a relationship between a change in the dimensionless temperature $\Delta T'$ and the dimensional temperature ΔT as $\Delta T = (312.5°C)\Delta T'$. A list of constant dimensionless parameters and the values used for these parameters in the current computations is given in Table 2. The dimensionless parameters that are allowed to vary in the computations include the rainfall intensity, the rainfall duration parameter $D_{rain} = \tau_R / \tau_L$, and the dimensionless rainfall frequency $f' = f\tau_L$.

Table 2. List of dimensionless parameters whose values are held fixed, and their values in the current computations.

Parameter Name	Equation	Typical Value
H_{conv}	$\dfrac{hb}{\lambda_0}$	2.8
c_1	$\dfrac{\tau_L \lambda_0}{C_0 b^2}$	5.2×10^{-2}
c_2	$c_1 c_7$	1.2×10^{-10}
c_3	$\dfrac{\tau_L \bar{q} D_{T0}}{\lambda_0 b}$	0.16
c_4	$\dfrac{\tau_L D_{\theta 0}}{b^2}$	3.5
c_5	$\dfrac{\tau_L K_{\theta 0}}{b}$	8.6×10^{-2}
c_6	$c_5 \dfrac{\rho_w c_w}{C_0}$	0.14
c_7	$\dfrac{L_0 D_{V0}}{\bar{q} b}$	2.4×10^{-9}
c_8	$\dfrac{\lambda_0 D_{\theta 0}}{D_{T0} \bar{q} b}$	22
m_1	$\dfrac{\bar{q} D_{T0}}{\lambda_0 K_{\theta 0}}$	1.9
m_2	$\dfrac{D_{\theta 0}}{K_{\theta 0} b}$	40

Grid Independence and Validation

A grid independence study was performed to examine sensitivity of the computations to number of grid points in the inner and outer grids. Since the focus of the study is on effect of soil characteristics and rain on the thermal and moisture exposure of a buried cable, the grid independence study examines the effect of grid resolution on the average temperature and moisture content on the cable surface as a function of time. The test computation used for the grid independence study was conducted for a case where the initial temperature field is set equal to the ambient temperature ($T'(x,0) = 0$) and the initial moisture content was $\theta(x,y) = 0.1$. The domain size was $H_x/b = 5.0$ and $H_y/b = 3.0$, with a cable diameter $d/b = 0.0249$ and an inner grid radius $R_I/b = 0.0747$. The cable surface heat flux was held constant ($q'_{surf} = 1$) and the rain flux was set at $Q'_{rain} = 0.5$. The time step was fixed as $\Delta t' = 0.002$, and the runs were continued out to $t' = 20$. The number of grid points in the inner grid was set such that the grid spacing at the outer edge of the inner grid in both the radial and azimuthal directions was similar to the grid spacing used in the outer grid. In the grid independence study, the number of points in the inner and outer grids were varied in the same proportion. Three different grids were examined in the study, with grid point numbers in each direction in the inner and outer grids listed in Table 3. Results for the average cable surface temperature and moisture content are plotted in Figure 2 as functions of time for each grid. For the finest two meshes, the maximum difference in cable surface temperature was 0.5% and the maximum difference in moisture content was 1.1%. The computations in the remainder of the paper were performed on the medium-resolution mesh B.
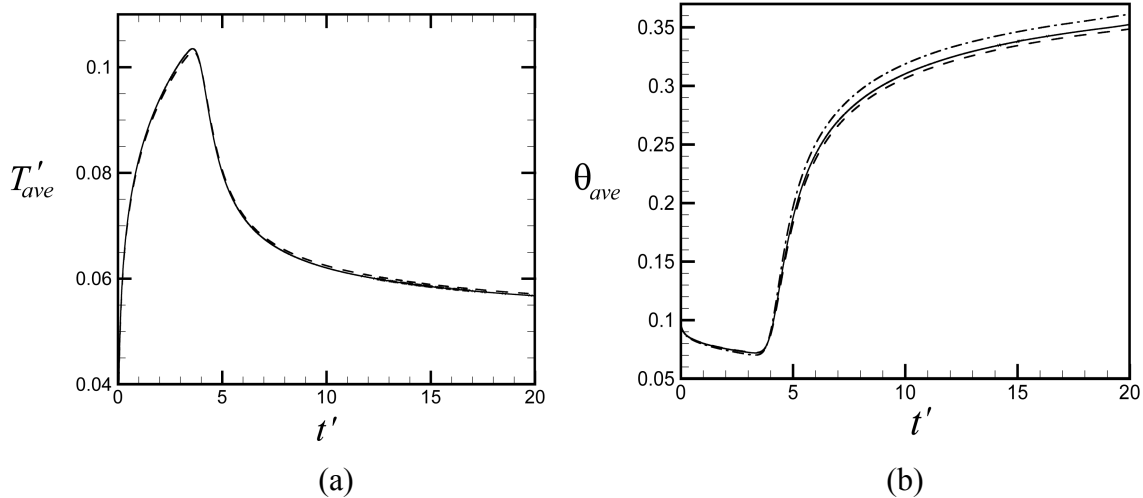

(a) (b)

Figure 2. Time variation of the average cable surface temperature and moisture content for the grid independence study, for grids A (dash-dot), B (solid), and C (dashed).

The sensitivity of the temperature field to the thermal convection term was examined by repeating the computation described above with grid B but with no thermal convection term. The prediction for the average dimensionless temperature on the cable surface is compared with the result with the thermal convection term in Figure 3. It is observed that the results are similar for the runs with and without convection during the initial part of the calculation as the cable

temperature increases before the rain front penetrates to the cable location. At about $t' = 4$, the cable temperature abruptly begins decreasing, coinciding with the abrupt increase in moisture content observed in Figure 2b associated with arrival of the moisture front from the rainfall event at the cable location. Following this time, the predictions with and without the convection term in Figure 3 exhibit significant differences. The most noticeable of these differences is that the cable temperature prediction without convection rapidly asymptotes to a constant value following arrival of the moisture front, whereas the cable temperature prediction with convection exhibits a gradual decrease with time.
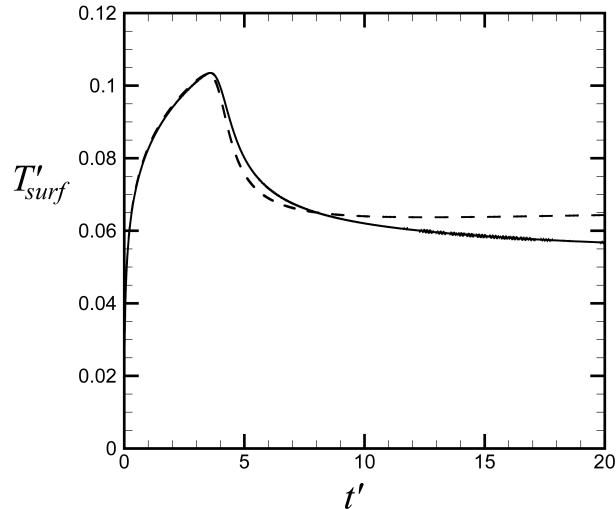

Figure 3. Comparison of predicted dimensionless average cable surface temperature for a case with the thermal convection term (solid line) and without the thermal convection term (dashed line) for the same run as shown in Figure 2.

3. Results and Discussion

Computational results are reported in this section for thermal and moisture fields around underground cables with periodic rainfall events. The rainfall intensity, duration, and period are all varied in such a way that the average rainfall is held constant, and the results are compared to computations with constant average rainfall in order to determine the transient effects caused by rainfall events.

Initialization

The computations are initialized using two sets of preliminary computations. The first preliminary computation is performed with the outer grid only for constant rainfall and with no cable present. Since this problem is essentially one-dimensional, the outer grid is reduced to 637 points in the y-direction and 11 points in the x-direction for the first preliminary computation. The constant rainfall rate is determined by dividing the average annual precipitation in different regions by the number of days in a year, and then non-dimensionalized to obtain $\overline{Q}'_{rain}$, where the overbar denotes average value. Computations were performed with $\overline{Q}'_{rain} = 0.005$, 0.01, 0.02, and 0.03, as well as the case with no rain ($\overline{Q}'_{rain} = 0$). The case with $\overline{Q}'_{rain} = 0.03$ corresponds to a precipitation of 95 cm/yr, which is typical of Chicago, whereas that with $\overline{Q}'_{rain} = 0.01$

corresponds to a precipitation of 32 cm/yr, which is typical of Los Angeles. For simplicity, rainfall is spread throughout the year and seasonal variations are ignored. Each computation is initialized using a uniform moisture content of $\theta_0 = 0.1$ and temperature set equal to the ambient value. The computations are continued until a steady-state condition is achieved in the value of moisture content to at least four significant figures. The case with no rain did not achieve a steady-state value even after very long time, but instead decreased very slowly with time in a continuous manner. The steady-state moisture profiles for the four cases with non-zero values of $\overline{Q}'_{rain}$ are plotted as functions of the dimensionless depth $\xi \equiv -y/b$ in Figure 4. The line denoted by 'E' in this figure shows the moisture content profile for the case with no rain at a time approximately 10 years after the initial condition.
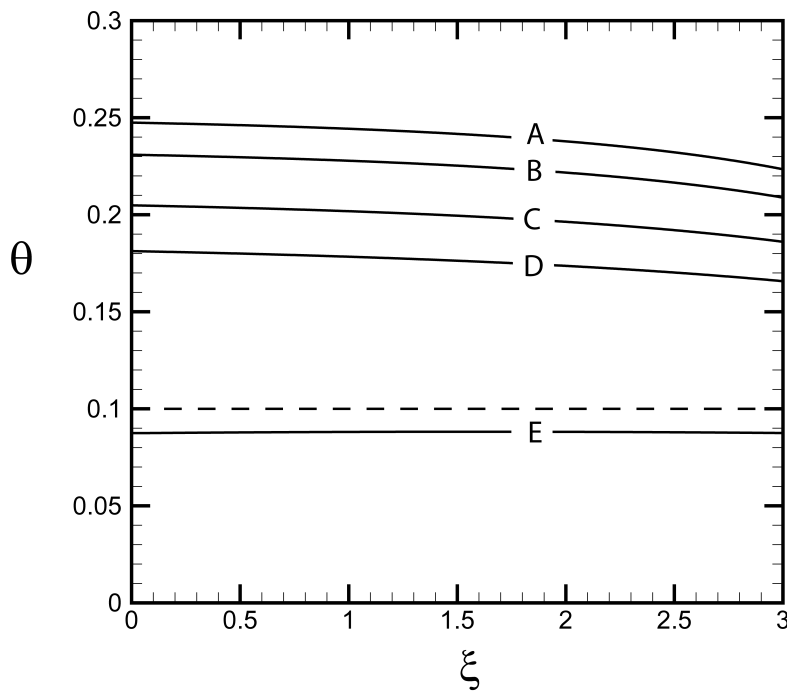

Figure 4. Steady-state moisture content profiles for cases with (A) $\overline{Q}'_{rain} = 0.03$, (B) 0.02, (C) 0.01, (D) 0.005, and (E) 0 as a function of dimensionless depth ξ. The initial moisture profile in the calculations is indicated by a dashed line. For the case with no rain, the moisture content moves downward very slowly in time and no steady-state profile is observed. The moisture profile shown in E is plotted at a time of approximately 10 years after the initial condition. The other cases have all converged to steady-state profiles within four significant figures in the moisture content.

The second preliminary computation reads in the equilibrium moisture content profile for the selected average rainfall rate, and then introduces the cable with a constant surface heat flux using both the outer and inner grids with the number of grid points set equal to the values stated for grid B in Table 3. In the second preliminary computation, the rainfall rate is held constant at the same average value as used for the first computation. The computations are continued until both the temperature and moisture content fields have achieved steady-state values. The time

47

variation of the average temperature and moisture content on the cable surface are plotted in Figure 5 as functions of time for the four cases with non-zero rainfall shown in Figure 4, showing the approach of the results to a steady-state condition. In Figure 5a, the dimensionless temperature is shown on the left-hand y-axis and the corresponding change in dimensional temperature (in $°C$) for the example problem with $\bar{q} = 500\,\text{W/m}^2$, $b = 1\,\text{m}$, and $\lambda_0 = 1.6\,\text{W/mK}$ is shown on the right-hand y-axis.

Table 3. Number of points in different grids used in grid independence study.

Grid Identification	Outer Grid		Inner Grid	
	x	y	r	ϕ
A	651	451	37	63
B	921	637	53	89
C	1029	711	59	99

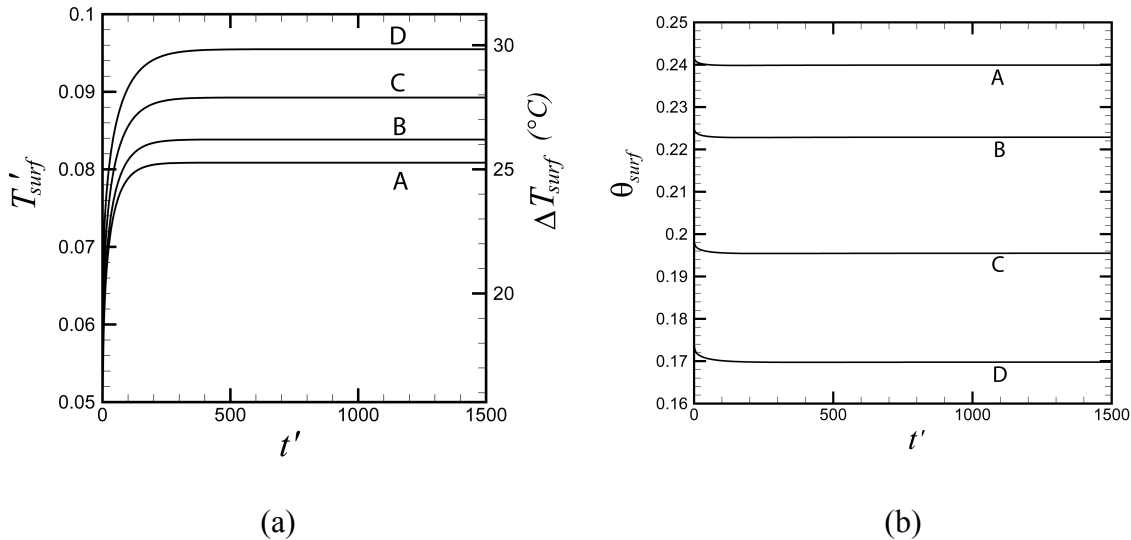(a)   (b)

Figure 5. Time variation of the average cable surface (a) temperature and (b) moisture content during the second preliminary computation for cases with (A) $\bar{Q}'_{rain} = 0.03$, (B) 0.02, (C) 0.01, and (D) 0.005. In (a), the dimensionless temperature is shown on the left-hand y-axis and the corresponding change in dimensional temperature for the example problem is shown on the right-hand y-axis. The figure shows the approach of the temperature and moisture content fields to a steady state condition.

The contours of the steady-state temperature and moisture content around the cable are plotted for the case with $\bar{Q}'_{rain} = 0.03$ in Figure 6. In this figure, the near-cable inner grid is superimposed on the outer grid so that the fields are accurately represented both near to and far

away from the cable. Contours of the temperature and moisture content fields are observed in close-up images to vary smoothly and continuously across the two grids. Also, the value of temperature and moisture content is extracted on the vertical line $x = 0$, passing through the cable, and plotted in Figure 7 for the four different rainfall rates in their steady-state solutions. As expected, the temperature field exhibits a local maximum at the cable and decays away from the cable. From Figure 7, we observe that the temperature peak value does not differ significantly between the four different rainfall rates examined, although the temperature falls off more rapidly with distance away from the cable for the higher rainfall rate case, as is consistent with the higher thermal conductivity caused by higher values of moisture content. The moisture content exhibits a local minimum near the cable for all four rainfall rates, which corresponds to a region in which the moisture content contour lines are locally raised upward as they pass over the cable. This effect also persists for some distance below the cable. The presence of rainfall causes the region of decreased moisture fraction (i.e., the 'dry' region) surrounding the cable to become asymmetric, with a sharper moisture gradient above the cable than below the cable.
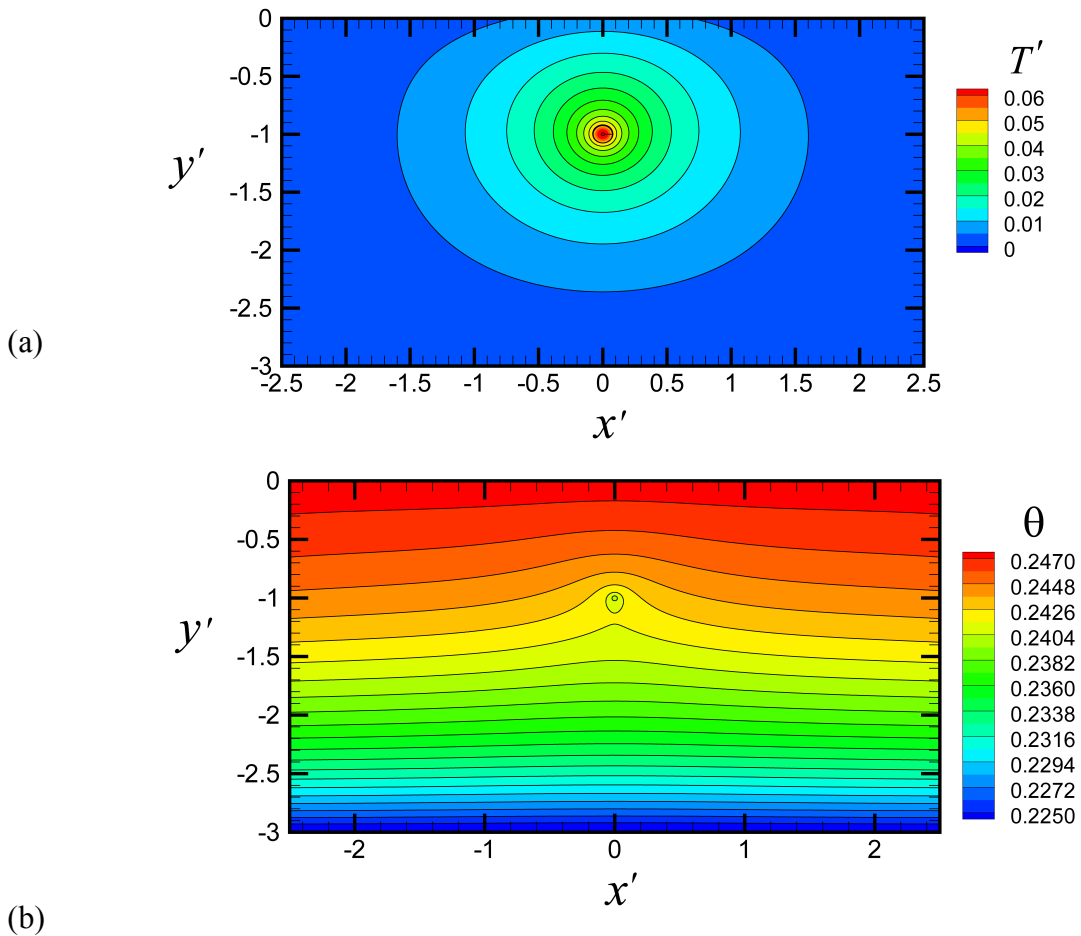

(a)

(b)

Figure 6. Steady-state (a) dimensionless temperature and (b) moisture content fields at the end of the second preliminary computation for the case with $\overline{Q}'_{rain} = 0.03$.
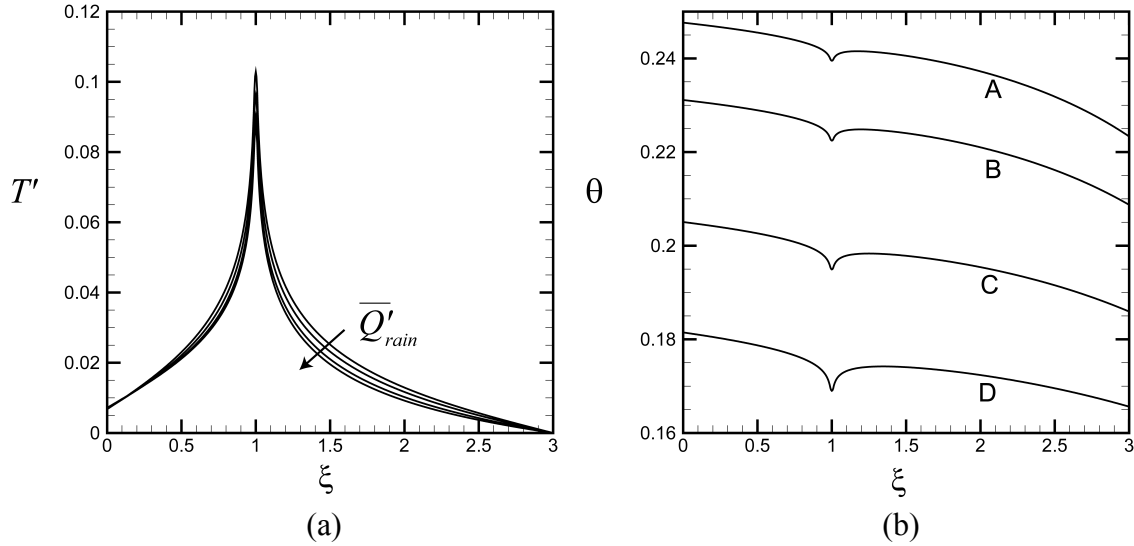
Figure 7. Variation of (a) temperature and (b) moisture content on the line $x' = 0$ as a function of dimensionless depth ξ for the same four values of $\overline{Q}'_{rain}$ shown in Figure 5.

Periodic Variation in Rainfall Intensity, Duration, and Frequency

The result of the second preliminary computation is used as an initial condition for a series of computations examining the effect of rainfall transients on cable thermal and moisture exposure. In each of these computations, the rainfall is assumed to occur periodically in time, with intensity, duration, and frequency that are consistent with the specified average rainfall rate in the preliminary computations. Each set of computations is compared with the result of the steady-state computation with constant rainfall rate. We focus specifically on two regions, one fairly moist (typical of Chicago, Illinois) and one fairly dry (typical of Los Angeles, California). The average dimensionless rainfall rates for these two regions are approximately $\overline{Q}'_{rain} \cong 0.03$ and 0.01, corresponding to 940 and 325 mm/yr, respectively. According to Sun et al. (2006), 67% of the precipitation occurs in 15 days in Los Angeles and in 30 days in Chicago, yielding a dimensionless frequency of $f' \equiv f\tau_L$ of 0.04 and 0.08, respectively. Rainfall intensity varies from about 2.5 mm/hr for a light rainfall to between 10-50 mm/hr for a heavy rainfall, with a characteristic value of 10 mm/hr for a moderate rainfall. When non-dimensionalized using $K_{\theta0} = 10^{-6}$ m/s, the characteristic value of the instantaneous dimensionless rainfall intensity, Q'_{rain}, is approximately 2.5. Dividing the total annual precipitation by the characteristic rainfall intensity (10 mm/hr) times the number of rainy days gives a typical rainfall duration of about 2.5 hours, or $D_{rain} = 2.5/24 \cong 0.1$. Using these characteristic values, a listing of computational runs was formulated as shown in Table 4. The first runs D1 and M1 are based on the characteristic conditions, runs D2-D3 and M2-M3 vary intensity and duration with fixed frequency, runs D4-D5 and M4-M5 vary duration and frequency with fixed intensity, and runs D6-D7 and M6-M7 vary intensity and frequency with fixed duration.

Results are shown in Figures 8-10 for Run D1, characteristic of a dry climate (e.g., Los Angeles). The average cable surface temperature and moisture content are plotted in Figure 8 as functions of time. The computation is performed over a time interval of 600 days, during which

24 rainfall periods occur. Even though the computation is initialized at the steady-state condition for the same value of average rainfall rate as used in the D1 computation, it is observed that the temperature and moisture fields approach a periodic limit-cycle state in which the mean temperature and moisture content on the cable surface has very different values than in the steady-state condition. The approach of the system from the steady-state solution to a limit-cycle state is shown in Figure 9, which plots the dimensionless cable surface temperature as a function of the cable surface moisture content. In this limit-cycle condition, the mean cable surface dimensionless temperature decreases by about 0.008 and the mean moisture content increases by about 0.04 compared to the steady-state solution. The oscillation amplitude of the dimensionless cable surface temperature in the limit-cycle state is $T'_{amp} \cong 0.0003$ and the amplitude of the moisture content on the cable surface is $\theta_{amp} \cong 0.0044$.

Table 4. Listing of rainfall conditions used for periodic rainfall computations in conditions typical of dry and moist climates. Rainfall is characterized by the dimensionless rainfall intensity $Q'_{rain} = Q_{rain} / K_{\theta 0}$, duration $D_{rain} = \tau_R / \tau_L$, and frequency $f' = f \tau_L$. The computational results are listed for the change in the mean values of dimensionless temperature and moisture content from the steady-state solutions, $\Delta \bar{T}'_{surf}$ and $\Delta \bar{\theta}_{surf}$, and the oscillation amplitude of the dimensionless temperature and moisture content in the periodic solution, T'_{amp} and θ_{amp}.

| Dry Climate ($\bar{Q}'_{rain} = 0.01$)							
Rainfall Characteristics				Computational Results			
Run	Intensity	Duration	Freq.	$\Delta \bar{T}'_{surf}$	T'_{amp}	$\Delta \bar{\theta}_{surf}$	θ_{amp}
D1	2.5	0.10	0.04	- 0.0081	0.00031	0.040	0.0044
D2	1.0	0.25	0.04	- 0.0076	0.00029	0.037	0.0041
D3	5.0	0.05	0.04	- 0.0097	0.00039	0.040	0.0052
D4	2.5	0.20	0.02	- 0.0085	0.00093	0.042	0.0115
D5	2.5	0.05	0.08	- 0.0074	0.00009	0.037	0.0015
D6	5.0	0.10	0.02	- 0.0104	0.00130	0.045	0.0146
D7	1.25	0.10	0.08	- 0.0067	0.00008	0.033	0.0013
Moist Climate ($\bar{Q}'_{rain} = 0.03$)							
Rainfall Characteristics				Computational Results			
Run	Intensity	Duration	Freq.	$\Delta \bar{T}'_{surf}$	T'_{amp}	$\Delta \bar{\theta}_{surf}$	θ_{amp}
M1	2.5	0.15	0.08	- 0.0094	0.00038	0.050	0.0060
M2	1.0	0.375	0.08	- 0.0088	0.00036	0.047	0.0058
M3	5.0	0.075	0.08	- 0.0082	0.00043	0.044	0.0069
M4	2.5	0.30	0.04	- 0.0101	0.00111	0.056	0.0145
M5	2.5	0.075	0.16	-0.0077	0.00012	0.042	0.0020
M6	5.0	0.15	0.04	-0.0088	0.00127	0.048	0.0170
M7	1.25	0.15	0.16	-0.0073	0.00011	0.040	0.0021
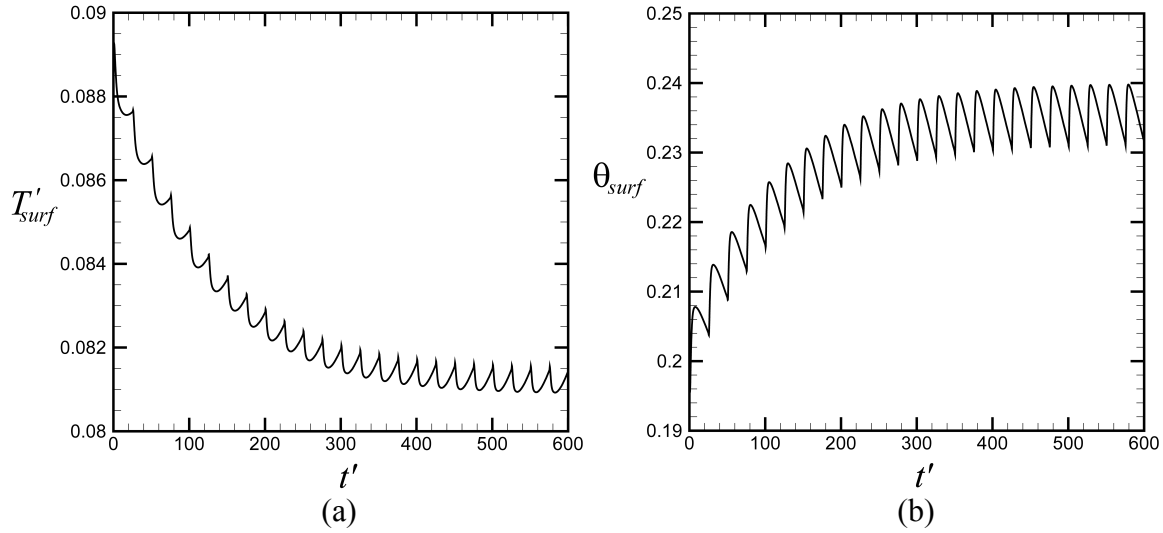
Figure 8. Oscillation of average dimensionless temperature and moisture content on the cable surface as functions of dimensionless time with constant cable heat flux, for Run D1. The oscillations observed in the plots are due to periodic rain events.
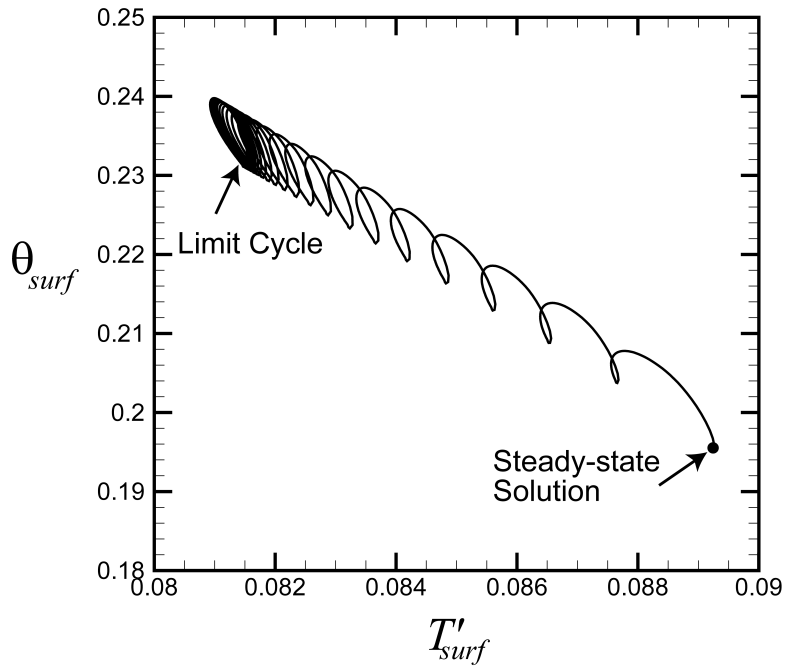

Figure 9. Plot of dimensionless cable surface temperature as a function of cable surface moisture content for Run D1, showing the approach of the system to a limit-cycle behavior at long time.
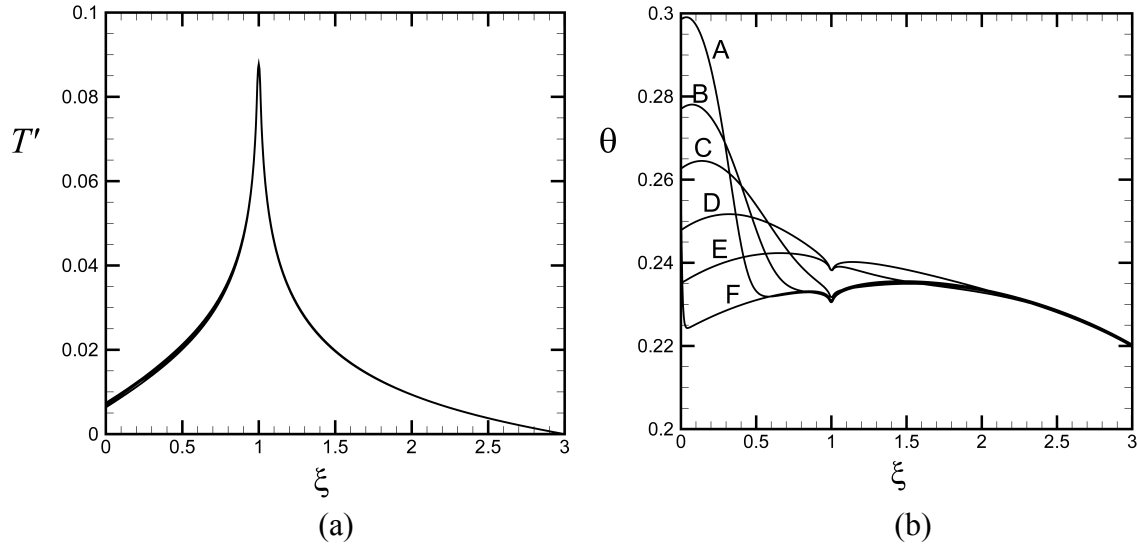
(a)   (b)

Figure 10. Variation of (a) dimensionless temperature and (b) moisture content on the line $x' = 0$ as a function of the dimensionless depth ξ for Run D1 at times (A) $t' = 575.2$, (B) 575.4, (C) 575.8, (D) 577.2, (E) 583.6, and (F) 575 and 600. The same six lines are plotted in (a), but the curves nearly overlap.

Plots showing the variation in temperature and moisture content profiles during a periodic rainfall event are given in Figure 10, for a time period $t' = [575,600]$ at which the system has achieved a periodic state. The profiles are extracted along the line $x' = 0$, which passes through the cable at depth $\xi = 1$. The largest moisture content variation occurs near the ground surface ($\xi = 0$) during the first part of the period, during and immediately after the rainfall event. The curves in this figure are plotted at times that are chosen so as to capture this moisture spike, and hence are preferentially timed for the beginning part of the rain period. Profiles are plotted at the same times in Figures 10a and 10b, but the temperature change due to moisture content variation is sufficiently small compared to the steady-state temperature values that the curves nearly lie on top of each other in Figure 10a. In Figure 10b, the rainfall is observed to cause a spike in moisture content near the ground surface $\xi = 0$. This rainfall spike rapidly propagates into the soil, and it diffuses and reduces in magnitude as it does so. Several different effects occur to influence the moisture content profiles, including downward gravitational drainage, upward pulling from the capillary force, diffusive spreading, and repulsion of moisture from the cable due to the temperature gradient around the cable. The combination of these influences causes the large fluctuation amplitude of the moisture content at the ground level ($\xi = 0$), which measures approximately 0.04, to decrease by nearly an order of magnitude at the level of the cable ($\xi = 1$). The moisture content fluctuation continues to decrease such that there is almost no observable change with time for depths $\xi < 2$. Following the rainfall event, the moisture content profile gradually returns to a curve with local maximum at approximately $\xi = 1.6$. This curve differs significantly in structure from the moisture content profile given in Figure 7b for the steady-state case.

Contour plots of the moisture content field are shown in Figure 11 for one day following a rainfall event in Run D1. The figure is plotted starting at time $t' = 575$, by which point the

system has achieved a periodic state. The initial plot (Figure 11a) is for an instance just before the rain begins. The structure of the moisture field has a region of high moisture content centered at about $\xi = 1.3$, with low moisture near both the bottom and the top of the computational domain. This high moisture band is the remnant of previous rainfalls, which are pulled downward by gravity and upward by capillary action. The region surrounding the cable is observed to be drier than surrounding regions at the same level, as evidenced by a downward deflection of the moisture contour lines. This structure differs significantly from that shown in Figure 6b for the steady-state simulation. At time $t' = 575.2$ (Figure 11b), the rain event has recently ended and a region with high moisture content is observed at the top of the figure. This region of high moisture content propagates downward with time in Figures 11c-f, eventually overtaking the dry region around the cable. Over longer time, the high-moisture region from the previous rainfall will move downward and merge into the high-moisture region located just below the cable, so that by the end of the period at $t' = 600$, the moisture field looks the same as shown in Figure 11a.
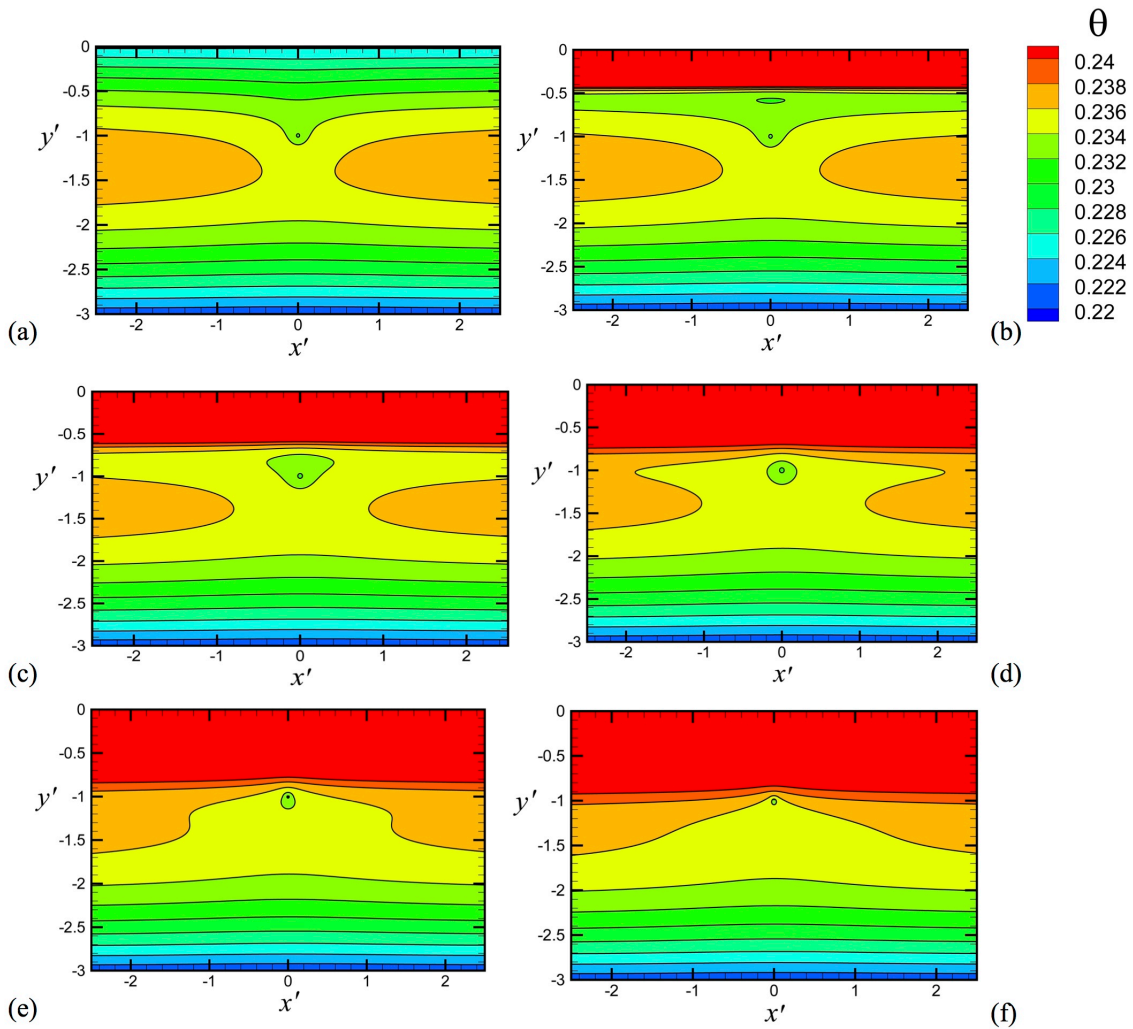

Figure 11. Contour plot of the moisture content for a time interval of one day following a rain storm, for Run D1. The plots are made at dimensionless times (a) $t' = 575$, (b) 575.2, (c) 575.4, (d) 575.6, (e) 575.8, and (f) 576.

54

Results are presented in Figures 12 and 13 for Run M1, characteristic of a moderately moisture climate (e.g, Chicago). The trends in the data are qualitatively the same as was observed under drier conditions in Figures 8 and 10. The cable surface temperature and moisture content transition from the steady-state solution to approach a limit-cycle state. The mean dimensionless cable surface temperature decreases by about 0.0094 and the mean cable surface moisture content increases by about 0.050 in this limit-cycle state compared to the values in the steady-state solution. The fluctuations in dimensionless surface temperature and moisture content during each rainfall cycle occur with amplitude $T'_{amp} \cong 0.0004$ and $\theta_{amp} \cong 0.006$, which are slightly larger than the values observed for Run D1. The temperature profile in Figure 13a is not significantly affected by the moisture variation, but the moisture profile in Figure 13b exhibits a large spike near the upper surface during and immediately after the rainfall event, with the moisture content increasing by approximately 0.1 at $\xi = 0$ during each rainfall cycle. As was the case with Run D1, the fluctuation in moisture content decays rapidly with depth, decreasing by about an order of magnitude by the level of the cable. The moisture content is observed to settle in the later part of each period to the same hump-type profile as noted in Figure 10b for Run D1, for which the moisture content is a maximum at an intermediate depth.
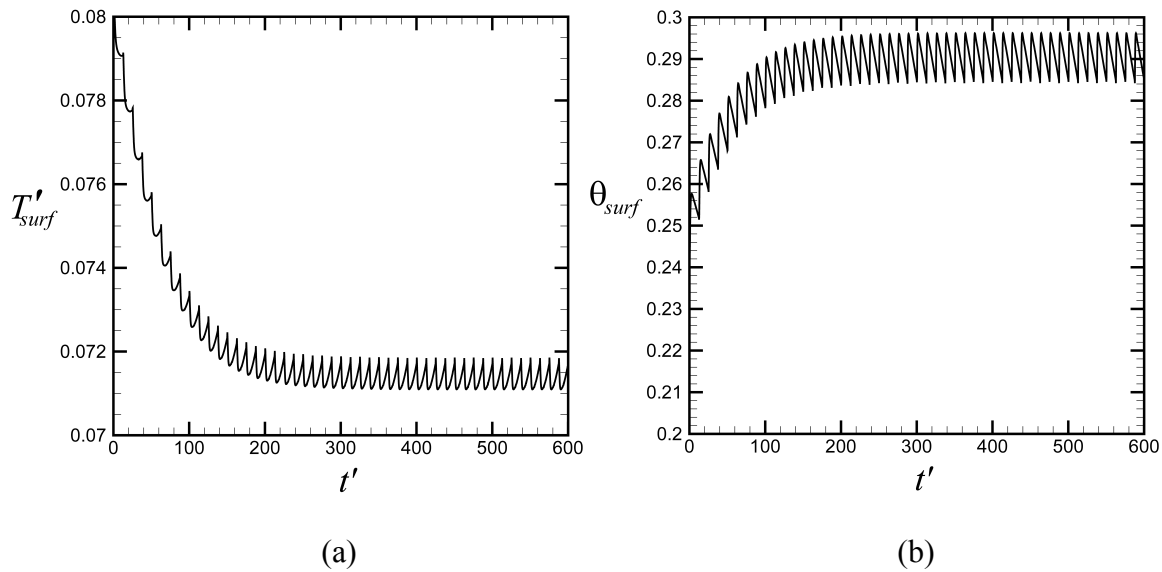

(a)

(b)

Figure 12. Oscillation of average dimensionless temperature and moisture content on the cable surface as functions of dimensionless time with constant cable heat flux, for Run M1. The oscillations observed in the plots are due to periodic rain events.
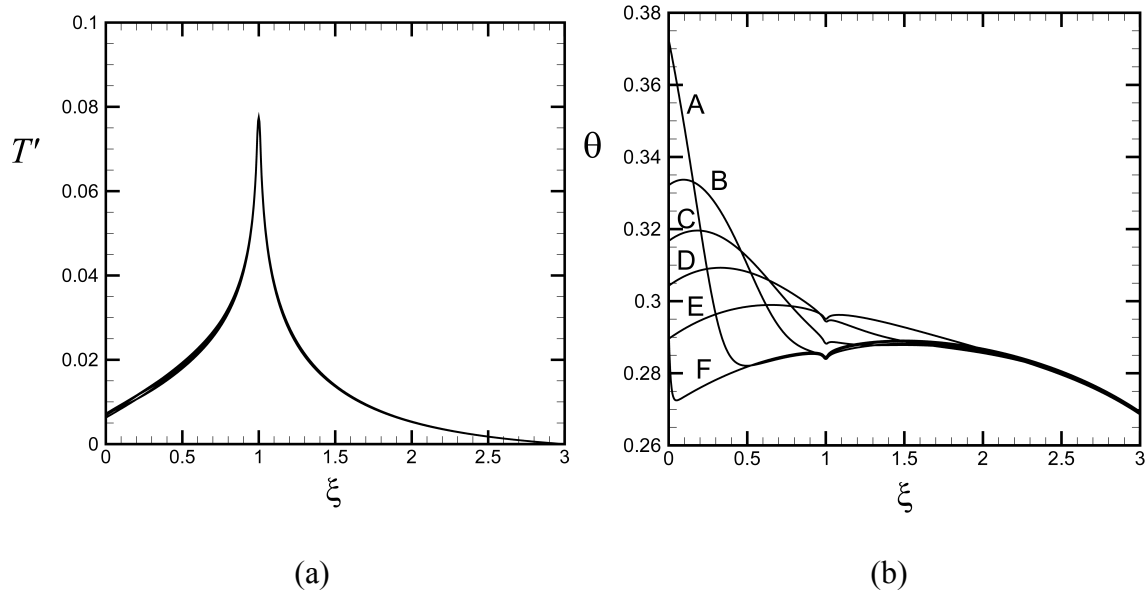
(a)　　　　　　　　　　　　　　　　　(b)

Figure 13. Variation of (a) dimensionless temperature and (b) moisture content on the line $x' = 0$ as a function of the dimensionless depth ξ for Run M1 at times (A) $t' = 587.6$, (B) 587.8, (C) 588.0, (D) 588.4, and (E) 590.0, and (F) 587.5 and 600. The same six lines are plotted in (a), but they nearly overlap.

The system response for Runs D2-D7 and M2-M7 were qualitatively similar to that described above for Runs D1 and M1. In all cases with periodic rainfall, the cable surface temperature and moisture content approach a periodic limit-cycle condition in which the mean cable surface temperature decreases and the mean cable surface moisture content increases compared to the steady-state solutions. A listing of the change in dimensionless cable surface temperature and moisture content and the amplitude of oscillation of these values in the limit-cycle state is given in Table 4 for Runs D1-D7 and M1-M7. The results in this table exhibit a strong dependence of the oscillation amplitude on the rain frequency, but a weaker dependence on rainfall intensity and duration (provided the total rainfall amount is fixed).

Figure 14 plots the computed oscillation amplitude for the dimensionless cable surface temperature and the cable moisture content as functions of dimensionless frequency f' for all of the conditions examined. The oscillation amplitude values for the moist conditions (Runs M1-M7) are substantially greater than for the dry conditions (Runs D1-D7). The amplitudes for the cable surface temperature and moisture content decrease as the rainfall frequency increases. Since the total annual rainfall amount for the dry and moist conditions is fixed, higher frequency cases correspond to conditions with frequent rainfall events containing small amounts of precipitation, whereas low frequency cases correspond to conditions with infrequent rainfall events that contain large amounts of precipitation. It is noted that the oscillation amplitude is rather small for both the cable surface temperature and the moisture content. For instance, for the example problem with burial depth $b = 1$ m and average cable heat flux $\bar{q} = 500$ W/m^2, the largest oscillation amplitude values for the cable surface temperature and moisture content in the computations conducted were $0.4°C$ and 0.017, respectively. By comparison, the temperature field obtained by Marshall et al. (2013) for the same example case oscillated due to the daily

56

power load variation with amplitude of $3.9°C$, or an order of magnitude larger than the rain-related oscillation amplitude.

Plots are shown in Figure 15 for the difference between the dimensionless cable surface temperature and the cable surface moisture content in the periodic limit-cycle condition and the initial values for the steady-state case, denoted by $\Delta T'_{mean}$ and $\Delta \theta_{mean}$. The dimensionless cable surface temperature decreases with periodic rainfall by an amount between 0.006 and 0.011, where the magnitude of the temperature change decreases with increase in the rainfall frequency. The cable surface moisture content increases with periodic rainfall by an amount ranging between 0.033 and 0.056, where the change in moisture content also decreases with increase in rainfall frequency. Again using our example problem with $b = 1\,\mathrm{m}$ and $\bar{q} = 500\ \mathrm{W/m^2}$, the change in mean cable surface temperature under the periodic rainfall condition corresponds to a decrease of $2.0 - 3.5°C$.

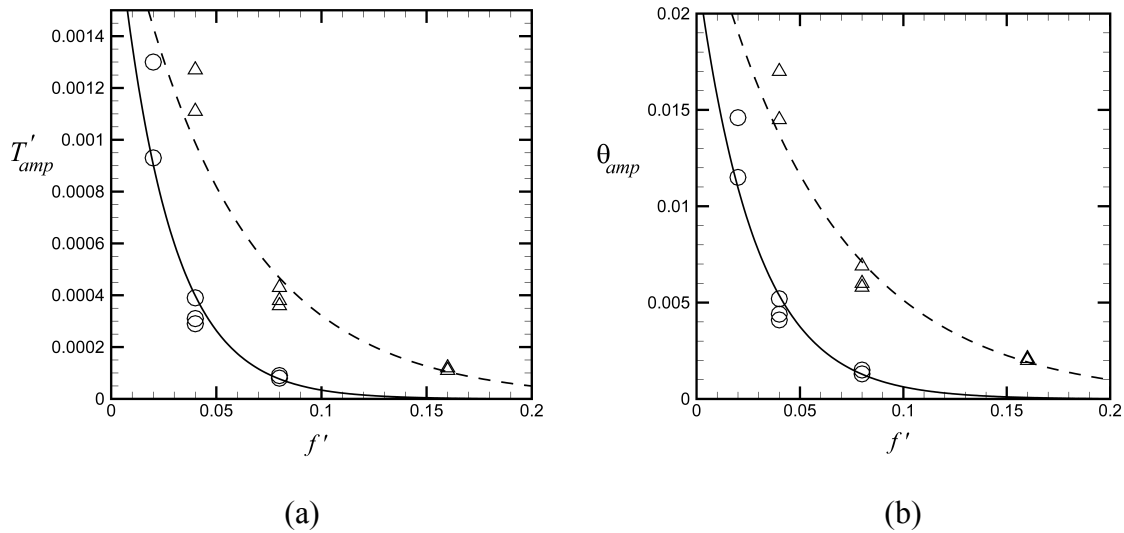(a)   (b)

Figure 14. Amplitude of average cable surface (a) dimensionless temperature and (b) moisture content fluctuations with periodic rain events as functions of dimensionless frequency. Results are for the moist condition (triangles, dashed line) and the dry condition (circles, solid line) listed in Table 4. The curves are exponential fits to the data.

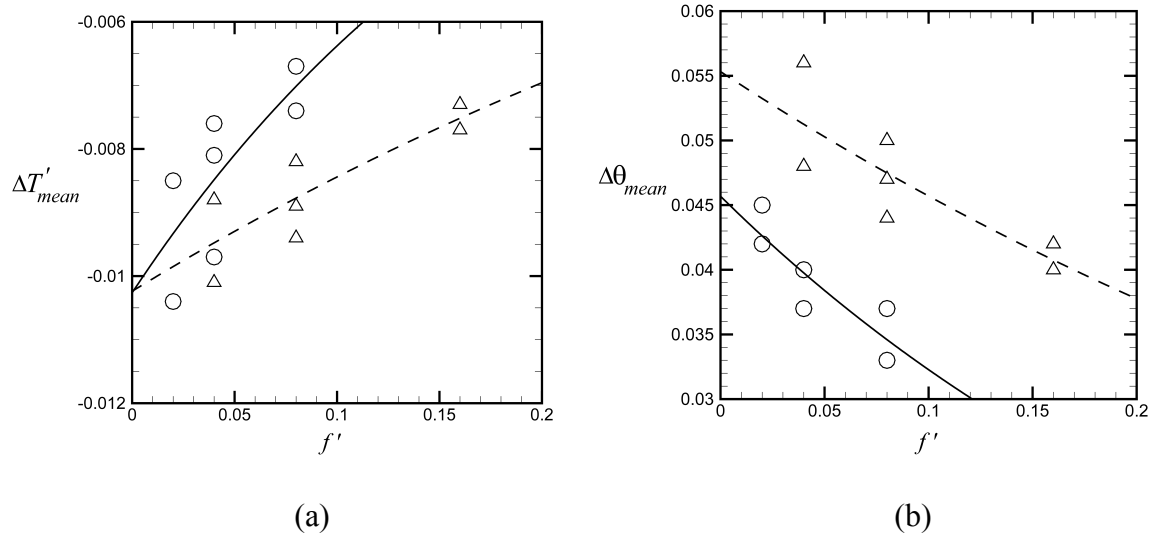(a)   (b)

Figure 15. Change in mean values of the average cable surface (a) dimensionless temperature and (b) moisture content with periodic rain events as functions of dimensionless frequency. Results are for the moist condition (triangles, dashed line) and the dry condition (circles, solid line) listed in Table 4. The curves are exponential fits to the data.

4. Conclusions

A study of the effect of periodic rainfall events on the surface temperature and moisture exposure of a buried electric cable was conducted using numerical simulations. Cases with different rainfall intensity, duration, and frequency were compared to a steady-state case with the same annual precipitation amount. Computations were conduced for two values of the annual precipitation, one typical of a relatively moist climate and one typical of a dry climate. In the steady-state condition, the computations indicate formation of a relatively dry region surrounding the cable in which the moisture content decreases by about 2-5% compared to the value that it would have had without the cable present. Under periodic rainfall conditions, the cable surface temperature and moisture content transition to a limit-cycle behavior with values that oscillate periodically in time with the rainfall frequency. Of particular interest is the observation that the mean values of the cable surface temperature and moisture content in this limit-cycle condition are significantly different from the steady-state values, with the mean cable surface temperature decreasing and the moisture content increasing in value under the limit-cycle condition relative to the steady-state condition. Both the oscillation amplitudes and the change in mean values relative to the steady-state condition are observed to depend primarily on the rainfall frequency and on the annual precipitation amount, such that the absolute values of these quantities decrease as the rainfall frequency or the annual precipitation amount increase. While the computed values of the oscillation amplitude of the cable surface temperature are rather small, measuring $0.4°C$ or less in the current computations, the change in the mean cable surface temperature between the steady-state and limit-cycle conditions is found to be large, measuring as high as $3.5°C$ in the current computations. Similarly, the largest computed value of the oscillation amplitude of the moisture content (0.017) is small compared to the largest computed value of the change in mean cable surface moisture content between the limit-cycle and steady-state conditions (0.056).

The results of the current study have shown that periodic rainfall conditions result in fundamentally different moisture and temperature fields around an underground cable compared

to what would be observed under rainfall steady-state conditions. Not only do the moisture content and temperature values oscillate periodically in time when exposed to periodic rainfall events, but the time-averaged values of the moisture content and temperature also change significantly in this periodic case compared to their steady-state values. The change in the mean values causes decreased values of the cable surface temperature, but increased values of the cable surface moisture content. As a consequence, steady-state computations over-estimate the temperature-related degradation of the cable insulation but under-estimate the moisture-related insulation degradation.

References

G.J. Anders, *Rating of Electric Power Cables. Ampacity Computations for Transmission, Distribution, and Industrial Applications*, IEEE Press, New York, 1997.

G. J. Anders, M. A. El-Kady, Transient ratings of buried power cables. Part 1. Historical perspective and mathematical model, *IEEE Trans Power Delivery* **7**(4) (1992) 1724-1734.

G.J. Anders, H. S. Radhakrishna, Computation of temperature field and moisture content in the vicinity of current-carrying underground power cables, *IEEE Trans* **135C** (1988) 51-61.

W.Z. Black, S. I. Park, Emergency ampacities of direct buried three phase underground cable systems, *IEEE Trans Power Apparatus Systems* **102**(7) (1983) 2124-2132.

K. Clement-Nyns, E. Haesen, J. Driesen, The impact of charging plug-in hybrid electric vehicles on a residential distribution grid, *IEEE Trans. Power Systems* **25**(1) (2010) 371-380.

L. P. Fernández, T. G. San Román, R. Cossent, C. M. Domingo, P. Frías, Assessment of the impact of plug-in electric vehicles on distribution networks, *IEEE Trans. Power Systems* **26**(1) (2011) 206-213.

N. Flatabo, Transient heat conduction problems in power cables solved by finite element method, *IEEE Trans Power Apparatus Systems* **92**(1) (1973) 56-63.

D. S. Freitas, A. T. Prata, A. J. de Lima, Thermal performance of underground power cables with constant and cyclic currents in presence of moisture migration in the surrounding soil, *IEEE Trans. Power Delivery* **11**(3) (1996) 1159-1170.

C. Garrido, A. F. Otero, J. Cidrás, Theoretical model to calculate steady state and transient ampacity and temperature in buried cables, *IEEE Trans Power Del* **18**(3) (2003) 667-678.

G. Gela, J. J. Dai, Calculation of thermal fields of underground cables using the boundary element method, *IEEE Trans Power Delivery* **3**(4) (1988) 1341-1347.

M.A. Hanna, A.Y. Chikhani, M. M. A. Salama, Thermal analysis of power cables in multi-layered soil. Part 1. Theoretical model, *IEEE Trans Power Delivery* **8**(3) (1993) 761-771.

I.N. Hamdhan, B.G. Clarke, Determination of thermal conductivity of coarse and fine sand soils. Proceedings World Geothermal Congress, Bali, Indonesia, 25-29 April (2010).

P. Hyvönen, Prediction of insulation degradation of distribution power cables based on chemical analysis and electrical measurements, Ph.D. dissertation, Helsinki University of Technology, 2008.

M.A. Kellow, A numerical procedure for the calculation of the temperature rise and ampacity of underground cables, *IEEE Trans Power Apparatus Sys* **100**(7) (1981) 3322-3330.

N. Kovač, I. Sarajčev, D. Poljak, Nonlinear-coupled electric-thermal modeling of underground cable systems, *IEEE Trans Power Delivery* **21**(1) (2006) 4-14.

M. Liang, An assessment of conductor temperature rises of cables caused by a sudden application of short pulse in a daily cycle load, *IEEE Trans Power Del* **14**(2) (1999) 307-313.

J.S. Marshall, P.D. Hines, J.D. Zhang, F. Minervini, S. Rinjitham, Modeling the impact of electric vehicle charging on heat transfer around underground cables, *Electric Power Systems Research* **97** (2013) 76-83.

G. Mazzanti, Analysis of the combined effects of load cycling, thermal transients and electrothermal stress of life expectancy of high-voltage AC cables, *IEEE Trans. Power Delivery* **22**(4) (2007) 2000-2009.

G. Mazzanti, The combination of electro-thermal stress, load cycling and thermal transients and its effects on the life of high voltage ac cables, *IEEE Trans Dielectrics Electrical Insulation* **16**(4) (2009) 1168-1179.

G. C. Montanari, G. Mazzanti, L. Simoni, Progress in electrothermal life modeling of electrical insulation over the last decades, *IEEE Trans Dielectrics Electrical Insulation* **9**(5) (2002) 730-745.

R.E.S. Moya, A.T. Prata, J.A.B. Cunha Neto, Experimental analysis of unsteady heat and moisture transfer around a heated cylinder buried into a porous medium. *International Journal of Heat and Mass Transfer* **42**, 2187-2198 (1999).

J. Nahman, M. Tanaskovic, Calculation of the ampacity of medium voltage self-supporting cable bunch, *Electric Power Systems Research* **93** (2012) 106-112.

J. H. Neher, M. H. McGrath, The calculation of the temperature rise and load capability of cable systems, *AIEE Trans*, Part 3, **752-763** (1957) 752-763.

J. H. Neher, The transient temperature rise of buried cable systems, *IEEE Trans. Power Apparatus Systems* **83**(2) (1964) 102-114.

J.R. Philip, D.A. de Vries, Moisture movement in porous materials under temperature gradients. *Transactions of the American Geophysical Union* **38**, 222-232 (1957).

P. Rezaei, J. Frolik, P. Hines. Packetized plug-in electric vehicle charge management. *IEEE Transactions on Smart Grid* (in press, 2014).

Y. Sun, S. Solomon, A. Dai, and R.W. Portman, How Often Does It Rain? *Journal of Climate* **19** (2006) 916-934.

E. Tarasiewicz, E. Kuffel, and S. Grybowsji, Calculation of temperature distributions within cable trench backfill and the surrounding soil, *IEEE Trans. Power Apparatus Systems* **104**(8) (1985) 1973-1978.

L. R. Vollaro, J. Fontana, A. Vallati, Thermal analysis of underground electric power cables buried in non-homogeneous soils, *Applied Thermal Engineering* **31** (2011) 772-778.

R. Webster, Can the electricity distribution network cope with an influx of electric vehicles?, *J. Power Sources* **80**(1–2) (1999) 217–225.

Chapter 5
Packetized Plug-in Electric Vehicle Charge Management[1]

Pooya Rezaei, Jeff Frolik, and Paul Hines

Abstract

Plug-in electric vehicle (PEV) charging could cause significant strain on residential distribution systems, unless technologies and incentives are created to mitigate charging during times of peak residential consumption. This paper describes and evaluates a decentralized and 'packetized' approach to PEV charge management, in which PEV charging is requested and approved for time-limited periods. This method, which is adapted from approaches for bandwidth sharing in communication networks, simultaneously ensures that constraints in the distribution network are satisfied, that communication bandwidth requirements are relatively small, and that each vehicle has fair access to the available power capacity. This paper compares the performance of the packetized approach to an optimization method and a first-come, first-served (FCFS) charging scheme in a test case with a constrained 500 kVA distribution feeder and time-of-use residential electricity pricing. The results show substantial advantages for the packetized approach. The algorithm provides all vehicles with equal access to constrained resources and attains near optimal travel cost performance, with low complexity and communication requirements. The proposed method does not require that vehicles report or record driving patterns, and thus provides benefits over optimization approaches by preserving privacy and reducing computation and bandwidth requirements.

1. Introduction

Plug-in Electric vehicles (PEVs) have the potential to facilitate a transportation future that is less dependent on liquid fossil fuels. However, as PEV market penetration increases, vehicle charging could strain aging power delivery infrastructure. A number of recent papers have shown that increases in PEV charging could have detrimental impacts on medium and low voltage distribution infrastructure (e.g., [1],[2]), particularly where PEV adoption is highly clustered [3]. With mass-produced PEVs coming to market and a range of charging standards (AC Levels 1-3) established [4], it is increasingly important to understand and mitigate negative impacts that PEV charging might have on distribution system components, such as underground cables and transformers.

Implementing effective charge management (CM, also known as smart charging) methods is one step to facilitate the smooth integration of PEVs. Several previous studies (e.g., [1],[2]) show that with effective CM schemes it is possible to support large numbers of electric vehicles even with constrained electric power infrastructure. In many cases it is also possible for PEVs to not only avoid negative impacts on the power grid, but also to provide grid services, through Vehicle-to-Grid (V2G) technology (e.g., [5],[6]).

The CM and V2G control schemes that have been proposed in the literature, or in industry, generally fall into one or both of the following categories:

---

[1] This chapter is based on work published as follows: Pooya Rezaei, Jeff Frolik, and Paul Hines, "Packetized Plug-in Electric Vehicle Charge Management." *IEEE Transactions on Smart Grid*, Vol. 5, No. 2, pp. 642-650, 2014.

1. Centralized optimization or control methods in which each vehicle submits information to a central authority, which in turn solves an optimization problem that produces a charging schedule for each vehicle [7]-[12].

2. Decentralized methods, in which either utilities set a pricing scheme (e.g., a two-period time-of-use price) and vehicles self-schedule based on those prices [13]-[15], or market-based scheme that generate prices from bid or historical information, to which vehicle charge management devices respond [5],[16]-[20].

These two approaches have a variety of advantages and disadvantages.

Centralized schemes have the advantage that they produce optimal outcomes by minimizing costs and avoiding constraint violations in the distribution system. However, optimization/control methods require that vehicle owners provide information (e.g., willingness to pay or anticipated departure times) to a central authority and give up at least some autonomy over the charging of their PEV. While the load-serving entity would likely compensate the vehicle owner for this loss of control with a reduced rate for electric energy, reduced autonomy could be an impediment to the adoption of CM schemes. In addition, vehicle owners are unlikely to know in advance their exact travel schedule, which complicates the problem.

Dynamic pricing schemes, such as reduced rates for nighttime charging, do not have these disadvantages; drivers are free to choose how to respond to change in prices. However, because not all vehicle owners will be price responsive, price-based schemes do not guarantee that vehicle charging will not produce overloads. In fact, under some conditions, time-differentiated pricing could produce new load peaks that increase, rather than decrease, aging in the distribution infrastructure [2]. The method in [21] seeks to combine the benefits of centralized and dynamic pricing schemes, but has the disadvantage that customers need to declare their willingness to pay for electricity in order to set the parameters for the bidding system. One major impediment for purely price-based schemes is the concern expressed by many utilities that true real-time pricing schemes would not be acceptable to electricity customers [22].

The stochastic nature of charging behavior is particularly important to highlight. PEV arrival and departure times vary substantially among different owners, days, and times-of-day. While aggregate load for a region can be predicted with some accuracy, distribution feeder loads are less predictable, due to the smaller number of customers over which to average. Distribution system load variability and uncertainty will grow even further with an increase in distributed renewable generation. Vehicle CM schemes that do not adapt well to this uncertainty are unlikely to be successful.

The combination of random supply (available capacity on a feeder, for example) and random demand for PEV charging is analogous to the problem of sharing a constrained channel in multiple access communication systems. This paper proposes an approach where PEV charging is completed over multiple short intervals using 'charge-packets,' which are analogous to discrete 'data packets' that revolutionized communications. Our approach leverages a probabilistic automaton, the design of which originated in the decentralized control of node activity in wireless sensor networks [24]. While the packetized approach could be applied in a variety of power system contexts, this paper focuses on the problem of ensuring that PEV charging does not result in overloads in residential distribution components (e.g., transformers or underground cables). Simulation results (Sec. 5) show that the inherent randomness in vehicle charging enables constrained resources to be fairly and anonymously shared.

Our approach builds on previous work by the authors and others applying communication algorithms to the problem of PEV charging. We extend our prior work [29]-[31] by simulating realistic travel demand behavior, and by comparing the packetized approach with other approaches to CM. Another communication-inspired algorithm is proposed in [25], which uses a more complicated communication algorithm, in order to treat PEV charging as a continuously controllable variable. Unlike many proposed smart charging methods (e.g., [1],[21]), the charge-packet method does not require drivers to estimate their future departure times.

2.   The Communication Channel Analogy

2.1   Characteristics of Modern Communications

Modern communication systems are characterized not only by information that is digital in format but also by the way that data are sent in multiple discrete packets, each of finite duration. Packet communications can occur over dedicated or shared channels, the latter type we view to have analogous issues to PEVs sharing the power distribution system. In the communications field, techniques that manage access to shared channels (or bandwidth) are collectively known as media access control (MAC) protocols and have as an objective the efficient use of the bandwidth resource (measured by channel throughput) for the load placed on the system [26]. This objective is analogous to matching the demand for power to the available capacity of a feeder, to ensure that high loads do not damage the infrastructure, or trigger instabilities (e.g., voltage collapse). A second objective for MAC protocols is ensuring that latency does not exceed the user's requirements; we view the latency objective to be analogous to PEVs receiving the requisite charge in the requisite time, which is a primary concern to PEV owners. The packetization of data allows both of these conflicting objectives to be addressed simultaneously in communication systems.

2.2   Packetization of PEV Charge

Why is PEV home charging a candidate for packetized delivery? Firstly, a 5-8kW AC Level 2 PEV charger is likely to be the highest power load in a home; if many chargers in a neighborhood were to run simultaneously, substantial infrastructure degradation could result, particularly in older distribution systems. In addition, most PEV owners with Level 2 chargers will not need to charge their vehicles immediately upon vehicle arrival at home. Given fast charge rates, there is likely to be more than sufficient time overnight to bring a PEV's battery to the desired state of charge (SOC) for the next day's driving. In short, it is typically not necessary that PEV charging be continuous from start to finish.

Packetized charging breaks the required charge time into many small intervals of charging (i.e., 'charge-packets'). For example, 4 hours of Level 2 charging could be accomplished with 48, 5-minute charge-packets. A PEV (or its charging station) would request the authorization to charge for the packet's duration. A charge-management coordinator device at the distribution substation would assess local conditions and determine whether additional load on the system can be accommodated. If allowed, the PEV will charge for the duration of the packet and then submit new requests for subsequent packets until the battery is fully charged. If charging cannot be accommodated, the PEV resubmits a request at a later time.

The accommodation or denial of charging is analogous to the successful transmission of a data packet or a packet collision, respectively, in random access communication systems in which

users compete for available bandwidth. Benchmark MAC methods developed for random access channels include Aloha, Slotted-Aloha and Carrier Sense Multiple Access (CSMA) [26], each of which requires very little (if any) overhead communications between the source and loads in the system. The MAC techniques provide a predictable throughput (i.e., utilization of bandwidth) for a given stochastic load by the network as a whole. However, individual user load is not managed by MAC protocols and thus a different type of control is needed if we wish to leverage packetization for the PEV charge management problem.

3. A Probabilistic Automaton for PEV Charge Management

3.1 Automaton Design

The problem of managing, in a distributed manner, the individual activity rates (i.e., load) for entities in a large group is similar to the control of active nodes in a wireless sensor network and to the PEV CM problem. For the sensor-network problem, N-state probabilistic automatons have been proposed that are both simple to implement on computationally constrained hardware and require minimal communications for control [24, 27, 28]. Our earlier work, [24] and [28], illustrated the ability of this
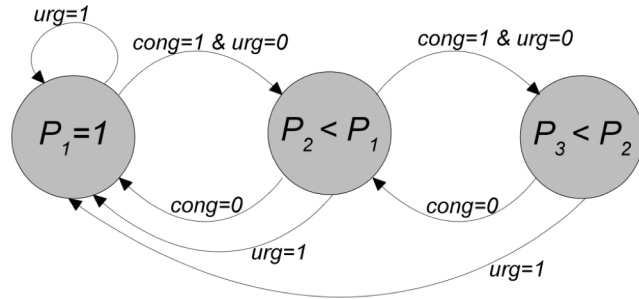

Fig. 1. A three-state ($N=3$) automaton where P_2 corresponds to a lower probability of PEV charge request than P_1, and P_3 to a lower probability than P_2. In case of charge urgency ($urg=1$) the state machine will stay at P_1, but if there is no charge urgency by driver's call ($urg=0$), and the power transformer was congested ($cong=1$), i.e. a charge request was denied to avoid transformer overload, the PEV state machine will go to a state with lower probability. If charge urgency was set by the driver ($urg=1$) the state machine will go to P_1 with the highest probability.

approach to control participation for a large range of nodes and activities levels in a manner that ensured equity of participation among nodes. For PEV charging, we leverage this automaton design, of which a simple version ($N=3$) is presented in Fig. 1.

As shown in the state diagram (Fig. 1), if the node (sensor or PEV) is in its middle state, it will transmit during a particular epoch (time period) with probability P_2. In the PEV application, this "transmission" corresponds to the PEV requesting a packet of charge for a fixed length of time (or epoch). If the request can be supported by the infrastructure, the vehicle is allowed to charge for one epoch. In the communications context this would mean being "rewarded" by the channel, through successful transmission of the data. With a successful request, the state machine moves to the next higher probability state (P_1) and transmits during the next epoch with probability $P_1 > P_2$. If the request was not successful, the PEV would not charge for the epoch, would move to the next lower probability state, and would request at the next epoch with probability $P_3 < P_2$. Prior work demonstrated that this automaton approach could adapt to scenarios where the distribution capacity varies over time [29].

For fair and consistent treatment across all PEVs, each user's automaton would have the same design. However, in order to ensure that drivers who need to charge their vehicles more quickly are able to do so, the design can be adjusted to give such vehicles a higher priority. In our design, each charger would have an "urgent" mode [30], which, when selected by the user, increases the probability of charge requests, and also the price of electricity. As implemented in this paper (see Fig. 1) 'urgent' vehicles request charge at each epoch with $P_1=1$ [31].

3.2   Possible Implementation Approaches

Key advantages of the proposed packet-based CM approach are that (1) the scheme can be used to manage constraints anywhere in a distribution system, (2) the communication requirements are minimal, and (3) customer privacy is maintained. Here we discuss these advantages by describing possible ways to implement the required communications (broadcast vs. point-to-point communications) and various power system constraints that the algorithm could be used to address.

The packetized method can be implemented to mitigate overloads at a variety of locations within a distribution system, such as avoiding thermal overloads in underground cables, low-voltage service transformers, or medium voltage distribution transformers, or avoiding under-voltage conditions in the network, or (using a hierarchical design) any combination of these constraints. In each case, a charger automaton would communicate with an aggregator responsible for managing a particular constraint. For the case of medium voltage constraints, the aggregator could be located at the distribution substation. For the case of service-transformer constraints, the aggregator would likely be located at the transformer. The only data that would flow from the PEV charger to the aggregator would be charge-packet requests. The aggregator would respond to requests only based on available capacity. In each of these cases, communications could occur over Advanced Metering Infrastructure systems, which typically have very low communications bandwidth and high latencies, emphasizing the importance of a scheme that makes limited use of this bandwidth.

It is possible to implement communications for the packetized method with either one-way (simplex) or two-way (duplex) data flows. In the duplex case, the aggregator would respond to each request individually with either an approval or denial. In the simplex case, the aggregator would broadcast the state of the resource (either overloaded, or not-overloaded) and chargers would make their request locally by merely randomly "listening" to the broadcast signal. The latter version has advantages in terms of privacy, as the transformer is blind to who is receiving permission to charge.

These approaches represent conceptual extremes on how the packetized CM technique could be implemented. Note that combinations of these schemes could be employed simultaneously. For example, a PEV charger might send requests to an aggregator at the substation only if a service transformer's broadcast signal indicated that there was local capacity available. Because vehicle chargers using the packetized method only charge when there is sufficient capacity in the system, our approach ensures that PEV loads will not cause overloads in components that are monitored by the system.

3.3   Illustrative results for a service transformer

To illustrate the operation of our approach, this section demonstrates how the charge-packet method would operate for the case of a constrained low-voltage service transformer. In this example scenario, a transformer has a peak load limit of 30kVA and serves 20 homes and 10 PEVs. The baseline residential load patterns were the same as used in [2], scaled to an average of 1 kVA per home, with a 0.9 power factor. The PEV travel patterns were randomly sampled from travel survey data [32] for New England, as described in [2]. Each vehicle was assumed to charge using AC Level 2 charging rates (7 kW at 1.0 power factor). The electric vehicle characteristics roughly reflect those of the GM Volt, with an efficiency of 4.46 km/kWh in electric mode and 15.7 km/L in gasoline mode, and a 13 kWh usable battery capacity. While all

of the simulation results in this paper are for series Plug-in Hybrid Electric Vehicles (PHEV), the packetized method could just as easily be applied to pure battery electric vehicles (BEV). However, for the BEV case, the travel survey data are likely to be a less accurate representation of travel behavior, since BEV drivers may adjust their travel patterns given the reduced range of the vehicle. For this reason we simulated PHEVs rather than BEVs.

In this paper, we assumed that drivers can decide to choose between urgent or non-urgent charging modes and that, once chosen, this choice is constant during the day (the simulation duration). In the urgent mode, the vehicle requests charge regardless of the price of electricity, and its automaton stays at P_1 (the highest probability). In the non-urgent mode, the vehicle requests charge only during off-peak hours, and its automaton can go to lower states in case of charge denial.

For our first illustrative example, we used the following assumptions. First, all PEVs operate in the non-urgent charging mode, and thus do not request charge during peak hours (8 a.m. to 8 p.m). Second, each PEV charger was managed with a three-state (N=3) automaton as illustrated in Fig. 1, with request probabilities of P_1=1, P_2=0.5 and P_3=0.25. Finally, time epochs were set to 15 minutes.
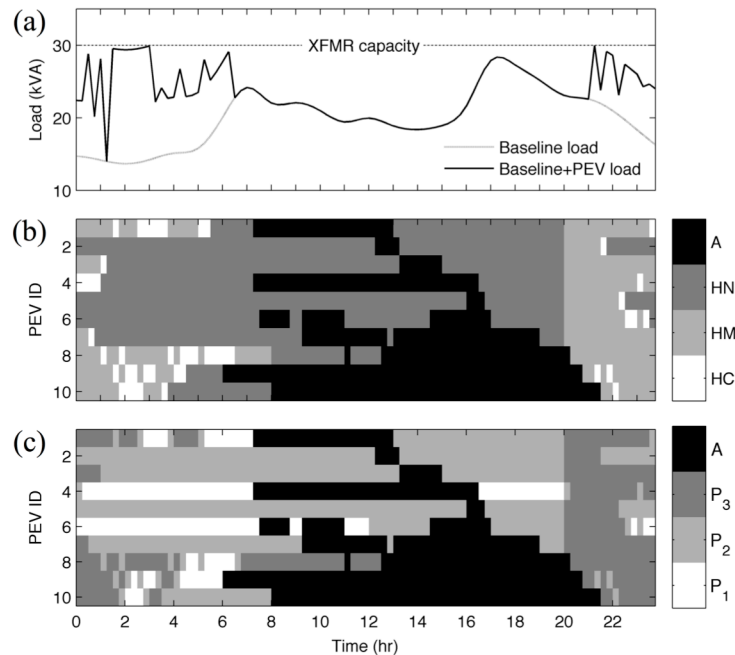

Fig. 2. Illustration of the charge-packet method for a service transformer with a 30kVA limit. (a) Load curve, showing the residential and the aggregate transformer load. (b) PEV status with gray shades indicating: A: PEV is away, HN: PEV is at home but not requesting for charge (either the battery is full, or it is during peak hours), HM: PEV requested a charge packet, but was denied to avoid transformer overload (charge mitigation), HC: PEV is at home and charging. (c) PEV automaton state number with the gray shades showing each automaton's state at the end of the epoch.

Fig. 2 shows the simulation result for this example. The top panel shows the transformer load with and without PEV charging. While the load approaches the 30kVA limit, the constraint is satisfied over the entire period. The middle panel shows the status of each PEV over the day,

with white bands showing the randomly scattered 15-minute periods during which vehicles were charging (note that vehicles are sorted by the time at which they arrive at home for evening charging). The lower panel shows the changing automaton states over the day, illustrating that during off-peak hours, the automatons are more likely to sit in the lower state (P_3). This is notable since these states are determined locally based only on the success of the vehicle's most recent charge request.

4. Comparison Charge Management Schemes

The results in Fig. 2 illustrate how the decentralized charge-packet CM approach can be used to keep transformer loads below a desired limit. This section describes two comparison schemes that were used to evaluate and illustrate the relative merits of the packetized approach. As stated in Sec. 3, the results that follow assume that all vehicles are series PHEVs, which use gasoline after their batteries are fully depleted.

4.1 First-come, first-served charge management

A simpler decentralized approach to the CM problem would be a first-come, first-served (FCFS) method in which vehicles are allowed to charge as soon as they arrive home and can continue to charge, so long as there is sufficient capacity available. As we will show, this approach puts vehicles arriving home at a later time at a disadvantage, should there be a capacity constraint in the system. Like the charge-packet method, this approach is largely decentralized, is low in computational complexity, ensures that charging will not exceed the feeder capacity, and can be implemented with equivalent limited communications. In our FCFS implementation, PHEVs are allowed during both peak and off-peak hours. Once charging begins, it continues until one of the following occurs: the battery is fully charged, the PHEV leaves home, or the network (transformer or feeder) becomes overloaded by an increase in non-PHEV load. In the latter case, the system randomly chooses a vehicle to stop charging.
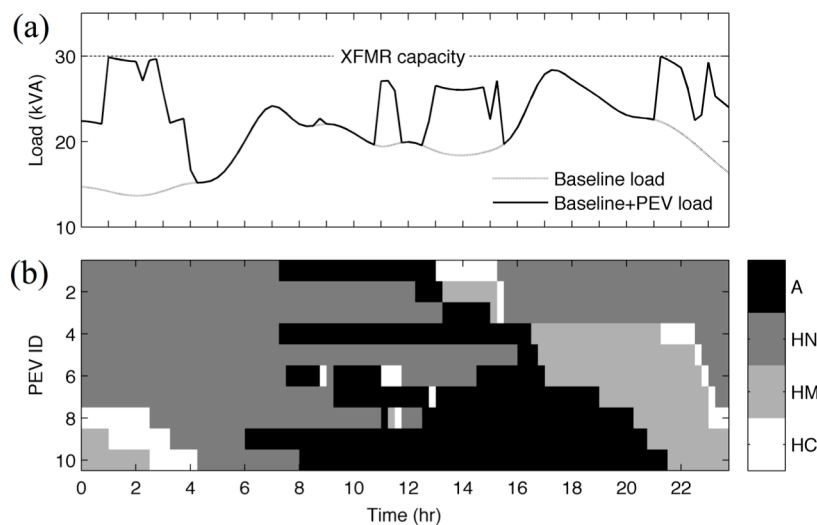

Fig. 3. Sample illustration of the FCFS charging method. (a) Load curve (b) PEV status using the same gray-scale codes as in Fig. 2.

Fig. 3 shows results from the FCFS approach for the same 10-vehicle scenario as in Fig. 2. In this scenario, vehicles have more continuous charging patterns (as seen by the continuity in the white bands in the lower panel). Because time-of-use prices are not considered by PHEVs in this method, they charge regardless of the time of day, as long as the transformer is not overloaded. In this case, vehicles that arrive later in the day or are initially denied charge are at a disadvantage because they cannot start charging until there is sufficient capacity to support additional PHEV charging. As a result PHEVs 9 and 10 do not start charging until the early hours of the morning (Fig. 3(b)). In contrast, the randomized nature of the packetized approach solves this fairness problem by requiring vehicles to request new packets at each epoch, providing vehicles with equal access to the resource, regardless of arrival times. In the packetized simulation (Fig. 2), vehicles 9 and 10 charge during several intervals during the night, with the first packets shortly after vehicle arrival. In Fig. 3, PHEVs 9 and 10 do not get any charge until after 1 and 2 am respectively. The extent to which vehicles get equal access to charging is quantified and compared in Sec. 5 (see Fig. 7).
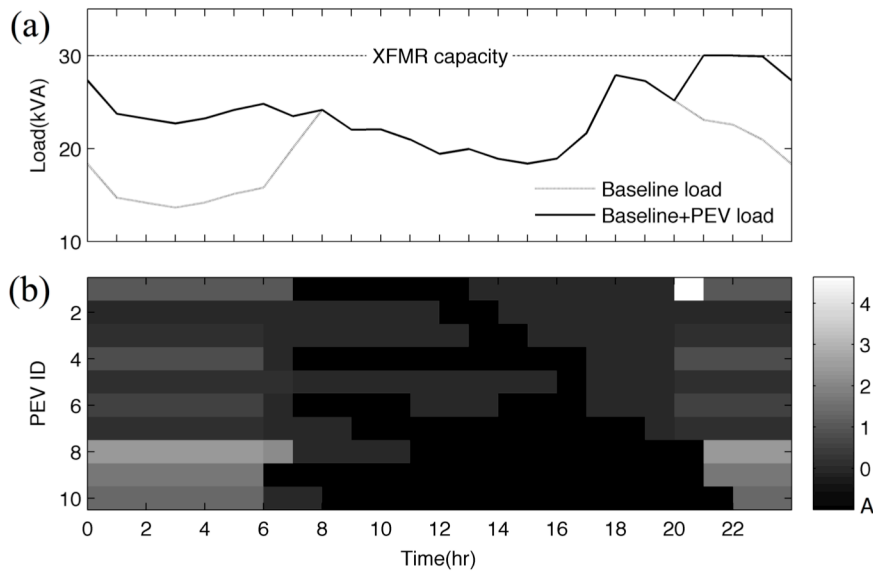

Fig. 4. Illustrative results for optimal charge management. (a) Load curve. (b) PEV status with gray levels showing the amount of energy given to each PEV at each hour. In the grey-level bar, "A" shows the time when the PHEV is away. When at home, hourly charge quantities vary between 0 and 4.64 kWh, which is the maximum quantity delivered in this example.

The FCFS charging scheme is a useful comparison scheme for two reasons. First, it illustrates how much charging costs increase, if PHEVs are not responsive to time-of-use prices, having the same travel pattern as in packetized charging method. Second, the FCFS method illustrates the potential of the packetized approach to provide equal access to constrained resources for all PHEVs.

4.2   Optimal Charge Management

The second comparison method is a centralized optimal CM scheme, which we use to identify the minimum cost charge scenario for each travel pattern and compare that cost to that of the packetized case under a two-rate, time-of-use residential tariff. A critical distinction for the optimal case is that the model assumes that PHEV charge rates can be continuously controlled

between zero and the full charge rate. Also, and significantly, the travel behavior for each user must be known in advance for the optimization scheme. As in the other cases, all vehicles were assumed to be serial plug-in hybrid electric vehicles, with gasoline used only after the usable battery capacity was expended.

The optimization problem formulation is a mixed integer linear programming model based on the approach in [12]. Only the objective function and our modifications to the model are described here; the reader is referred [12] for further details.

The objective in the optimization method is to minimize the retail costs to vehicle owners associated with traveling the miles described in the travel survey data. Because the vehicles are PHEVs, and the homes are charged for electricity using time-of-using pricing, there are three fuels that can be used for charging: on peak electricity, off peak electricity, or gasoline. The resulting objective (cost) function is given in (1):

$$C_t = \sum_{t=1}^{T} \sum_{v=1}^{N} \left[\frac{\pi_e(t) \cdot P(v,t) \cdot h}{\eta_e} + \frac{\pi_g \cdot d_{CS}(v,t)}{\eta_g} \right] \tag{1}$$

where $\pi_e(t)$ and $P(v,t)$ are the price of electricity and the charging power of vehicle v at time t; h is the charge epoch length; η_e is the overall efficiency of the charging system ($\eta_e = 0.85$); $\pi_g = 1.06$ \$/L is the price of gasoline; $d_{CS}(v,t)$ is the distance traveled after the battery was depleted (Charge Sustaining, CS mode); $\eta_g = 15.7$ km/L is the CS mode vehicle efficiency; and T and N are the number of epochs and vehicles, respectively. In our implementation, one-hour epochs were used ($h = 1$), and $P(v,t)$ was a continuous variable that varied between 0 and 7 kW. In order to obtain consistent results, the following two constraints were added to the model in [12]:

$$\sum_{v=1}^{N} P(v,t) + P_r(t) \leq \bar{P} \quad \forall t = 1, \dots, T \tag{2}$$

$$P(v,t) \leq P(v, t-1) \quad \forall v, t: \\ d_{tot}(v,t) = d_{tot}(v, t-1) = 0 \ \& \ \pi_e(t) = \pi_e(t-1) \tag{3}$$

where $P_r(t)$ is the total residential load at time t, $\bar{P}$ is the load limit for the transformer or feeder, and $d_{tot}(v,t)$ is the total distance traveled by vehicle v at time t. Constraint (2) ensures that the transformer is not overloaded, and (3) forces PHEVs to charge as soon as possible, so long as the total cost is not affected. In other words, if the total distance traveled by PHEV v is zero in two consecutive time slots (if the PHEV is plugged in at home) and the price of electricity is the same at time t and t-1, the charging power of vehicle v's battery should be greater at the earlier time slot.

Fig. 4 shows results for this optimal charging scheme for the 10-PEV case considered in Figs. 2 and 3. As a result of allowing vehicles to charge at any rate, the approach chooses charge rates that are lower than the full Level 2 rate. This type of "Unidirectional V2G" [5] has advantages in terms of more refined control, but requires additional communication and coordination. As expected, optimal CM fully utilizes the transformer capacity during off-peak hours, but only if travel plans are fully known. The other two methods also keep loads below the power limit, but with somewhat more variability.

5.   Results

This section compares the packetized approach to the optimal and FCFS cases, and to variants of the packetized approach, for a larger number of homes and vehicles. Specifically, we simulated a 500 kVA medium voltage transformer serving 320 homes, each with 1 kVA average load. Each home has two vehicles [33] (i.e., 640 vehicles in total), either or both of which could be a PHEV depending on the PHEV penetration level. The number of homes was selected such that the peak residential load was below the transformer's rated load. We assumed that customers were charged for electricity according to a two-rate, time-of-use residential tariff in which the peak (8 a.m. to 8 p.m.) electricity rate is $\pi_e(t)$=$0.14/kWh and the off-peak rate is $\pi_e(t)$= $0.10/kWh. These assumed values are representative of (though less extreme than) current retail time-of-use rates in the Northeastern US [34]. For the packetized case, we assumed that vehicles in urgent charging mode were charged the peak price ($0.14/kWh) during peak hours. It is important to note that this $0.04 difference between urgent and non-urgent rates is likely conservative, since the cost to utilities of providing non-urgent charging is likely to be only slightly higher than off-peak wholesale energy costs, which are frequently $0.02-$0.03/kWh in the Northeastern US [35].

In order to obtain a distribution of outcomes over a variety of likely travel patterns, 100 unique vehicle travel patterns were randomly selected from the survey data (see [2] for details of this Monte-Carlo model).

5.1   Comparing packetized charging to optimal and FCFS charge management

In this section the packetized approach is compared to results from the FCFS and optimal method for the larger scenario. For the packetized method, we modeled a two-state automaton, with request probabilities of P_1=1 and P_2=0.5. Furthermore, vehicles were set to urgent mode (for the packetized approach) based on the solution from the optimization: if PHEV v charged during peak hours in the optimization results, v was set to urgent charging mode. Essentially this reflects the assumption that drivers were able to estimate their need for urgent charging.

We simulated three different levels of PHEV penetration: 12.5% (N=80), 25% (N=160) and 50% (N=320). Note that these high penetration levels are relatively unlikely in the near term for the aggregate vehicle-fleet in most countries. However, it is not unlikely that some residential neighborhoods could have PEV penetrations that are substantially higher than that of aggregate. As a result of this, and the fact that temporal patterns in non-residential loads differ from residential patterns, we assume that the simulated PHEVs do not impact the two-tier time-of-use price. We also assume that the aggregate system load curve, which would include commercial and industrial customers, is different from the residential load shown in Fig. 5, which shows the baseline and total load for 25% PHEV penetration (160 PHEVs) for each CM scheme. In order to make a clear comparison, we chose 1-hour time slots for the FCFS and optimization method, and 1-hour request intervals and packet lengths (i.e., epochs) for the charge-packet method. Fig. 5 shows that the PHEVs in the charge-packet case use slightly more peak hour charging, than in the optimization case, which increases the overall costs for the charge-packet method somewhat. However, the presumption is the unrealistic requirement that the central optimization approach can obtain perfect information about travel plans. What is notable is that the charge-packet scheme keeps loads below the limit, with costs that are nearly optimal as the load presented to the system is adjusted over time and distributed across PEVs in the system.
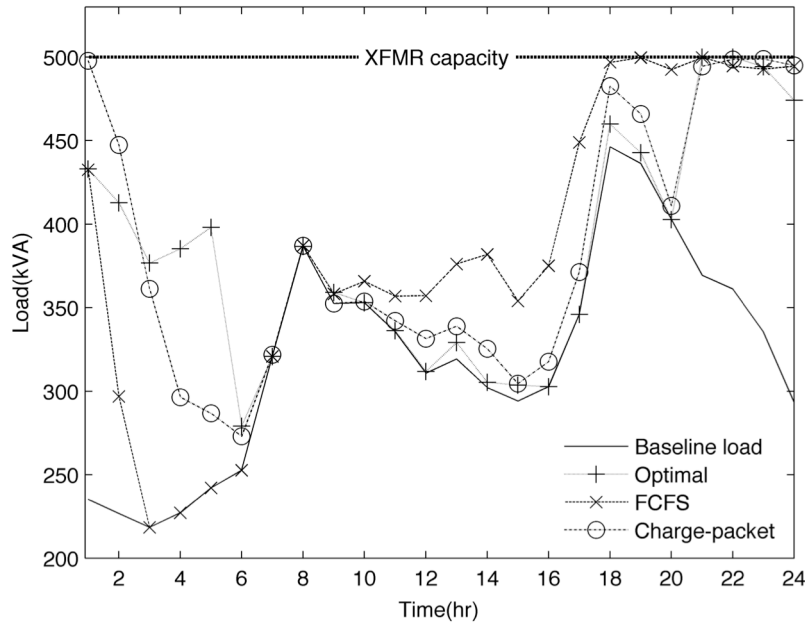
Fig. 5. Daily load curve showing non-PEV residential load and the aggregate load with 25% PHEV penetration.

We compared the average total travel cost per PHEV over 100 one-day Monte Carlo simulations. We assigned each vehicle a random travel pattern from the survey data. The same vehicle-travel pattern combinations were used identically for each scenario, to ensure a fair comparison. The results for two different PEV penetrations (12.5% and 50%), and two different battery capacities are shown in Fig. 6. The gasoline, off-peak and on-peak electricity costs are shown separately. From Fig. 6, we can see that the total travel cost of the charge-packet method is slightly more than that of the optimization method, but much less than the FCFS method. The charge-packet costs are slightly greater because urgency settings were constant during the day, based on the realistic assumption that drivers are not perfect optimizers. The FCFS method is more costly because in this case drivers do not differentiate their charging based on the price of electricity. The result is that in the FCFS method, vehicles consume more peak-hour electricity than in the other methods. One exception is the case of 50% penetration and 24 kWh batteries, where all charging methods use the entire transformer capacity during off-peak hours, but the optimization method can optimally allocate charging to those PEVs that cannot get peak-hour charging. In other charging methods, some PEVs that are not capable of receiving peak electricity (because of not being home) do not get enough charge overnight, and must use the most expensive fuel, gasoline. It should be noted that in our simulations peak electricity at $0.14/kWh is still cheaper than gasoline in terms of $/km travel.
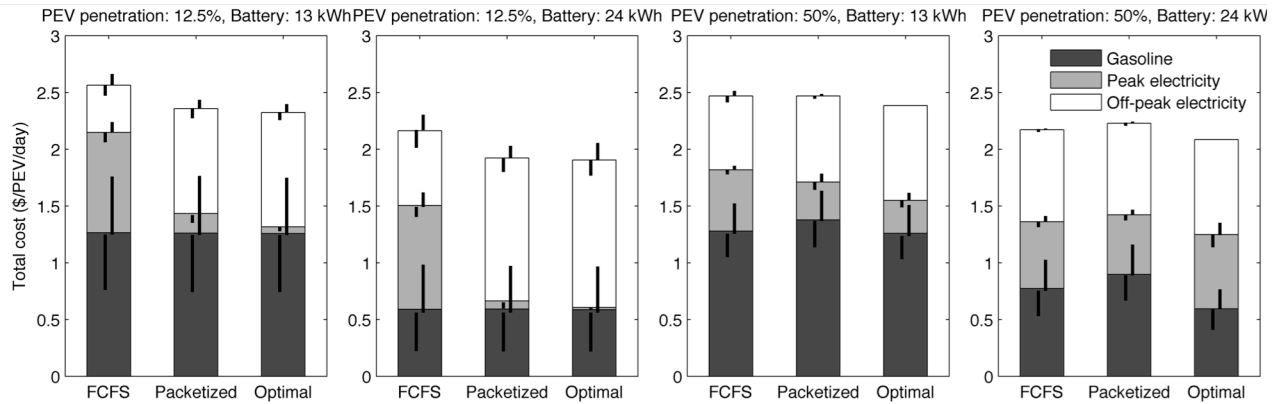
Fig. 6. Average total travel costs in 100 Monte Carlo simulations, showing gasoline, peak and off-peak electricity costs separately in four case studies with different PEV penetrations and battery capacities (bars show the average and black lines show 10th to 50th and 50th to 90th percentile)

Generally, in the higher PEV penetration scenarios, there is insufficient off-peak electricity to allow all vehicles to fully charge their batteries, resulting in more peak electricity usage for the optimization and packetized scenarios. Because of this, increased PEV penetrations resulted in a slight increase in travel costs for the optimization and packetized cases. For example, in the 12.5% PEV penetration case, vehicles can use more off-peak electricity than in the 50% PEV penetration case, where peak electricity is used more.

As one would expect, the results indicate that larger battery capacities result in reduced use of the most expensive fuel, gasoline, and thus reduce travel costs. However, the impact of the larger batteries is different in low and high PEV penetration cases. In the low penetration case, more off-peak electricity can be used for the larger battery, as more transformer capacity is available; in the high penetration case, the transformer capacity is exhausted for both the 13 kWh and 24 kWh battery cases during the off-peak hours, making the benefits of larger batteries less clear.

Most importantly, these results show that the cost of using the packetized method is only 0.9% to 5.2% greater than what we found for the optimal CM case (as opposed to 3.1% to 14.1% for the FCFS CM scheme). The charge-packet method requires much less information from the PEV owner (only the choice of an urgency setting) and requires far less two-way communication than would be required to implement centralized optimization method. In summary, we find that the charge-packet method can achieve near optimal costs, while preserving driver privacy and being robust to random changes in travel behavior.

5.2   Comparing variants of the charge-packet method

The automaton used in the packetized PEV charger allows PEV charging to adapt to reduce the impact on the distribution system, such as overloaded transformers or feeders. However, different automaton probabilities and structures will change the performance of the charge-packet method, particularly with respect to the burden on the communications infrastructure. To investigate the performance of the charge-packet method, we introduced the idea of differentiating between charge-packet lengths, i.e., the time epoch a PEV is given permission to charge, and request intervals, i.e., the time epoch between two requests for charge.

We simulated the charge-packet method with different automaton probabilities, packet lengths (5-minute and one-hour), and request intervals (5-minute and one-hour). The results were
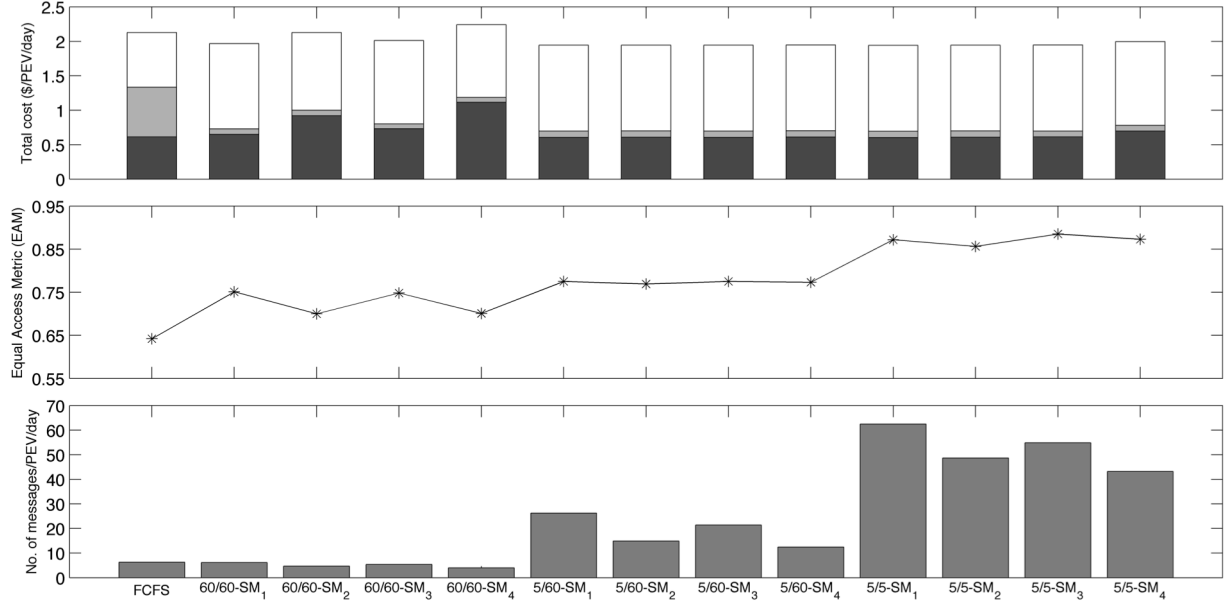
Fig. 7. Comparison of FCFS charging and variations of the charge-packet method. (Top) Average total costs over 100 Monte Carlo simulations, with shades indicating gasoline (black), peak (gray) and off-peak (white) electricity costs. (Middle) The extent which consumers have equal access to the available capacity. (Bottom) Communication burden for the various methods. t_1 and t_2 in t_1/t_2 (e.g., 60/60) show the request interval and the packet length in minutes, respectively. See the text for definitions of the state-machine probabilities SM_i.

compared across three metrics: (1) average total cost, (2) a measure of the extent to which the method provided each vehicle with equal access to the charging resources, and (3) the number of messages transmitted by the PEVs or the transformer, per vehicle-day, assuming the bi-directional communication (duplex) case is implemented (see Sec. 3.2).

One of the problems observed with the FCFS charging case (Sec. 4.1) was that vehicles that began charging earlier than others, before a period in which charge mitigation occurred (typically early evening hours), were not required to stop charging when new vehicles arrived. As a result, vehicles that arrived later in the day frequently were not allowed to begin charging until capacity in the system was released, effectively giving them "less equal" access to charging resources. In order to measure the extent to which vehicles were given equal access to grid resources under different scenarios, we defined an Equal Access Metric (EAM) to assess the "fairness" of each method. For this purpose, we find the probability of charge mitigation for each vehicle v, $P_M(v)$, by dividing the number of time slots that the PEV charge request is denied by total number of time slots that the PEV is requesting charge from the transformer. P_M was computed only for off-peak hours, when all vehicles, whether in urgent or non-urgent mode, were requesting charge. Given the standard deviation of $P_M(v)$ over all v, $\sigma(P_M)$, EAM was calculated as follows:

$$EAM = 1 - \sigma(P_M). \qquad (4)$$

$\sigma(P_M)$ ranges between 0 and 1, which means that EAM has the same range. Therefore, a method with perfectly equal access will have EAM = 1, and lower values of EAM indicate that some vehicles are given more access than others. The rationale for this metric is that as long as all the PEVs are mitigated with the same probability (i.e., the same ratio of mitigation to total requests)

the method maintains its fairness.

Communication burden was measured by counting the number of messages exchanged over the communications network per vehicle per day. Following the two-way communication system design, we assumed that each charge packet request requires one message submission to the aggregator. If the PEV gets a reply (one message), this means that the request is approved; otherwise the charge request is denied.

Fig. 7 shows these three metrics, for three different charge time-interval combinations and four different state machines, along with results for the FCFS charging method. Time-interval combinations are defined using the notation t_1/t_2, in which t_1 is the interval of times between requests and t_2 is the length of the charge packet, both in minutes. The three time-interval combinations compared were 60/60, 5/60 and 5/5, and the state machines were SM_1: $\{P_1 = 1, P_2 = 0.5\}$, SM_2: $\{P_1 = 1, P_2 = 0.5, P_3 = 0.25\}$, SM_3: $\{P_1 = 0.8, P_2 = 0.4\}$ and SM_4: $\{P_1 = 0.8, P_2 = 0.4, P_3 = 0.2\}$. As expected, smaller request intervals and charge-packet lengths reduced charging costs, but increased communication costs. The 5/60 gives about the same travel cost as 5/5, but at the expense of fairness (reduced EAM). It is possible that excessively frequent on/off cycles could have adverse effects on the battery or charging systems. If this was the case, the 5/60 method could be preferable, given that the increase in cost is negligible. Note that 5/60 outperforms 60/60 in terms of equal access.

The results also suggest that using state-machines with $N=3$ rather than $N=2$ states, or with lower transition probabilities, can substantially reduce the burden of CM on the communications system. This notion agrees with the results obtained previously for automaton control applied to wireless sensor node participation [24]. However, these changes also result in small increases in travel costs. If communications bandwidth is not a constraint, the 5/5 charge-packet is superior in terms of both total cost and equal access.

6. Conclusions

This paper draws similarities between the problem of managing the charging of electric vehicles and that of providing multiple devices with access to a bandwidth-constrained communications channel. We propose to treat PEV charging as a random access problem where charge is delivered through many 'charge-packets'. As with random access communication channels, the packetization of charge allows distribution system objectives (i.e., efficient use of available resources without overloading the network) and customer objectives (reducing travel costs) to be achieved simultaneously. Leveraging this approach, this paper presents a new decentralized, automaton-based charge management strategy, which preserves users' privacy more than many existing charge management schemes. Simulations of packetized charging in a constrained residential distribution feeder indicate that the cost increase of our method over an omniscient centralized optimization method (which is untenable in its information requirements) is only 0.9% to 5.2%. However, in comparison to the optimal approach, the charge-packet technique can be implemented with first-generation low-bandwidth advanced metering infrastructure.

While the simulations in this paper are for plug-in hybrid electric vehicles charging in a residential distribution network, the packetized method could be adapted and applied to other thermal or battery storage loads. Battery electric vehicles are likely to have somewhat different charging and travel characteristics than PHEVs: BEV owners would probably take fewer very long trips, and are likely to request the "urgent" charging mode more frequently. Similarly, the

method could be adapted to the management of thermal loads, such as HVAC and water heating. Future work will investigate these adaptations.

Finally, it is important to note that the charge packet approach would not be desirable if discrete switching caused substantially accelerated battery degradation. While detailed analysis of battery impacts are beyond the scope of this paper, evidence from prior research suggest that charging Lithium Ion batteries at a constant rate resulted in no aging benefit, relative to a variable changing rate [36], and that pulsed charging can, under some circumstances, be beneficial to battery life [37].

7. References

[1] Q. Gong, S. Midlam-Mohler, V. Marano, G. Rizzoni, "Study of PEV Charging on Residential Distribution Transformer Life," *IEEE Trans. Smart Grid*, vol. 3, no. 1, pp.404-412, Mar. 2012.

[2] A. Hilshey, P. Hines, P. Rezaei, J. Dowds, "Estimating the Impact of Electric Vehicle Smart Charging on Distribution Transformer Aging," *IEEE Trans. Smart Grid*, vol. 4, no. 2, pp.905-913, Jun. 2013.

[3] J. Sears, J. Dowds, L. Aultman-Hall, P. Hines, "Travel Demand and Charging Capacity for Electric Vehicles in Rural States: A Vermont Case Study," *Transportation Research Record*, (in press), 2012.

[4] Society of Automotive Engineers, "SAE charging configurations and ratings terminology," *SAEJ1772,* 2011.

[5] E. Sortomme, M.A. El-Sharkawi, "Optimal Combined Bidding of Vehicle-to-Grid Ancillary Services," *IEEE Trans. Smart Grid*, vol. 3, no. 1, pp.70-79, Mar. 2012.

[6] C. Quinn, D. Zimmerle, T.H. Bradley, "An Evaluation of State-of-Charge Limitations and Actuation Signal Energy Content on Plug-in Hybrid Electric Vehicle, Vehicle-to-Grid Reliability, and Economics," *IEEE Trans. Smart Grid*, vol. 3, no. 1, pp.483-491, Mar. 2012.

[7] K. Clement-Nyns, E. Haesen, J. Driesen, "The Impact of Charging Plug-In Hybrid Electric Vehicles on a Residential Distribution Grid," *IEEE Trans. Power Syst.*, vol. 25, no. 1, pp.371-380, Feb. 2010.

[8] S. Deilami, A.S. Masoum, P.S. Moses, M.A.S. Masoum, "Real-Time Coordination of Plug-In Electric Vehicle Charging in Smart Grids to Minimize Power Losses and Improve Voltage Profile," *IEEE Trans. Smart Grid*, vol. 2, no. 3, pp.456-467, Sept. 2011.

[9] E. Sortomme, M.M. Hindi, S.D.J. MacPherson, S.S. Venkata, "Coordinated Charging of Plug-In Hybrid Electric Vehicles to Minimize Distribution System Losses," *IEEE Trans. Smart Grid*, vol. 2, no. 1, pp.198-205, Mar. 2011.

[10] R.A. Verzijlbergh *et al.*, "Network Impacts and Cost Savings of Controlled EV Charging," *IEEE Trans. Smart Grid*, vol. 3, no. 3, pp.1203-1212, Sep. 2012.

[11] P. Richardson, D. Flynn, A. Keane, "Optimal Charging of Electric Vehicles in Low-Voltage Distribution Systems," *IEEE Trans. Power Syst.*, vol. 27, no. 1, pp.268-279, Feb. 2012.

[12] R. Sioshansi, "Modeling the Impacts of Electricity Tariffs on Plug-in Hybrid Electric Vehicle Charging, Costs, and Emissions," *Operations Research*, vol. 60, no. 3, pp.506-516, May-June, 2012.

[13] C. Ahn, C. Li, H. Peng, "Optimal Decentralized Charging Control Algorithm of the Electrified Vehicles Connected to Smart Grid," *Journal of Power Sources*, vol. 196, no. 23, pp.10369-10379, Dec. 2011.

[14] M. C.W. Kintner-Meyer, "Smart Charger Technology for Customer Convenience and Grid Reliability," in *Proc. 24th Electric Vehicle Symp.*, Stavanger, Norway, 2009.

[15] P. Richardson, D. Flynn, A. Keane, "Local Versus Centralized Charging Strategies for Electric Vehicles in Low Voltage Distribution Systems," *IEEE Trans. Smart Grid*, vol.3, no.2, pp.1020-1028, June 2012.

[16] H. Yifeng, B. Venkatesh, G. Ling, "Optimal Scheduling for Charging and Discharging of Electric Vehicles," *IEEE Trans. Smart Grid*, vol.3, no.3, pp.1095-1105, Sept. 2012.

[17] Di Wu, D.C. Aliprantis, L. Ying, "Load Scheduling and Dispatch for Aggregators of Plug-In Electric Vehicles," *IEEE Trans. Smart Grid*, vol. 3, no. 1, pp.368-376, Mar. 2012.

[18] N. Rotering, M. Ilic, "Optimal Charge Control of Plug-In Hybrid Electric Vehicles in Deregulated Electricity Markets," *IEEE Trans. Power Syst.*, vol. 26, no. 3, pp.1021-1029, Aug. 2011.

[19] Z. Ma, D. S. Callaway, and I. A. Hiskens, "Decentralized charging control of large populations of plug-in electric vehicles," *IEEE Trans. Control Syst. Technol.*, vol. 21, no. 1, pp.67,78, Jan. 2013.

[20] M.D. Galus *et al.*, "Integrating Power Systems, Transport Systems and Vehicle Technology for Electric Mobility Impact Assessment and Efficient Control," *IEEE Trans. Smart Grid,* vol.3, no.2, pp.934-949, June 2012.

[21] K. Kok *et al.*, "Dynamic pricing by scalable energy management systems - Field experiences and simulation results using PowerMatcher," in *Proc. IEEE Power and Energy Society General Meeting,* San Diego, CA, 2012.

[22] B. Alexander, "Dynamic Pricing? Not So Fast! A Residential Consumer Perspective," *The Electricity Journal*, vol. 23, no. 6, pp.39-49, 2012.

[23] A. Brooks *et al.* "Demand dispatch," *IEEE Power & Energy Mag.*, vol. 8, no. 3, pp. 20–29, May/Jun 2010.

[24] J. Kay and J. Frolik, "An expedient wireless sensor automation with system scalability and efficiency benefits," *IEEE Trans. Syst. Man Cybern. A., Syst. Humans*, vol. 38, no. 6, pp.1198 - 1209, Nov. 2008.

[25] F. Zhong, "A Distributed Demand Response Algorithm and Its Application to PHEV Charging in Smart Grids," *IEEE Trans. Smart Grid*, vol.3, no.3, pp.1280-1290, Sept. 2012.

[26] T. Rappaport, *Wireless Communications: Principles and Practice, 2nd ed.*: Prentice Hall, 2002.

[27] R. Iyer and L. Kleinrock, "QoS control for sensor networks," in *Proc. IEEE ICC*, Anchorage, AK, 2003, pp.517–521.

[28] J. Frolik, "QoS control for random access wireless sensor networks," in *2004 Wireless Communications and Networking Conference (WCNC04)*, Atlanta, GA, 2004.

[29] J. Frolik and P. Hines, "Random access, electric vehicle charge management," in *Proc. 1st IEEE International Electric Vehicle Conf.*, Greenville, SC, March 4-8, 2012.

[30] J. Frolik and P. Hines, "Urgency-driven, plug-in electric vehicle charging," in *Proc. IEEE PES Innovative Smart Grid Technol. (ISGT) Europe Conf.*, Berlin, Germany, 2012.

[31] A. Hilshey, P. Rezaei, P. Hines, J. Frolik, "Electric vehicle charging: Transformer impacts and smart, decentralized solutions," in *Proc. IEEE Power & Energy Society General Meeting*, San Diego, CA, 2012.

[32] U.S. Dept. Transportation, Federal Highway Administration (2009). *National Household Travel Survey (NHTS)* [Online]. Available: http://nhts.ornl.gov/download.shtml.

[33] S. Shengnan, M. Pipattanasomporn, S. Rahman, "Challenges of PHEV penetration to the residential distribution network," in *Proc. IEEE Power & Energy Society General Meeting*, Calgary, Canada, 2009.

[34] Green Mountain Power, "GMP Rates," Online: http://www.greenmountainpower.com/customers/payment/gmp-rates/, Aug. 8, 2013.

[35] ISO New England, "Markets," Online: http://www.iso-ne.com/markets/, Aug. 8, 2013.

[36] Elena Marie Krieger, "Effects of variability and rate on battery charge storage and lifespan", " Ph.D. dissertation, Dept. Elect. Eng., Princeton Univ., Princeton, NJ, 2013.

[37] L.R. Chen, S.L. Wu, D.T. Shieh, and T.R. Chen, "Sinusoidal ripple current charging strategy and optimal charging frequency for Li-ion batteries," *IEEE Trans. Ind. Electron*., vol. 60, no. 1, pp.88-97, Jan. 2013.

Chapter 6

Conclusions

This report describes the results of a two-year study of the impacts of electric vehicles on the electric power distribution infrastructure, which moves electricity between the bulk transmission system and individual homes and businesses.

In Chapter 2, we show that residential service transformers can be adversely affected by even a small number (e.g., 3) of electric vehicles simultaneously charging. This was particularly the case in hot climates, such as Arizona, where ambient temperatures result in smaller margins between the internal thermal limits of a transformer and the actual operating temperature. The results in Chapter 2 also show that well-designed "Smart Grid" control schemes can be useful in dramatically reducing the potential negative impacts of electric vehicle charging. Chapter 3 builds on this work to study the thermal properties of residential service transformers in additional detail. In this study we collected temperature measurements from several instrumented transformers in the Green Mountain Power territory, and used the measurements to test a variety of different thermal models. The results suggest that there are simpler models that may work equally well for residential service transformers, relative to the more complicated thermal models that are commonly used to model larger bulk power transformers.

In Chapter 4, team members propose a new thermal model for underground cables, which are another critical component of the electric power distribution infrastructure. This new method can accurately model the thermal impact of moisture on distribution cables. In cooler, moist climates, such as Vermont, moisture could increase the available capacity in an underground cable, which indicates that there may be capacity for more electric vehicle adoption than one would assume from standard cable models that do not model the impacts of moisture. This new approach makes it possible to more accurately plan for electric vehicle deployment in cool, moist locations.

Finally, Chapter 5 presents a new approach to mitigate the potential negative impacts of electric vehicle charging on the power distribution infrastructure. Unlike optimization-based approaches to electric vehicle charge management, which have been proposed by others, our method does not require information about the vehicles future state (e.g., battery state of charge, arrival time, departure time, etc.) in order to compute a charging schedule. Our approach, in contrast, allows the charging behavior of vehicles to adapt to constraints in a power system, in near real-time. This new approach requires very little data from the vehicles, and what information it does need is anonymous to the central aggregator, and thus the new approach maintains privacy. This new approach to power delivery mimics the means by which data is moved through communication networks; i.e., using 'packets'. As a result, we expect to be able to leverage decades of research into random access communication channels to improve upon the work reported here. In future work, we expect to leverage the core concepts to develop a distributed and adaptive means to manage other large residential loads such as water heaters and air conditioners. Ongoing work, including a pending pilot implementation, is looking at

strategies for applying the method to charge a fleet of vehicles and for managing roadway lighting.

Taken as a whole, these results suggest that electric vehicle charging can have significant impacts on the electric power distribution infrastructure, but that these impacts can be effectively mitigated by careful planning and appropriate use of the increasing capabilities of "Smart Grid" infrastructure.